Polytechnic of Turin

Master's Degree
in Materials Engineering

Application of the Hot Isostatic Pressing on Inconel 738 above its solidus temperature for microstructural enhancement

Thesis supervisor:
Dr. Bassini Emilio

Candidate:
Pignatelli Alberto

Thesis co – supervisor:
Dr. Ugues Daniele

A.Y. 2023/2024

Index

Abstract

Nickel-based alloys are commonly used in demanding applications such as aerospace, nuclear, oil and gas production. The production of components made of these materials is often highly complicated because of their high melting temperature, low castability and forgeability. This condition makes Additive Manufacturing (AM) so attractive for these alloys. Nevertheless, the defectiveness and the microstructure of additively manufactured components differ from traditional ones. Hot Isostatic Pressing (HIP) for these materials is often compulsory and reported in international standards because of the stringent safety levels typically adopted. Nonetheless, the standards still refer to traditional cast or wrought microstructure and adapt poorly to the AM materials, and this is where the thesis finds its focal point. The main scope of this work is to assess the feasibility of a dedicated HIP treatment on Laser Powder Bed Fusion (LPBF) Inconel 738 performed above its solidus temperature, i.e. within the incipient melting region of the alloy. A traditional heat treatment performed in this high-temperature range would be detrimental due to the formation of large porosities and damages. On the other hand, applying high pressures, as in the case of a HIP process, allows entering the incipient melting region without forming new pores. Indeed, the exceptionally high temperature enhances solid-state diffusivity in the material, allowing to form special microstructures. During the soaking stage at such temperatures, the out-of-equilibrium microstructure of AM samples is eliminated and substituted with an equiaxial one. Furthermore, the grain boundaries can coarse very effectively, making the samples potentially more resistant to creep. Moreover, after the HIP cycle, material density results close to the theoretical one because defects have been effectively healed. Based on the results obtained in this work, using HIP above the material solidus temperature is an effective heat treatment for AM components designed for high-temperature applications where creep is the main reason for failure, as in the case of turbine blades.

Chapter 1

General theory about superalloys

1.1 Superalloys

Nowadays, applications in critical fields such as aeronautics, oil and gas or competitive automotive, require complex and performant materials. The principal materials considered for such applications are certainly Fe-, Ni- and Co- based superalloys. These materials show remarkable mechanical performance, e.g., high fatigue resistance, high yield strength, high corrosion and thermal oxidation resistance. Superalloys are generally used at temperatures above 540°C. Fe and Ni based alloys have a face-centered cubic (fcc, austenitic) structure, instead Co based alloys have a hexagonal closed packed structure. Iron, cobalt, and nickel are transition metals with consecutive positions in the periodic table of elements. The iron- nickel-base superalloys are an extension of stainless-steel technology and generally are wrought, whereas cobalt- and nickel-base superalloys may be wrought or cast, depending on the application/composition involved. Appropriate compositions of all superalloy-base metals can be forged, rolled to sheet, or otherwise formed into a variety of shapes. The more highly alloyed compositions normally are processed as castings. Fabricated structures can be built up by welding or brazing, but many highly alloyed compositions containing a high amount of hardening phase are difficult to weld. Properties can be controlled by adjustments in composition and by processing (including heat treatment), and excellent elevated-temperature strengths are available in finished products. Figure 1 compares stress rupture behavior of the three alloy classes. Superalloys have been used in cast, rolled, extruded, forged, and powder-processed forms. Sheet, bar, plate, tubing, shafts, airfoils, disks, and pressure vessels (cases) are some of the shapes that have been produced. These metals have been used in aircraft, industrial, and marine gas turbines; nuclear reactors; aircraft skins; spacecraft structures; petrochemical production; orthopedic and dental

prostheses; and environmental protection applications. Although developed for high-temperature use, some are used at cryogenic temperatures and others at room temperature. Applications continue to expand, but at lower rates than in previous decades. Aerospace usage remains the predominant application on a volume basis.
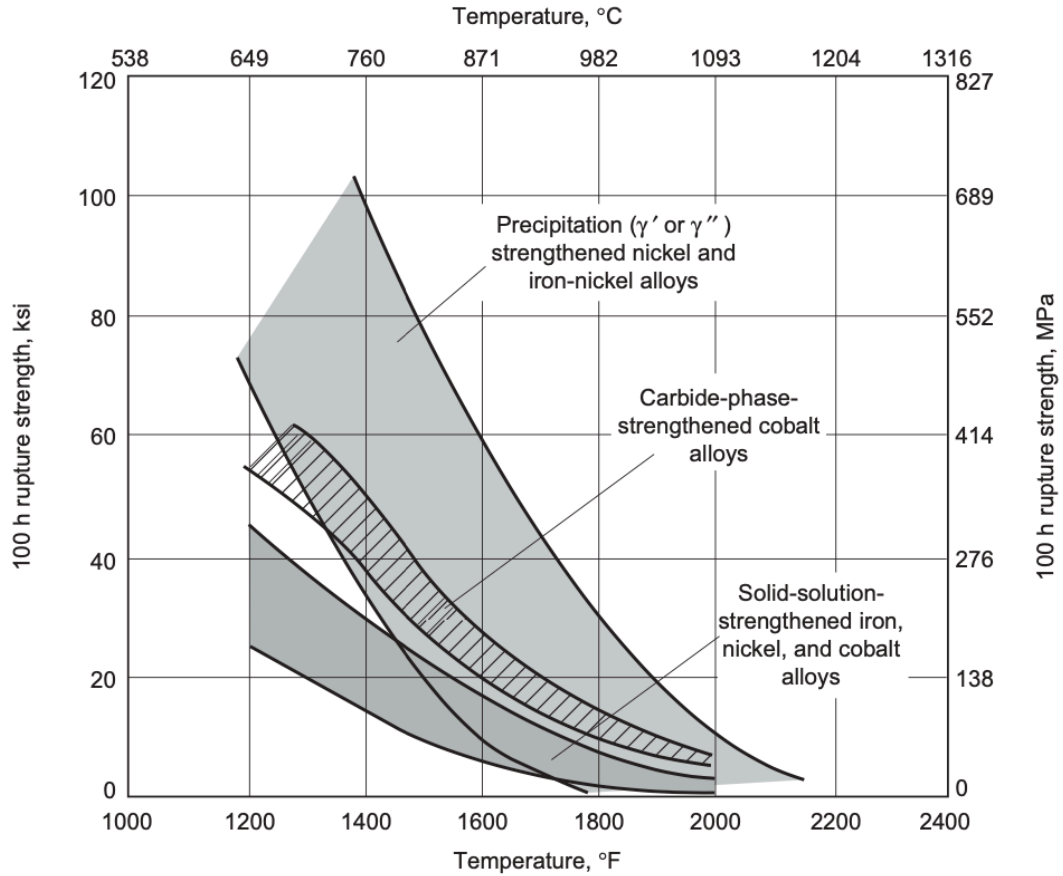

Figure 1: ultimate tensile stress (UTS) comparison among superalloys [1].

1.1.1 Overview on Ni and Ni-based alloys

Nickel has a face centered cubic (FCC) crystalline structure showed in **Errore. L'origine riferimento non è stata trovata.**Figure 2 which means that Ni elementary unit cell arranges 8 atoms on the vertices of a cube and other 6 atoms in the center of the cube faces.
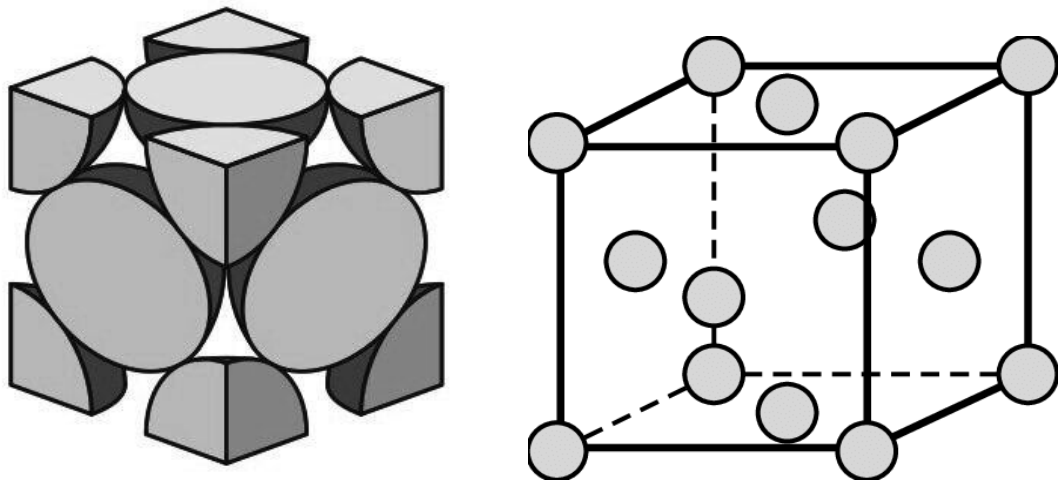
Figure 2: face centered cubic (FCC) structure displayed by Ni [1].

This structure allows ductility and toughness. FCC structure of the nickel is stable from room temperature to very high temperatures. Nickel density is $\rho = 8.9 \text{ g}/\text{cm}^3$ and it presents a melting temperature of $T_m = 1455 \text{ °C}$.

1.1.2 strengthening mechanisms and primary phases

In order to improve the mechanical properties of nickel alloys, several processes are employed. The most important class of nickel-base superalloys is that strengthened by intermetallic-compound precipitation followed by Ni-based alloys strengthened by solid solution [1]. A third class includes oxide-dispersion-strengthened (ODS) alloys such as IN-MA-754 and IN-MA-6000E, which are strengthened by dispersion of inert particles such as yttria, coupled in some cases with precipitate phases (MA-6000E) [2,3]. Strengthening mechanism by solid solution consists in alloying nickel with other elements; atoms of different elements occupy interstitial sites within the crystalline lattice of nickel or reticular sites when replace the nickel atoms of the crystal lattice. When nickel is alloyed, it forms a

principal phase that is indicated whit the Greek letter "γ". Gamma is the matrix phase, it has an austenitic structure (FCC) that mainly contains nickel, chromium and cobalt and other heavy elements such as vanadium, tantalum etc. Elements that undergo in solid solution present dimensional atomic variations respect to nickel atom of the order of 1 to 28% [4,5], this entails notable elastic distortions of the crystal lattice that increase the Young modulus and reduce dislocation motion. Aluminum shows a strong solid solution strengthening behavior, followed by tungsten, molybdenum and chromium. On the contrary, iron, titanium vanadium and cobalt have no strong reinforcement effect when in solid solution. Iron in solution is mostly employed to reduce the final cost of the product. Some examples of solid-solution strengthened alloys are Hastelloy X and IN-625 [6,7]. The solid-solution-strengthened nickel-base alloys may derive some additional strengthening from carbide and/or intermetallic-compound precipitation. The most used strengthening mechanism is precipitation of intermetallic second phases named whit γ′, in general indicated with the brutal chemical formula Ni_3X where X = Ti, Al, Nb, Ta. Ni_3Al presents the FCC elementary unit structure with nickel atoms at the center of the cube faces and aluminum at the vertices of the cube [8]. Titanium can replace Al atoms forming the Ni_3 (Al, Ti) intermetallic compost that is commonly present in these superalloys. Ti, Nb and Ta generate intermetallic phases too but with different reticular lattices, in particular: compact hexagonal in case of Ni_3Ti indicated as μ, orthorhombic or body centered tetragonal lattice for Ni_3Nb named γ′′, and body centered tetragonal lattice for Ni_3Ta. The thermodynamic stability of the intermetallic composts Ni_3X varies, in general the hierarchy from the most stable to the less is: Ni_3Al, Ni_3Ti, Ni_3Nb, Ni_3Ta. In general, the lattice of the intermetallic phase remains cubic until the amount of Al is high enough. Precipitates Ni_3 (Al, Ti) have same crystal lattice of the matrix phase γ (FCC) but slightly different cell parameter; so, in this case the 2 phases γ and γ′ are coherent at the interface between them and are not separated from grain boundaries. The difference between the cell parameters introduces misfits in the overall structure that generate elastic tensions at the interface making tough the dislocation motion. The

presence of elements such Ti, Ta and Nb instead of Al in the intermetallic phase structure widely changes the cell parameter and makes it uncoherent respect to the matrix lattice. For nickel-titanium/aluminum alloys the strengthening precipitate is γ'. Such alloys are typified by the wrought alloys Waspaloy and Udimet (U)-720, or by the cast alloys René 80 and IN-713. For nickel-niobium alloys the strengthening precipitate is γ''. These alloys are typified by IN-718. Some nickel-base alloys may contain both niobium plus titanium and/or aluminum and utilize both γ' and γ'' precipitates in strengthening. Alloys of this type are IN-706 and IN-909. The effectiveness of this hardening precipitates depends on the amount of misfit generated, dimensions, shape and distribution of these phases. For what concern the dimension of the precipitates of γ' the ideal values range over from 200 to 500 nm. The presence of cubic or spheroidal γ' precipitates within the matrix enhances the blocking effect on dislocation motion, as dislocation lines are forced to pass through channels formed by the precipitates. In iron-nickel-base superalloys, the strengthening precipitates usually degrades in a moderate temperature regime, 650 to 760 °C, forming structures and precipitate morphologies that are less effective in strengthening the alloy. Sometimes, to improve the weldability and so the processability via additive manufacturing, concentration of Al and Ti must be reduced [9]. In Table 1: role of alloying elements in superalloys. Adapted from [10].

Effect(a)	Iron-base	Cobalt-base	Nickel-base
Solid-solution strengtheners	Cr, Mo	Nb, Cr, Mo, Ni, W, Ta	Co, Cr, Fe, Mo, W, Ta, Re
fcc matrix stabilizers	C, W, Ni	Ni	…
Carbide form:			
MC	Ti	Ti	W, Ta, Ti, Mo, Nb, Hf
M_7C_3	…	Cr	Cr
$M_{23}C_6$	Cr	Cr	Cr, Mo, W
M_6C	Mo	Mo, W	Mo, W, Nb
Carbonitrides: M(CN)	C, N	C, N	C, N
Promotes general precipitation of carbides	P	…	…
Forms γ' Ni_3(Al,Ti)	Al, Ni, Ti	…	Al, Ti
Retards formation of hexagonal η (Ni_3Ti)	Al, Zr	…	…
Raises solvus temperature of γ'	…	…	Co
Hardening precipitates and/or intermetallics	Al, Ti, Nb	Al, Mo, Ti(b), W, Ta	Al, Ti, Nb
Oxidation resistance	Cr	Al, Cr	Al, Cr, Y, La, Ce
Improve hot corrosion resistance	La, Y	La, Y, Th	La, Th
Sulfidation resistance	Cr	Cr	Cr, Co, Si
Improves creep properties	B	…	B, Ta
Increases rupture strength	B	B, Zr	B(c)
Grain-boundary refiners	…	…	B, C, Zr, Hf
Facilitates working	…	Ni_3Ti	…
Retard γ' coarsening	…	…	Re

(a) Not all these effects necessarily occur in a given alloy. (b) Hardening by precipitation of Ni₃Ti also occurs if sufficient Ni is present. (c) If present in large amounts, borides are formed.

are summarized all the elements that undergoes solution and their role into the alloy.

Table 1: role of alloying elements in superalloys. Adapted from [10].

1.1.3 Embrittling phases in Ni-based superalloys

In some cases, the elevated exposure to high temperatures leads to phase transformations in Ni based superalloys which could lead to a decrement

of mechanical properties. For example, to enhance the mechanical properties Nb can be added in Ni based superalloys that forms carbides and precipitate γ″ with chemical composition Ni_3Nb [11]. Although it must be considered that γ″ is metastable and transforms in phase δ above 800°C. Phase δ has reinforcement properties but his brittleness and the acicular morphology increase stress concentration factor which could makes it a crack nucleator [12].

Other intermetallic phases can derive from intermetallic compounds at high coordination number also called topologically close packing, and can be classified in 3 families [1,13]:

- o Phase σ

- o Phase μ

- o Laves phases.

Phase σ is made up from A_xB_y intermetallic composts where x and y can assume values from 1 to 7. The formation of these phases is observed in range temperatures starts from 650 to 925 °C and is facilitated in Cr and Mo rich alloys.

The μ is a A_7B_6 intermetallic phase, for example Co_7Mo_6 that in case of superalloys assume more complex composition such $(Co, Fe, Ni)_7 (Mo, W, Cr)_6$.

The Laves phases has chemical composition A_2B. Basic Laves phases with hexagonal or FCC lattice are Fe_2Mo, Co_2Ta and Ni_2Nb. In case of superalloys assume complex composition such $(Fe, Ni, Cr, Mn, Si)_2 (Mo, Ti, Nb)$.

All these phases come from long time exposing in critical temperatures range by side effect of the dissolution of the intermetallic hardening phases. Their presence decreases the mechanical properties of the superalloys. In particular, phase η have acicular morphology that involves high stress concentration factor which could make them a crack nucleator.

Phase σ nucleates at grain boundaries with long plates shape and it is dangerous because can be a preferential starting point for cracking formation mechanism at high temperatures. Laves phases have brittle

effect even at room temperature. Furthermore, their formation cause depletion of heavy metals from the matrix with corresponding decrease in hardness.

1.1.4 Secondary phases: carbides

Carbides in the Ni-based superalloys can be observed at the grain boundaries or within the matrix γ. Studies claim that particular morphology and elevated number of carbides located at grain boundaries can affect negatively the mechanical properties of the material [14,15]. For this reason, the concentration of C in superalloys is severely controlled because it is a strong carbide former. C is added in range of 0.02–0.18 wt% [16] in order to strengthen the superalloys by carbides precipitation. Grain boundaries carbides, if present with other specific elements, such as Ta, Hf, Zr, Nb, V, Cr, Mo, and W can improve high temperature resistance due to grain size control through the grain boundary stabilization, in this way grain sliding is reduced or eliminated; also a controlled number of carbides enhance the resistance to hot viscous sliding mechanism also known as creep[16]. Carbides within the grains act as obstacles to dislocation motion, thereby increasing the material's resistance. However, compared to the precipitation strengthening mechanism of the γ' phase, it is less effective. Principal families of carbides are MC, $M_{23}C_6$ and M_6C where "M" indicated the metal element that characterize the carbide that could be Hf, Ta, Nb, Cr, Ti, V, Mo etc. Carbides of type MC form while cooling from the melt by direct combination of refractory elements (Hf, Ta, Nb) or Cr, Ti or V with C. They precipitate both in grains and at grain boundaries, they have FCC crystal lattice with high toughness if compared to other carbides. MC carbides alone are stable but, when elements such as Cr, Mo or W are present into the alloy they can transform during heating at temperatures between 700 to 900°C in $M_{23}C_6$ carbides according to the reaction:

$$MC + \gamma = M_{23}C_6 + \gamma'$$
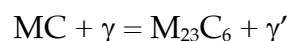
Such phenomenon is facilitated at low concentration of Nb, Ta, Zr or Hf. Among the other types of carbides, the MC is the most thermodynamically stable [1,16].

$M_{23}C_6$ carbides are the least thermodynamically stable and also exhibit a cubic lattice, but they are less tough compared to MC carbides. Their formation can start from MC carbides or by direct combination of metallic elements with residual C from the austenitic phase γ. $M_{23}C_6$ carbides generate due to the presence of Cr in the alloy, other carbide former elements are Mo and W; when these 2 elements are present a mixed carbide can be formed $Cr_{21}(Mo, W)_2C_6$ starting from $Cr_{26}C_6$ phase. They precipitate essentially at grain boundaries and their equilibrium temperature range between 870 to 980°C. When higher temperature is applied, they dissolve into the matrix. Considering their position at grain boundaries these carbides can improve creep resistance by opposing to hot sliding of the grains [17], on the contrary, because of their fragile behavior tend to act as crack promoter especially if they uniformly decorate the grain boundary [14].

M_6C carbides form by transformation of other carbides in alloys containing Mo and W, when temperature range between 815 and 980°C. They also have cubic lattice and are more stable than $M_{23}C_6$. Their higher thermodynamic stability at elevated temperatures makes them suitable for grain size control in extreme operating conditions or during heat treatments.

1.1.5 Secondary phases: borides

Other minor phases worthy of mentioning are borides. B was recently introduced in superalloys in few concentrations of about 50 to 500 p.p.m. because it is a good boundaries stabilator. This element locates at grain boundaries and occupies the reticular vacancies, in this way it blocks diffusive phenomena of other elements and avoids precipitation of brittle phases at grain boundaries. Since boron concentrates in this position, it can form borides of type M_3B_2 that have tetragonal lattice characterized by high hardness. These precipitates can also block the nucleation of cracks deriving from creep phenomena [16].

1.2 Manufacturing processes for Ni-based alloys.

1.2.1 Cast and wrought processes

To produce high-quality steels and superalloys the vacuum induction melting (VIM) process is used. Raw materials such as metal scraps and ferrous master alloys are loaded into a refractory crucible that is surrounded by a cupper coil water cooled. The coil is powered by alternative current, in general at 60 Hz to produce an inducted magnetic field that generates parasite currents into the metallic load. Parasite currents heat and melt the load by Joule effect. The crucible is kept under vacuum with pressure around 10^{-4} atm while the load is melting. The main effects of the VIM process are lowering of the nitrogen and oxygen concentration due to degassing effect, removal by volatilization of low melting point contaminants elements such as lead and bismuth and desulfurization of the melt using additives like calcium oxide [10]. The as built VIM ingots are not suitable for subsequent metallurgical applications unless they are going to be cast processed. The ingot, in fact, presents marked level of segregation, solidification defects, cracks, porosities and ceramic inclusions coming from the refractory materials of the crucible. Therefore, VIM ingots must be processed whit secondary remelting passages which are electroslag remelting (ESR) and vacuum arc remelting (VAR). The ingot obtained by ESR has less impurities and it is much isotropic [18]. Regarding the vacuum arc remelting, this process allows a further refinement of the chemical composition: elements such as hydrogen, nitrogen and oxygen which are particularly hard to get rid of are lowered to few parts per million, furthermore the ingot presents less defects and an even higher isotropic properties respect to ESR ingots. This process is mandatory for ingots that are meant to be used in aeronautic field or, in general, is indicated for materials that must be very reliable and poor in defects [1,18]. The VIM remelting step is applied several times to achieve higher quality and so how higher cost. A resume scheme of this processes is reported in Figure 3.
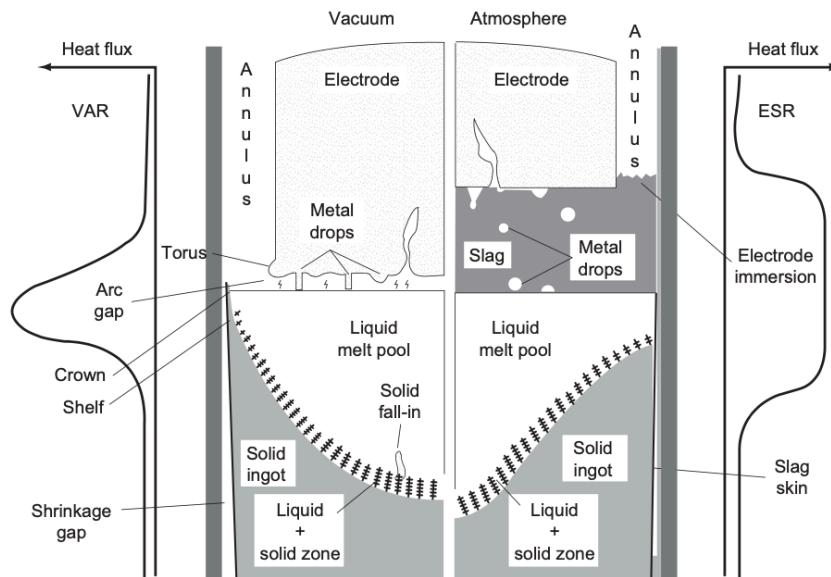
Figure 3: schematic of solidification relationships in VAR (left) and ESR (right) melting processes [18].

Consumable remelted superalloys generally are processed to either forged parts or to sheet/plate. Forged products are produced through an intermediate (billet) forging process, during which refinement of the cast structure is accomplished and a recrystallized grain size is established. Subsequent die forging of parts cut from the billet may further processed to refine the microstructure or simply shaped into the desired form. Workability is affected primarily by composition and secondarily by microstructure [19], a workability rating is shown in Figure 4. Optimal strain and temperature conditions for working of superalloys can be defined by "processing maps".

Alloy	Forging temperature		Forgeability
	°C	°F	
A-286	1065	1950	Excellent
IN- 901	1095	2000	Good to excellent
Hastelloy X	1095	2000	Excellent
Waspaloy	1080	1975	Good
IN-718	1065	1950	Excellent
Astroloy	1095	2000	Fair to good

Figure 4: forgeability ratings of superalloys [20]

Similarly, ingots to be processed into sheet are often converted by cogging to the desired input size for the rolling mill. The large reductions of the

subsequent sheet-rolling process reduce the need for control of cogged structure compared to that required for forging stock [10]. Thus, for some alloys utilizing ESR as the secondary melt process, the ingot may be "cast" into a slab for direct input into the rolling process.

Cobalt-base and strengthen hardened nickel-base superalloys are processed to complex final shapes by investment casting. Iron-nickel-base superalloys are not customarily investment cast [1]. Investment casting permits intricate internal cooling passages and re-entrant angles to be achieved and produces a near-net shape of very precise dimensions. Most investment castings are small random-grain-oriented polycrystalline articles ranging in weight from hundred grams to a few kilos, but columnar-grain and single-crystal parts also are being cast, some as large as 4.5 to 9 kg. In addition, large investment castings are being made in configurations up to several meters in diameter and hundreds of kilos in weight. Many alloys are investment cast, including VIM superalloys, steels, and aluminum. These metals are melted and poured into the mold and solidified under conditions according to whether the product is to be large or small, and polycrystalline, columnar grained, or single crystal [10,21]. Inclusions, coarse grain size, surface attack in core leaching, core shift, and resulting undersized wall thickness are a few of the problems encountered in investment casting of superalloys. Hot isostatic pressing techniques used for powder processing have been applied successfully in many instances to eliminate non-surface connected porosity, particularly in large castings of iron-nickel- and nickel-base superalloys. Improved fatigue and creep life generally result, because casting quality is improved by HIP.

1.2.2 Powder metallurgy, an overview

Sintered nickel-base materials and other superalloys enjoy wide commercial usage due to their unique properties, such as corrosion resistance, wear resistance, mechanical strength at low and elevated temperatures, thermal expansion, electrical conductivity, and magnetic permeability. Commercial products represent a wide range of shapes, sizes, and microstructures. Sintered products with ≤90% porosity are technologically as important as fully dense products. Sintering practices

16

aimed at achieving such diverse properties represent a variety of manufacturing technologies.

Powder metallurgy techniques are being used extensively in superalloy production. Principally, high-strength gas turbine disk alloy compositions such as IN-100 or René 95 [1], which are difficult or impractical to forge by conventional methods, have been powder processed. Inert atmospheres are used in the production of powders, often by gas atomization, and the powders are consolidated by extrusion or hot isostatic pressing (HIP). The latter process has been used either to produce shapes directly for final machining or to consolidate billets for subsequent forging. Extruded or HIP billets often are isothermally forged to configurations for final machining. Minimal segregation, reduced inclusion sizes, ability to use very high-volume fraction γ' compositions, and ease of grain-size control are significant advantages of the powder process. Reduced costs, particularly through HIP formation of near-net-shape disks, may be possible with powder techniques, but the extent of actual cost savings is a function of alloy and part complexity. Deformation processing of powder-produced articles generally is preferred from a mechanical property standpoint [1,10]. Designers tend to have more confidence in parts that have been deformation processed to some extent. The deformation processing is thought to enhance the detectability of subsurface imperfections that would limit the fracture mechanics life of the article. Another facet of P/M is the importance of maintaining low gas content in powder products to minimize potential defects. Sources of excessive gas in P/M superalloys include hollow argon-atomized powder particles and container leakage or insufficient evacuation and purging of containers before consolidation. Powder techniques also have been used to produce turbine blade/vane alloys of the oxide dispersed strengthened (ODS) type. Mechanical alloying is the principal technique for introducing the requisite oxide/strain energy combination to achieve maximum properties. Rapid-solidification-rate (RSR) technology has been applied to produce highly alloyed (very high-volume fraction γ') superalloys and shows promise for advanced gas-turbine applications. Rapid-solidification-rate and ODS alloys can benefit

from aligned crystal growth in the same manner as can directionally cast alloys. Directional recrystallization has been used in ODS alloys to produce favorable polycrystalline grain orientations with elongated (high-aspect-ratio) grains parallel to the major loading axis.

1.2.3 Powder production

Powder metallurgy (P/M) processing of superalloys begins with the powder production process. Both vapor-metallurgical and hydro-metallurgical methods are used for producing pure powders. The end use of the powder dictates the method used. Alloyed powders are produced by either atomization techniques or high-energy ball milling (mechanical alloying).

Atomization is simply the breakup of a liquid into fine droplets. Any material available in liquid form can be atomized. In the case of high melting materials, the result is frozen droplets, that is, powder. Typically, the size of atomized powders is smaller than 150 μm, although larger-sized powders can be produced (in which case atomization is referred to as "shotting" or "granulation").

The general types of atomization processes include several industrial and research methods [1]. Principal industrial methods are:

- o Two-fluid atomization, where a liquid metal is broken up into droplets by impingement with water, oil, or an inert gas (Figure 5 a and b)
- o Centrifugal atomization, where a liquid stream is dispersed into droplets by the centrifugal force of a rotating disk, cup, or electrode (Figure 5 c)
- o Vacuum or soluble gas atomization, where a molten metal is supersaturated with a gas that causes atomization of the metal in a vacuum (Figure 5 d)
- o Ultrasonic atomization, where a liquid metal film is agitated by ultrasonic vibration (Figure 5 e)
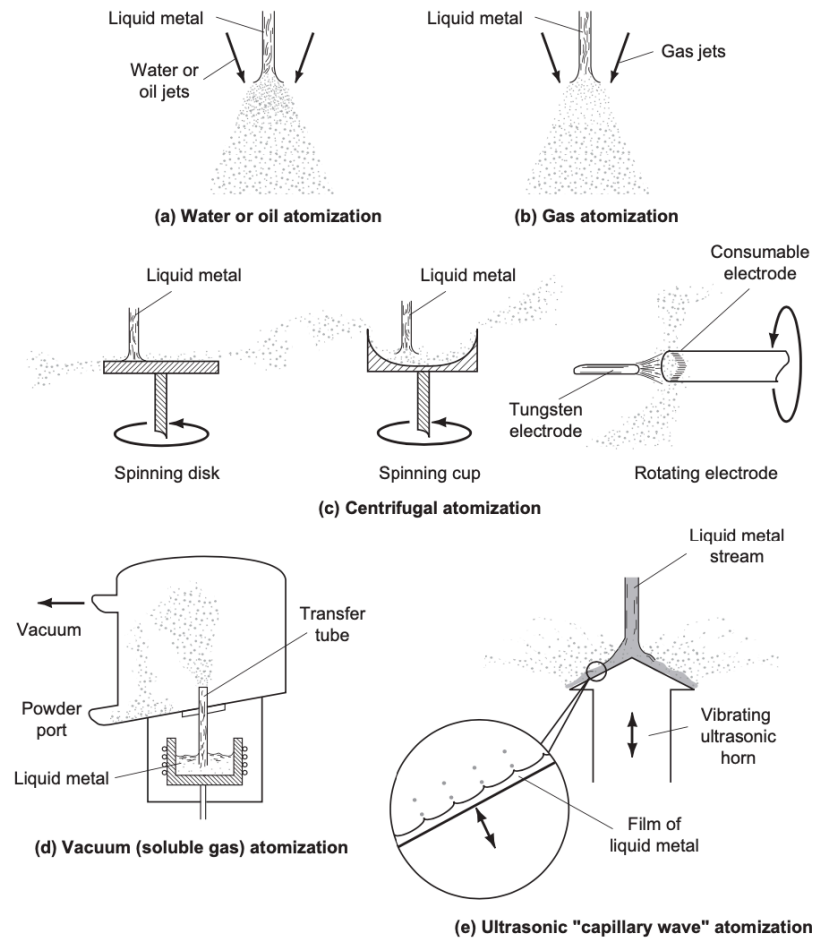
Figure 5: schematic of industrial atomization processing [1]

1.2.4 Additive manufacturing

A new technology known as rapid prototyping has enabled significant changes within the casting industry by eliminating the need for many of the investment casting process steps. This elimination has led to significant cost and lead-time reduction for development hardware. Processes such as stereolithography, selective laser sintering, and other three-dimensional printing technology can provide casting patterns without the use of costly conventional wax or ceramic injection dies [1]. Special machines can take a three-dimensional computer-aided design (CAD), convert the design into cross-sectional layers (an STL file), and build a three-dimensional representation of the CAD geometry in plastic, wax, or polymer. Some processes can directly build (from three-dimensional CAD geometry) three-dimensional ceramic shells into which metal can be poured. Other technologies focused on direct metal fabrication from 3D-CAD geometry

are being developed [22,23]. These technologies have revolutionized the industry in allowing faster development through low-cost iterative design so that design concepts can be transitioned to production rapidly.

Powder bed fusion (PBF) techniques currently offer the best reproducibility and dimensional accuracy within metal AM production and, therefore, have been well-researched in both industry and academia. In general, PBF techniques utilize the following steps to fabricate a part: (1) a layer of pre-alloyed metal powder of specified thickness is spread onto the build plate of the machine; (2) the desired area within the layer of powder is selectively melted together using a laser or electron beam heat source; (3) the build plate moves down, and a new layer of powder is spread onto the build plate; (4) this process is repeated layer-by-layer until the part is completed. PBF processes have been used in various industries for numerous applications such as medical (customized orthopedic components and implants from bio-materials of titanium, stainless steels, and cobalt-chrome alloys), aerospace and defense (fuel nozzles, brackets, turbine blades, engine components, and structural member), and energy (heat exchangers and turbine airfoils).

As specified in the ISO/ASTM52900 standard [24], PBF is defined as an additive manufacturing process in which thermal energy selectively fuses regions of a powder bed. Processes that fall under this category include electron beam melting (EBM), selective laser melting/sintering (SLM/SLS), which are described more recently as direct metal laser melting (DMLM) or direct metal laser sintering (DMLS). ASTM has defined the following terminologies for AM technologies:

- o For direct laser deposition → Laser beam directed energy deposition (L-DED).
- o For selective laser melting, laser powder bed fusion, etc. → Laser beam powder bed fusion (L-PBF).
- o For electron beam technologies such as powder feed or powder bed → E-DED and E-PBF, respectively.

In this thesis work only laser powder bed fusion process will be discussed in detail because the material subject of following analyses it's been manufactured in this manner.

LPBF also known as selective laser melting, uses a laser as the primary tool to manufacture a part in a layer-by-layer process. It is capable of producing parts in a range of metal alloys, including aluminum, titanium, iron, and nickel-based superalloys. There are different manufacturers for this type of metal AM. A step-by-step process methodology for LPBF AM is summarized in Figure 6.
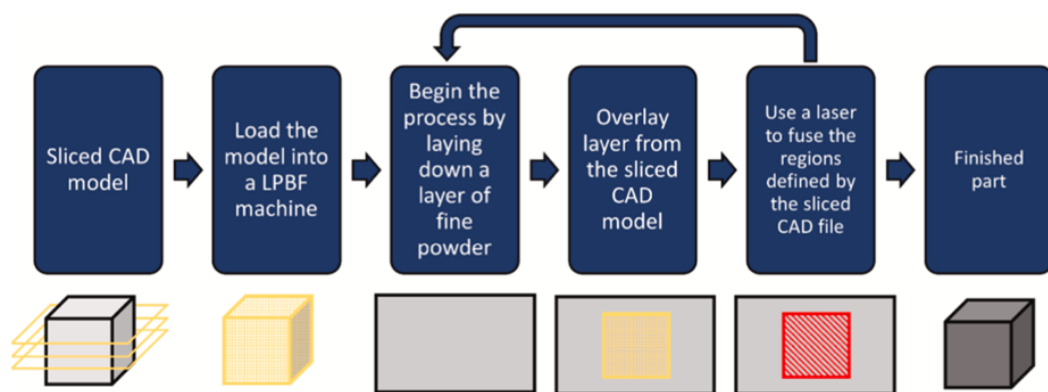

Figure 6: general build methodology for an L-PBF machine. Rectangular grey drawings represent a bed of powder during the L-PBF process. [25]

Once the full part has been printed, the excess powder is removed (and often recycled) and then the build plate is unloaded from the build chamber. Since the printed part is fused to the build plate, mechanical removal is required. Before removal, the parts are typically left on the build plate and given a stress-relief heat treatment to minimize residual stresses, eliminate warping, and maintain dimensional accuracy. The LPBF technique fills niches in industries where either rapid prototyping or low-volume production is needed. The inherently additive nature of the process allows printing of complex lattice structures (Figure 7 a) and parts with intricate internal geometries like the GE fuel nozzle (Figure 7 b). Moreover, it allows for part consolidation and the geometrical optimization for lighter weight such as the seat brackets (Figure 7 c). LPBF of metal parts has largely developed in recent years. Besides the increasing number of commercially available machines, significant effort has gone into research to improve the

technique. One of the major challenges, especially in applications where fatigue is a concern, is the defects that form inside a build. Understanding the building process and defect formation is the key to building high-quality parts.
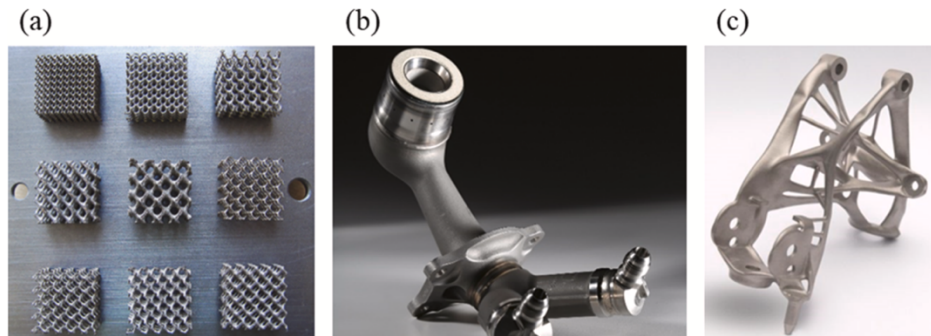

Figure 7: examples of AM geometries. (a) lattice structures[26]. (b) Fuel nozzle [27]. (c) Lightweight seat bracket [28] .

There are many studies on the effect of process parameters on microstructure, porosity level, and defect formation. Influential process parameters are (1) laser-related parameters (e.g., laser power, spot size, pulse duration, and pulse frequency), (2) scan-related parameters (e.g., scan speed or velocity, scan spacing or hatch, scan rotation, and scan pattern), (3) powder related parameters (e.g., powder morphology, particle size and distribution, layer thickness, dosing, and materials properties), and (4) macroscopic parameters (e.g., powder bed temperature and its uniformity, gas flow, gas type, spreader bar type) [25]. Computational modeling has been applied to the LPBF process to predict laser-powder interaction, melt pool geometry, and potential defect formation based on the input processing parameters [29]. The formation of defects in LPBF has several causes. High speed x-ray visualization [30,31] has shown that, at sufficiently high laser power, the vapor cavities or "keyholes" that form above a characteristic threshold in power density tend to be unstable and generate keyhole porosity [32,33]. At a constant laser power, increasing the scanning speed elongates the keyhole and makes it shallower. In general, there is an optimal combination of power, velocity, hatch spacing and layer depth for printing which gives an optimal process window. Nevertheless, transfer of porosity from the powder to the build can occur via capillary forces. At high

power and speed, bead-up or humping leads to instabilities in melt pool shape that can also cause porosity. Finally, increasing the scan speed at constant power results in the lack-of-fusion (LOF) case where insufficient melt pool overlap results in unfused regions in the form of porosity and/or inclusion of un-melted particles. The potential defects are shown in Figure 8 as regions in the laser power-scanning speed "processing window" or region where full density can be expected. The point is that defect morphologies in PBF metal AM follow predictable trends within power-velocity-hatch-layer (*P-V-H-L*) processing parameter space [34,35]. In addition to the P-V-H-L processing combination, scan strategy (Figure 9) plays an essential role in defect formation in PBF processes. Scan strategy influences heat transfer, melt formation from powder, and solidification rate, affecting the type of defects, location, and distribution as well as grain morphology. Thus, it is crucial to optimize process parameters, heat source power, and scan speed and strategy for minimizing process-induced porosity. During the laser powder bed fusion process and following powder spreading, which is governed by many powder characteristics, a laser selectively scans the surface of the powder layer to melt and fuse the metal powder following the STL input file in the respective layer. The complex laser-matter interaction leads to many phenomena that may result in defects in the final part. Common defects include balling/bead-up, lack of fusion, keyhole porosity, the ejection of spatters of molten metal or powder particles, denudation of the surrounding substrate, or microstructural defects.
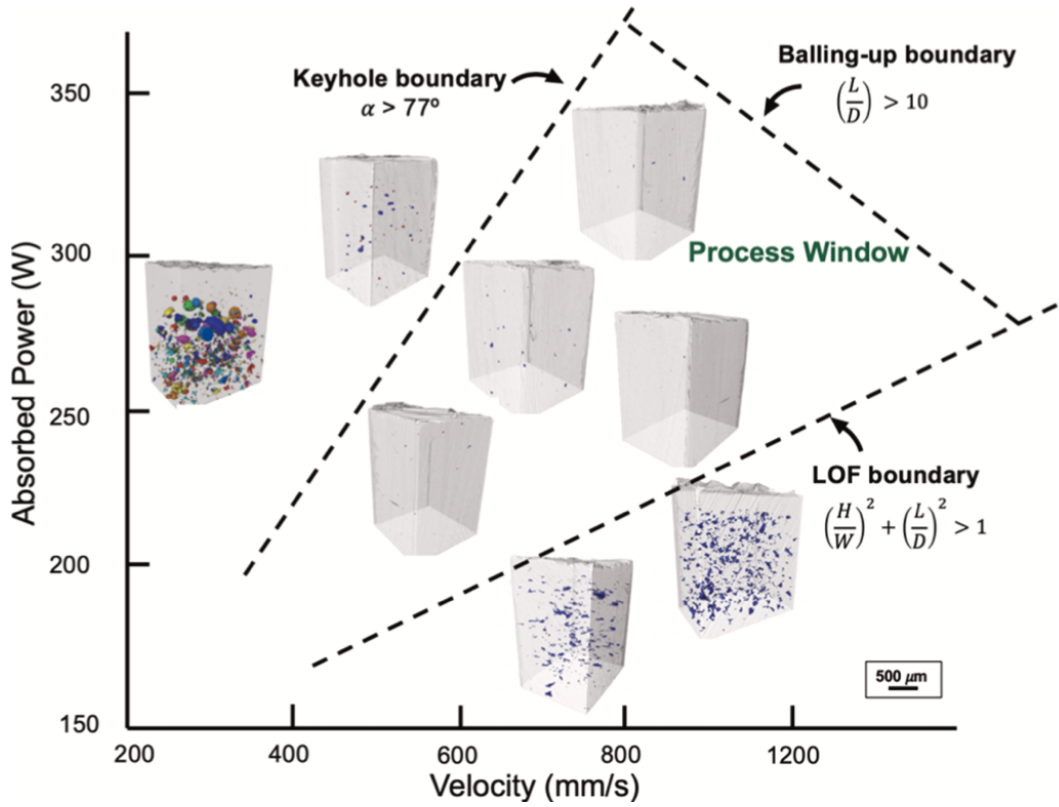
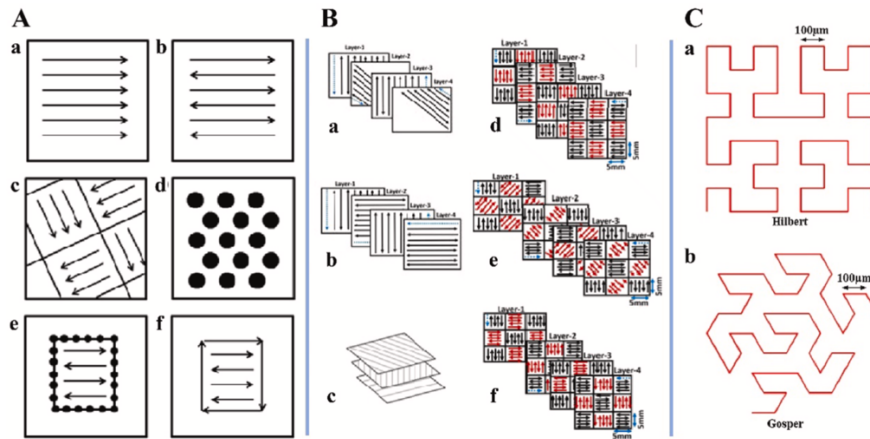*Figure 8: defects and processing window for LPBF [25].*

Figure 9: (A) Different scan strategies used in the L-PBF process. (a) unidirectional or concurrent fill, (b) bi-directional, snaking, or countercurrent fill, (c) island scanning, (d) spot melting, (e) spot melting contours with snaking fill, and (f) line melting contours with snaking fill [23]. (B) Schematics illustrating scan patterns of (a) 45◦ alternating, (b) 90◦ alternating, (c) 67◦ alternating, (d) chessboard scanning, and chessboard scanning with adjacent chessboard block scanned in (e) 45◦ and (f) 90◦ rotated direction [36]. (C) Examples of fractal scan strategies of (a) Hilbert and (b) Gosper [37].

1.3 Heat treatments in Ni-based alloys

Nickel has an austenitic structure, and in the nickel and high-nickel family of alloys, no allotropic phase transformations occur, the alloys are austenitic from the melting temperature down to absolute zero. While some precipitates such as carbides and the γ' hardening phase may form, these do not change the basic austenitic-type structure of the matrix. The main goal of thermal treatments in nickel-based superalloys is to optimize the material's microstructure to meet the demanding requirements of high-temperature applications.

These treatments aim to:

o Maximize high-temperature strength and creep resistance by controlling the precipitation of strengthening phases like γ'.

o Improve fatigue resistance and toughness.

o Minimize grain boundary-related failures by reducing porosity and promoting the formation of stable carbides.

o Ensure dimensional stability and reduce internal stresses for long-term performance.

Almost all heat treatment methods used with nickel and the nickel alloys are employed either to soften them, such as annealing, or to increase their strength, such as age hardening. Furthermore, heat treatments serve also to control grain size microstructure using appropriate cooling and heating ramps. In summary, thermal treatments in nickel-based superalloys are essential for developing the desired balance of strength, ductility, and thermal stability, allowing these materials to perform effectively in critical applications at elevated temperatures.

1.3.1 Types of Heat Treatment

Nickel and the nickel alloys may be subjected to one or more of five principal types of heat treatment, depending on chemical composition, fabrication requirements, and intended service. These methods include:

• *Annealing:* a heat treatment designed to produce a recrystallized grain structure and softening in work-hardened alloys. Annealing usually

requires temperatures between 705 and 1205 °C, depending on alloy composition and degree of work hardening [38].

• *Solution treating:* a high-temperature solutioning at 1150 – 1315 °C of certain nickel alloys to put carbides in solid solution and produce a coarse grain size for enhanced stress-rupture properties. Normally applied to age-hardenable materials before the aging treatment[39,40].

• *Stress relieving:* a heat treatment used to remove or reduce stresses in work-hardened non-age-hardenable alloys without producing a recrystallized grain structure. Stress-relieving temperatures for nickel and nickel alloys range from 425 to 870 °C, depending on alloy composition and degree of work hardening [41].

• *Stress equalizing:* a low-temperature heat treatment used to balance stresses in cold-worked material without an appreciable decrease in the mechanical strength produced by cold working [42].

• *Age hardening or precipitation hardening:* a treatment performed at intermediate temperatures (425 – 870 °C) on certain alloys to develop maximum strength by precipitation of a dispersed phase throughout the matrix [43].

1.3.2 Grain size control

To achieve the mechanical properties demands for each application, the microstructure in superalloys is fundamental. Several processes are applied to obtain the desirable grain structure and, in general, the overall microstructure. It is known that finer grain size leads to higher fatigue resistance conversely, to improve high temperature resistance coarser grains behave better [44]. In recent years there has been more interest in the interdependence of hot working and heat-treating operations because in many critical applications, the desired final properties are not attainable only via heat treatment. This requires a study of hot working and heat treating, known as thermomechanical processing. One application of thermomechanical processing is the development of direct age Inconel 718 for turbine disk applications. Proper heating temperatures and forging operations also influence the microstructure and distribution of phases in alloys such as 718 [1]. An important objective of thermomechanical

processing is grain size control. For example, grain structure may be controlled by thermomechanical processing in several iron-nickel-base alloys that have two precipitates present, such as the primary strengthening precipitate (γ'' Ni_3Nb in Inconel 718 and γ' Ni_3Ti in Inconel 901) and a secondary precipitate (δ in Inconel 718 and η Ni_3Ti in Inconel 901). The secondary precipitate is produced first, by an appropriate heat treatment (8 h at 900 °C, for 901), followed by working at about 950 °C, below the η solvus. Final working is carried out below the recrystallization temperature, and the alloy is subsequently recrystallized below the η solvus. Finally, the alloy is aged by standard procedures. The result is a fine-grain alloy with higher tensile strength and improved fatigue resistance due to deformation working provided to the component but also, to grain boundaries control through precipitate phases [39,45]. Instead, different approach for AM near net shape manufactured products must be considered as they cannot be processed with hot or cold deformation processes. Difficulties in controlling the microstructure by using only heat treatments are widely studied, for example the solution heat treatment at temperatures high enough to dissolve all the primary γ' particles and homogenize the alloy for subsequent γ' re-precipitation in the form of uniformly distributed fine γ' precipitates has been severely restricted in IN738 alloy due to the occurrence of incipient melting [46]. Consequently, the standard solution heat treatment generally adopted for this alloy has been limited to 2 hours at 1120 °C, which results only in a partial homogenization. For these reasons other heat-treating methods for controlling the microstructure are being researched. Studies [47,48] asses that solution, hot isostatic pressing (HIP) and annealing treatments display good grain size and microstructure controlling effect. Especially a proper combination of solution and HIP treatments is used to refine the grain size microstructure to obtain enhanced mechanical properties.

1.3.3 Incipient melting

When metals are alloyed, there is no longer a single melting point for a composition. Instead, alloys melt over a range of temperature. The lowest

melting temperature (incipient melting temperature) and melting ranges of superalloys are functions of composition and prior processing [21]. Nickel-base superalloys may show incipient melting at temperatures as low as 1204°C. However, advanced nickel-base single-crystal superalloys having limited amounts of melting-point depressants tend to have incipient melting temperatures equal to or in excess of those of cobalt-base superalloys. Incipient melting in Ni – based superalloys is due mainly to:

- o Presence of inter dendritic low melting γ - γ' eutectic phases [46].
- o Segregation of element such as Mo or Co [49].
- o Precipitation of intergranular low melting M_3B_2 [50].

In particular, it was discovered that M_3B_2 precipitates with lamellar morphology liquefaction is induced by the partial dissolution of nearby MC carbides, this led to faster intergranular cracking process.

1.4 IN738 an overview

The following work of thesis focuses on IN738 superalloy, so for this reason a brief description of this Ni – based superalloy is reported. IN738 is essentially used in turbine engines for ground energy production, in particular, for blades of the fourth rotor section as reported Table 2.

Table 2: Alloys and coatings used in the hot sections of various industrial gas turbines [51].

Manufacturer	Model	Vanes	Blades	Coatings
ABB	11N2	IN939	IN738LC	NiCrAlY+Si
	GT24/26	DS CM247LC (R1)/ MarM247LC (R2,3)/ IN738 (R4,5)	DS CM247LC (R1–3)/ MarM247LC (R4,5)	TBC (R1V)/NiCrAlY+Si (R2–4 B,V) Uncoated R5V, Chromised (R5B)
GE	7/9EA	FSX-414 (all stages)	GTD-111/IN738/ Udimet 500	RT22/GT29-In+ (R1B)
	7/9FA	FSX-414 (R1)/ GTD-222 (R2,3)	DS GTD-111 (R1)/ GTD-111 (R2,3)	GT33-In/GT-29-In+/ Chromise (R3)
	7H	SC Rene N5 (R1)/ FSX-414/GTD-222	SC Rene N5 (R1)/ DS GTD-111 (R2,3)	TBC (R1,2 B,V)/ All others GT33
Siemens	V84/94.2	IN939	IN738LC/IN792 (R4)	CoNiCrAlY+Si
	V84/94.3A	SC PWA1483 (R1,2)/ IN939	SC PWA1483 (R1,2)	TBC (EB-PVD R1B)/MCrAlY+Re
Westinghouse/ Mitsubishi	501D5/701D	ECY-768/X-45	Udimet 520	MCrAlY
	501/701F	ECY-768/X-45	IN738LC	TBC (R1 B,V)/ MCrAlY/Sermalloy J
	501/701G	IN939	DS MarM002 (R1,2)/ CM247	TBC (R1,2 B,V)/ EB-PVD/MCrAlY

Note: R1, R2, etc. refer to the first, second rotor sections, etc.; B and V refer to blade and vane, respectively.

Alloy IN-738 is a precipitation hardenable nickel-base alloy possessing excellent high temperature creep-rupture strength combined with hot corrosion resistance superior to that of many high-strength superalloys of lower chromium content. It is designed to provide the gas turbine industry with an alloy which will have good creep strength up to 870 °C combined with the ability to withstand long-time exposure to the hot corrosive environments associated with the engine. Alloy IN738 exhibits tensile properties superior to and elevated temperature stress-rupture properties comparable to those of the widely used Alloy 713C along with substantially better sulfidation resistance [52]. The standard heat treatment for this alloy consists in a solution treatment at 1120 °C for 2 hours and air cooled followed by aging treatment at 845 °C for 24 hours and air cooled [52]. The heat treatment is performed in order to precipitate spheroidal γ′ and grain

boundaries carbides (specially MC and $M_{23}C_6$ carbides). In this way could be achieved the best combination of mechanical and physical properties.

1.4.1 Additively Manufactured IN738

Additive manufacturing processes, such as laser powder bed fusion (LPBF) previously mentioned, have gained significant attention for the production of nickel-based superalloys like IN738, particularly in turbine blade applications. The use of AM for this alloy not only reduces material waste but also opens possibilities for rapid prototyping and the production of lightweight, intricate designs that would be challenging with conventional manufacturing methods. LPBF processes for turbine blade manufacturing use powders of IN738 alloy obtained by gas atomization. LPBF is a transient metallurgical process characterized by extreme temperature gradients and high cooling rates, which lead to high residual stresses, high dislocation density, numerous fine cellular sub-grains [15] or columnar grain structures [53], and insufficient precipitation of precipitated phases compared to the traditional casting process [54]. Due to the traditional heat treatment program, unsuitable for the LPBFed process, it is essential to develop a specific heat treatment regime to tailor the microstructure of these manufactured type of alloys. There is an amount of work performed on optimizing the heat treatment regime of LPBFed IN738LC alloy. Studies asses that the recrystallization temperature of LPBFed IN738LC alloy is 1230 °C [55,56] and indicated that recrystallization did not occur in the as-deposited state of IN738 alloy after heat treatment at 1200 °C/2 h [57]. These findings demonstrate that the recrystallization temperature of LPBFed IN738 alloy is significantly higher than that of nickel-based alloys prepared by conventional processes (1000 – 1100 °C) [1,10]. LPBFed alloys display a cellular sub-grain structure and fine grain size, leading to an exceptional tensile performance at room temperature. Conversely, adjusting the heat treatment process to achieve larger grain sizes can significantly improve the high temperature creep resistance.

1.4.2 Reasons behind super solidus HIP

The purpose of this thesis work is to investigate at what temperature the IN738 alloy, manufactured via laser powder bed fusion, undergoes significant recrystallization. Once the temperature is determined, it will be verified whether the use of hot isostatic pressing treatment can enlarge the grain size without leaving residual porosity. In order to promote a large recrystallization of the alloy, the process temperature will be set in the super solidus region of IN738. The incipient melting temperature of LPBFed IN738 is of 1260 °C as reported in [58]. Considering the abovementioned reasons this treatment will lead to a complete solubilization of γ' phases and the other microstructure's components, but concurrently to large porosity formation due to incipient melting mechanisms. This issue will be prevented by the application of isostatic pressure with Ar gas. Furthermore, the formation of liquid will lead to have both solid and liquid diffusive mechanisms within the alloy which can further improve recrystallization and homogenize the microstructure [59]. In this way could be finally obtained a material with large grain microstructure as well as less porosities than the as built.

Chapter 2

Materials and methods

2.1 Description of IN738 analyzed in the thesis

The material object of this work of thesis is nickel alloy Inconel® 738LC provided by Siemens Energy. The nominal chemical composition that is reported in the official data sheet is shown below in Table 3.

Table 3: nominal composition of IN738LC [60].

	Ni	Cr	Nb	W	Mo	Ta	Ti	Al	Co	C	Sn, Mn	S, P, O, N	B, Zr
Wt%	bal.	16	0.8	2.6	1.75	1.7	3.5	3.5	8.5	0.10	<0.04	250 p.p.m.	<0.04

Siemens Energy produces IN738LC blades by laser powder bed fusion with EOSM290 machine, using argon as shielding gas, an HSS recoater blade, a layer thickness of 40 μm and typical wall thickness of 0.3 – 0.4 mm [60].

2.2 Metallographic preparation

Samples of IN738LC provided by Siemens Energy were subjected to metallographic preparation to ensure the surfaces of the samples were properly exposed for microstructural examination, in particular, to determine the volumetric porosity. The starting samples were cylindrical rods with 14 mm diameter and 120 mm height. To conduct a complete porosity analysis of the as built condition, samples were taken from the top, the center and the tail of the rod. Samples were cut with a disc saw machine in cylindrical specimens of 2 cm height and then cut again in a half. In this way it was possible to study the material from xy and xz orientations plans. Then, specimens were embedded into 20 ml of thermoset phenolic resin in a mounting machine at 155 °C. After incorporation, samples were polished with sandpapers starting from grit size 180 to 1200. A final polishing process with silicon carbide sandpaper with grit size of 2400 was conducted.

Thus, lapping procedure was performed with colloidal silica pastes in three passages, respectively with colloidal size of 6, 3 and 1 μm. To conduct the SEM and grain size analyses specimens were etched with Kalling nr.2; this etchant is used to highlight the grains into the microstructure [61].

2.3 Optical analysis

Prepared cross sections are analyzed in the non-etched condition by light optical microscopy using a LeicaMEF4 microscope on incident light mode without polarization filter and a constant magnification of 100x. 10 images are taken from the core and 5 from the edge samples location. If not stated otherwise, cross sections from the xy-plane are used for the defect analysis. A dense microstructure appears as bright area in the light microscopy images, as the polished surface reflects the light to a high degree. Defects represent surface irregularities which reduce the fraction of reflected light, so that they appear as dark areas. The resulting contrast between dense microstructure and defects is used to separate both areas. This is done automatically with the open-source software ImageJ, whereby the detected areas which represent defects are in general spherical pores, lack of fusions and cracks. The aspect ratio value it's calculated by the ratio between the major and minor axis of the smallest ellipse that circumscribes the defect. The average of this ratio estimates the mean morphology of flaws detected by the software: an aspect ratio value of 1 indicates that flaws are perfectly spherical, on the contrary, as higher values are as irregular the morphology of the defect. Feret diameter is another method used to evaluate defect's morphology. This value indicates the minimum equivalent radius of the sphere that circumscribes the defect. The used method to quantify the defects is not free from error but nevertheless allows for a quick and user independent analyses of a large number of images.

2.4 Grain size analysis

Grains size analyses are conducted on etched samples. 5 images for edge and 10 images for core locations are taken with optical microscope at 100x magnification. Then images were analyzed using ImageJ software. For the

calculation of the average grain diameter reference has been made to the ASTM E112 regulation [62]. In Figure 10 is reported the table taken for reference.

ASTM E112 – 13 (2021)

TABLE 4 Grain Size Relationships Computed for Uniform, Randomly Oriented, Equiaxed Grains

Grain Size No. G	$\bar{N}_A$ Grains/Unit Area		$\bar{A}$ Average Grain Area		$\bar{d}$ Average Diameter		$\bar{\ell}$ Mean Intercept		$\bar{N}_L$
	No./in.² at 100X	No./mm² at 1X	mm²	µm²	mm	µm	mm	µm	No./mm
00	0.25	3.88	0.2581	258064	0.5080	508.0	0.4525	452.5	2.21
0	0.50	7.75	0.1290	129032	0.3592	359.2	0.3200	320.0	3.12
0.5	0.71	10.96	0.0912	91239	0.3021	302.1	0.2691	269.1	3.72
1.0	1.00	15.50	0.0645	64516	0.2540	254.0	0.2263	226.3	4.42
1.5	1.41	21.92	0.0456	45620	0.2136	213.6	0.1903	190.3	5.26
2.0	2.00	31.00	0.0323	32258	0.1796	179.6	0.1600	160.0	6.25
2.5	2.83	43.84	0.0228	22810	0.1510	151.0	0.1345	134.5	7.43
3.0	4.00	62.00	0.0161	16129	0.1270	127.0	0.1131	113.1	8.84
3.5	5.66	87.68	0.0114	11405	0.1068	106.8	0.0951	95.1	10.51
4.0	8.00	124.00	0.00806	8065	0.0898	89.8	0.0800	80.0	12.50
4.5	11.31	175.36	0.00570	5703	0.0755	75.5	0.0673	67.3	14.87
5.0	16.00	248.00	0.00403	4032	0.0635	63.5	0.0566	56.6	17.68
5.5	22.63	350.73	0.00285	2851	0.0534	53.4	0.0476	47.6	21.02
6.0	32.00	496.00	0.00202	2016	0.0449	44.9	0.0400	40.0	25.00
6.5	45.25	701.45	0.00143	1426	0.0378	37.8	0.0336	33.6	29.73
7.0	64.00	992.00	0.00101	1008	0.0318	31.8	0.0283	28.3	35.36
7.5	90.51	1402.9	0.00071	713	0.0267	26.7	0.0238	23.8	42.04
8.0	128.00	1984.0	0.00050	504	0.0225	22.5	0.0200	20.0	50.00
8.5	181.02	2805.8	0.00036	356	0.0189	18.9	0.0168	16.8	59.46
9.0	256.00	3968.0	0.00025	252	0.0159	15.9	0.0141	14.1	70.71
9.5	362.04	5611.6	0.00018	178	0.0133	13.3	0.0119	11.9	84.09
10.0	512.00	7936.0	0.00013	126	0.0112	11.2	0.0100	10.0	100.0
10.5	724.08	11223.2	0.000089	89.1	0.0094	9.4	0.0084	8.4	118.9
11.0	1024.00	15872.0	0.000063	63.0	0.0079	7.9	0.0071	7.1	141.4
11.5	1448.15	22446.4	0.000045	44.6	0.0067	6.7	0.0060	5.9	168.2
12.0	2048.00	31744.1	0.000032	31.5	0.0056	5.6	0.0050	5.0	200.0
12.5	2896.31	44892.9	0.000022	22.3	0.0047	4.7	0.0042	4.2	237.8
13.0	4096.00	63488.1	0.000016	15.8	0.0040	4.0	0.0035	3.5	282.8
13.5	5792.62	89785.8	0.000011	11.1	0.0033	3.3	0.0030	3.0	336.4
14.0	8192.00	126976.3	0.000008	7.9	0.0028	2.8	0.0025	2.5	400.0

Figure 10:ASTM E112 regulation, reference table for grains size calculation [62].

2.5 Observation with electronic microscope

Samples once etched were observed with the scanning electron microscope Zeiss evo 15. Images were taken both in secondary electron and backscattered electron mode to highlight the surface morphology and the phases of the specimen respectively. Magnifications of 5Kx, 10Kx, 15Kx, 20Kx and 30kx were used. For a better identification of the present phases EDS detector is also used.

2.6 DSC test and heat treatments

As previously mentioned in the first paragraph, the IN738 superalloy produced via LPBF exhibits a microstructure and resulting characteristic temperatures that differ from those obtained through casting processes. Therefore, heat treatments were conducted to verify the accuracy of the data found in the literature and to experimentally determine the microstructure's response to high temperatures, in particular the grain microstructure evolution, the characteristic solidus temperature and the incipient melting

temperature region. These data are fundamental in order to optimize the hot isostatic pressing process parameters as effectively as possible. To evaluate the solidus temperature a differential scanning calorimetry of the LPBFed IN738 a (DSC) test and different heat treatments were performed. The DSC test was conducted in a Setaram DSC/TGA furnace on a specimen of 50.3 mg, starting from a temperature of 20 °C to 1350 °C with a heating and cooling rate of 20 °C/min. Following treatments were conducted on larger specimens with height of 20 mm to evaluate the heat response of the material in a most similar real treatment condition by using a furnace. In detail: 4 samples have been treated respectively at 1270, 1280, 1290 and 1300 °C for 1 hour and then air cooled. Finally, a standard solutioning heat treatment it's been performed on a 2 cm height specimen. For cast IN738 the solution treatment consists in heating for 2 hours at 1120 °C with subsequent air cooling.

2.7 Taguchi method

The hot isostatic pressing process above the solidus temperature is an innovative method aimed at enhancing the performance of the IN738 superalloy and improving its production process. To accelerate the experimentation of this process while maintaining effectiveness, new approach known as Design of Experiment (DOE) have been employed. The design of experiments is a tool for planning, designing and analyzing the experiments so that valid and objective conclusions can be drawn effectively and efficiently from results of the experiments [63,64]. The Taguchi method is a form of DOE developed by Genichi Taguchi used for efficient planning and conducting experiments to analyze how different parameters affect the mean and variance of a process performance characteristic. Taguchi proposed a special design of orthogonal arrays to study all parameters at their corresponding levels with a small number of experiments only. The results of the experiments are further transformed into a signal-to-noise (S/N) ratio. The S/N ratio is a measure of quality characteristics deviating from or nearing to the desired values.

2.7.1 DOE set-up

Minitab is a widely used software package for data analysis, statistical applications, and process improvement, helping organizations around the world enhance quality and reduce costs [65]. It is utilized across various industries such as healthcare, manufacturing, and education. Minitab offers tools for performing statistical analyses, including regression analysis, hypothesis testing, and ANOVA, along with graphical tools that enable users to visualize data effectively. Minitab allows setting up the design of experiment using the Taguchi method. For a consistent data analysis, the software suggests 9 trials resulting from an optimal combination of 3 values each for the 3 main parameters of HIP process: temperature, pressure and time. The choose of these 3 values is discussed in the following paragraphs.

Chapter 3

Experimental

3.1 DSC analysis

Below in Figure 11 are reported the curves of the DSC test conducted on IN738.
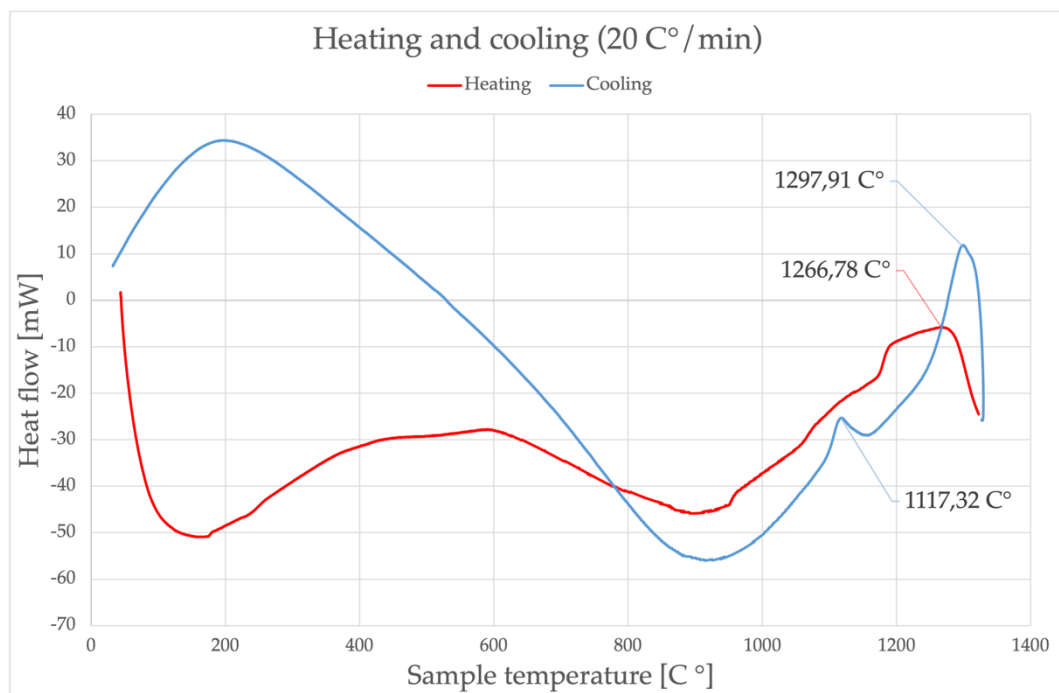
Figure 11: DSC heating and cooling curves for IN738.

The peak in the DSC heating curve at a temperature of 1266 °C is related to the solidus point of IN738, which means that above this temperature a liquid phase starts forming during heating. From the cooling curve instead, it is possible to see that the first crystal starts forming at temperatures under 1300 °C. Thus, the possible work window for hot isostatic pressing could be between 1266 °C and 1300 °C, where liquid formation is most likely to happen. Other important transition phases, for example the peak highlighted in the cooling curve at temperature of 1117 °C could be reconducted to the precipitation of hardening phases such as γ' or carbides.

3.2 As built characterization

Some examples of the defects analyzed in the as built samples are showed in Figure 12, images are taken from head sample both in the xy and xz orientation.
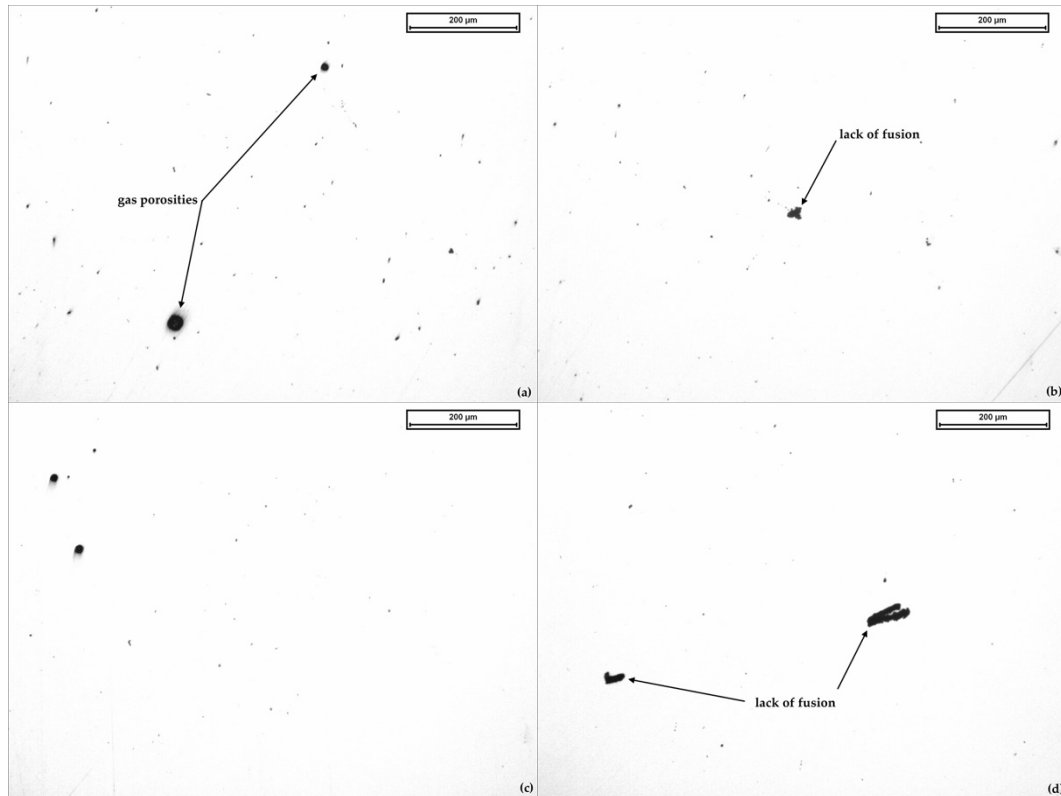
Figure 12: edge xy (a), core xy (b), edge xz (c), core xz (d) top sample.

The results obtained by the optical analyses are reported below in Figure 13 and Figure 14. Concerning the mean aspect ratios it is possible to see that no particular trend is present between the top, core and tail samples; only in the edge of the top specimen can be seen a peculiar mean value. Instead, the average porosities showed in Figure 14 exhibit a marked behavior: mean values of the porosities at the core site are higher than the values reported for the edge site. These values of aspect ratios can be correlated to gas porosities and lack of fusion caused by the manufacturing.
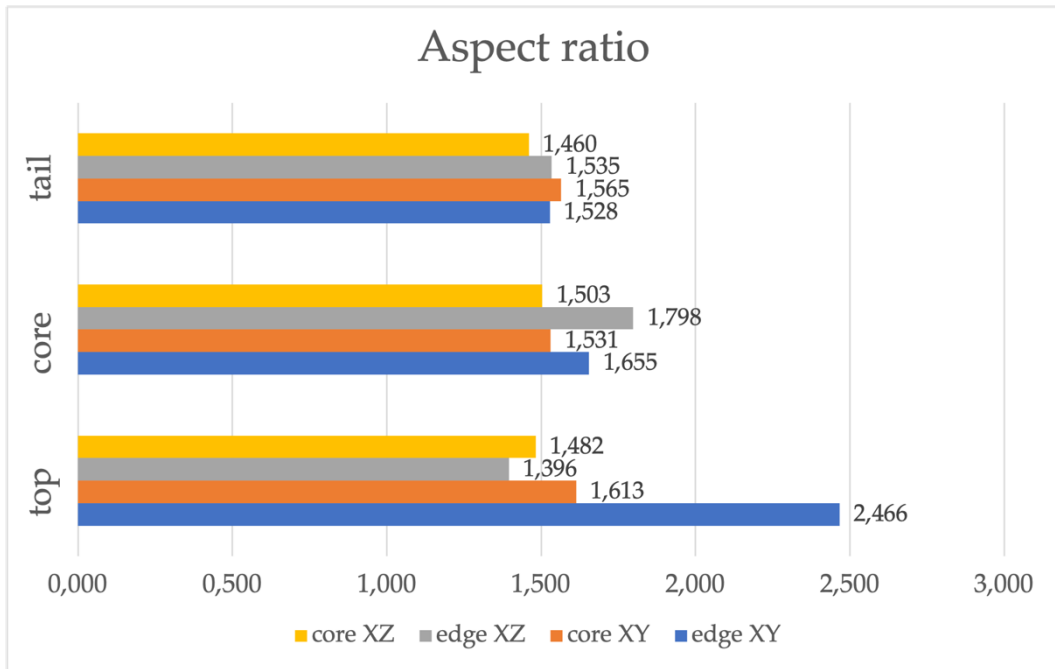
Figure 13: as built mean aspect ratios.
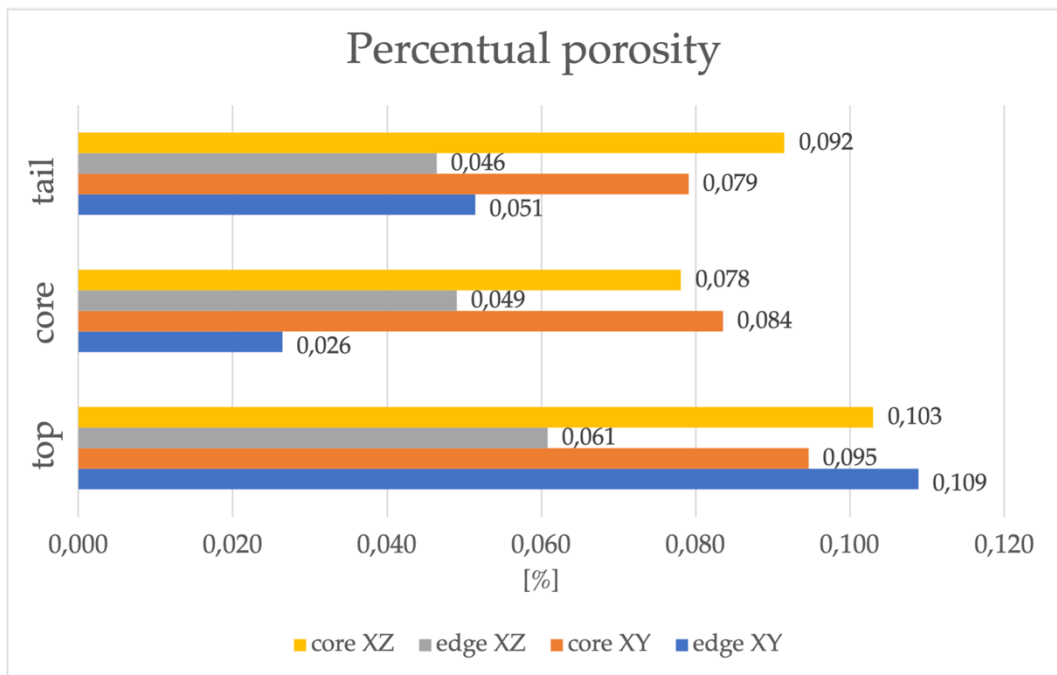
Figure 14: as built mean percentual porosities.

Etched as built samples presents the typical AM grain microstructure that can be seen in Figure 15: in the xy plane (Fig. a) can be seen fine grains, almost in a cellular structure. In fig. (b) can be seen columnar grains

obtained during cooling, also, chemical attack has highlighted in the xz-plane melt pools left by the laser during the AM building process.
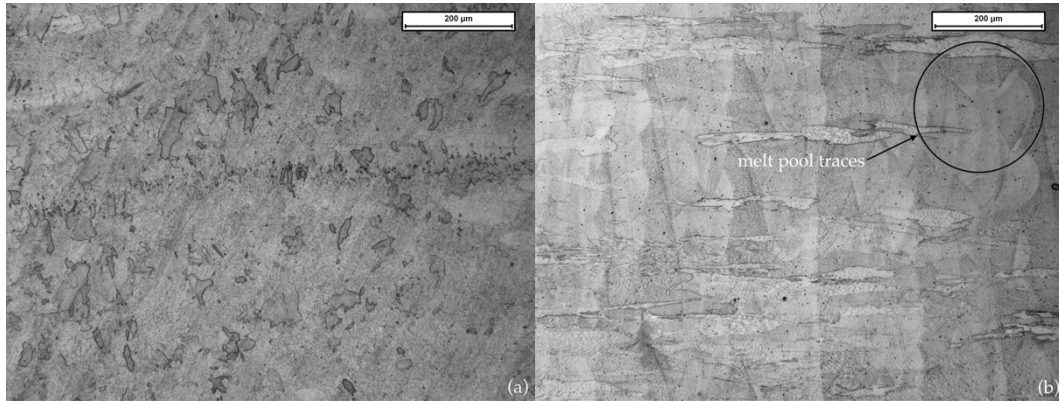
Figure 15: grain microstructure in center sample; (a) xy-plane (b) xz-plane.

Results from the SEM analyses conducted on tail sample in both xy and xz plane are reported below. In particular, Figure 16 confirms the presence of the cellular grain microstructure (Figure 16 a), at 1Kx magnification can also be noticed the marks left by the laser during the AM production process (Figure 16 b). Image detected with backscattered electrons (Figure 16 c) show segregated heavy elements (brighter regions) that could be Nb or Ta; probably due to the high cooling rate such elements couldn't form carbides or other precipitate phases. Finally, in Figure 16 d can be seen also dendritic lamellar formations, this lamellar region could probably lead to the consequently formation of elongated small grains that sometimes could be find in AM product's microstructures.
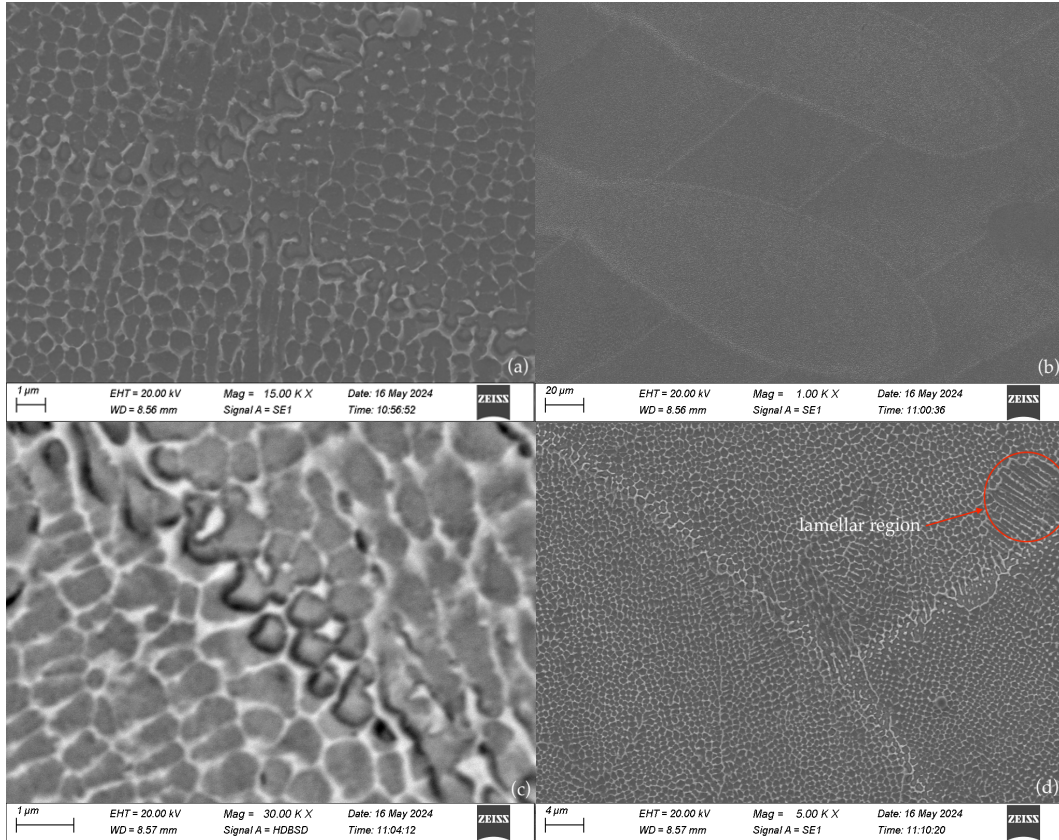
Figure 16: SEM images detected with secondary electrons signal (a, b, d) and backscattered signal (c) at different magnifications.

3.3 Microstructure of heat-treated samples

As previously mentioned, a standard solution treatment and non-standard heat treatments were performed to evaluate the microstructure and liquid formation evolution with increasing temperature. A resume scheme of non-standard heat treated samples are reported below in Table 4:

Table 4: nonstandard heat-treated samples.

Sample	Temperature treatment [°C]
1	1270
2	1280
3	1290
4	1300

3.3.1 Standard solution heat treatment

Firstly, results obtained with the standard solution treatment for IN738 are reported. The data obtained from the optical analyses of the defects are reported in Table 5. In this case it can be noticed that the edge is more defective than the core of the sample. The average aspect ratios remain similar to the as built specimens.

Table 5: summary of defects analysis of solutioning heat treated sample.

Solubilized sample	Edge		Core	
		St. deviation		St. deviation
Average aspect ratio	1.406	0.421	1.413	0.425
Average porosity [%]	0.051	0.022	0.035	0.020
Average defect radius [μm]	10.736	2.220	8.797	2.478

In Figure 17 can be seen that after the heat treatment some recrystallization occur; grains became slightly larger respect to as built condition.
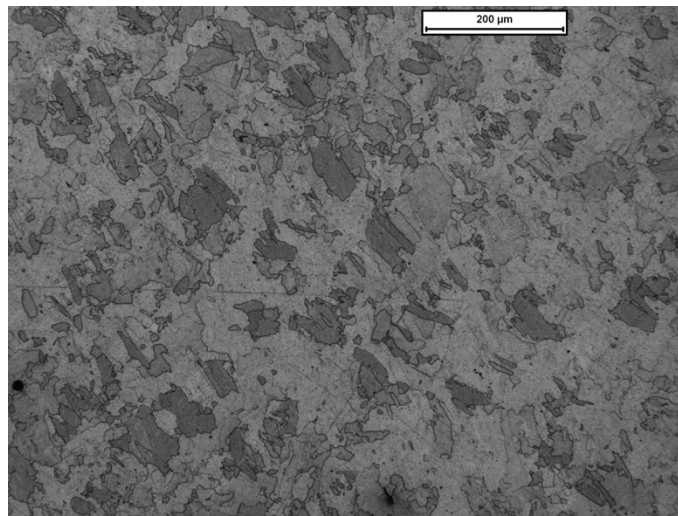
Figure 17: grain microstructure of solutioning treated sample.

SEM analysis with secondary electrons signal at 5 Kx magnification clearly shows in Figure 18 the grain boundaries highlighted by the brighter carbides of MC and M_6C type; such carbides are also visible within the grains. From the backscattered signal at 10 Kx magnification (fig. 18 b) can

be slightly seen the presence of γ′ spheroidal phase in the darker circular areas.
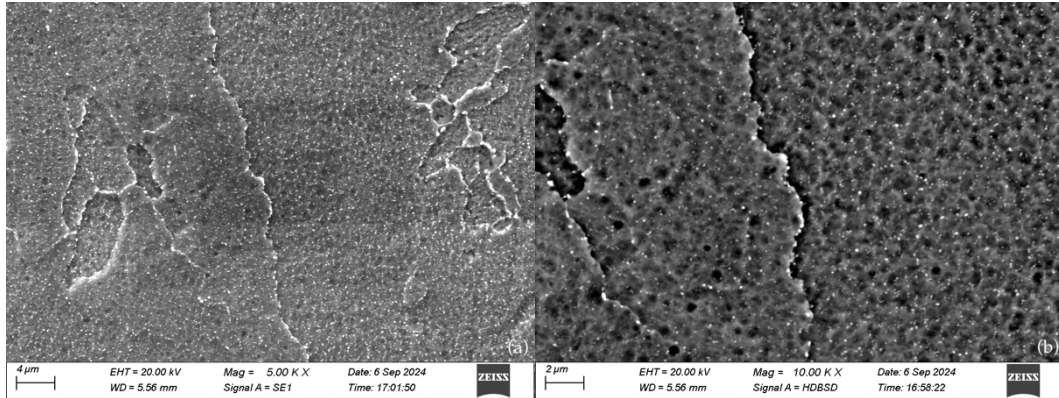
Figure 18: solubilized sample SEM images taken with secondary electrons (a) and backscattered electrons (b).

These results confirm that LPBFed IN738 is subjected to poor solubilization after the standard treatment since γ′ phase is hardly noticeable, and carbides largely decorate the grains and grain boundaries. Furthermore, grains remain almost of the same dimensions as the as built state of the material this leads to assess that poor recrystallization has occurred.

3.3.2 Non-standard heat treatments and definition of the Incipient melting range

Static furnace treatments were performed to investigate the amount of liquid phase formation in the range temperatures resulting from the DSC test. In Figure 19 are shown explicative images of the surface of samples 1, 2, 3 and 4 in the xz direction. From a first view it is possible to notice severe gas porosities and larger and irregular flaws resulting from incipient melting especially at 1290 °C (fig. 19 c) and at 1300 °C (fig. 19 d).
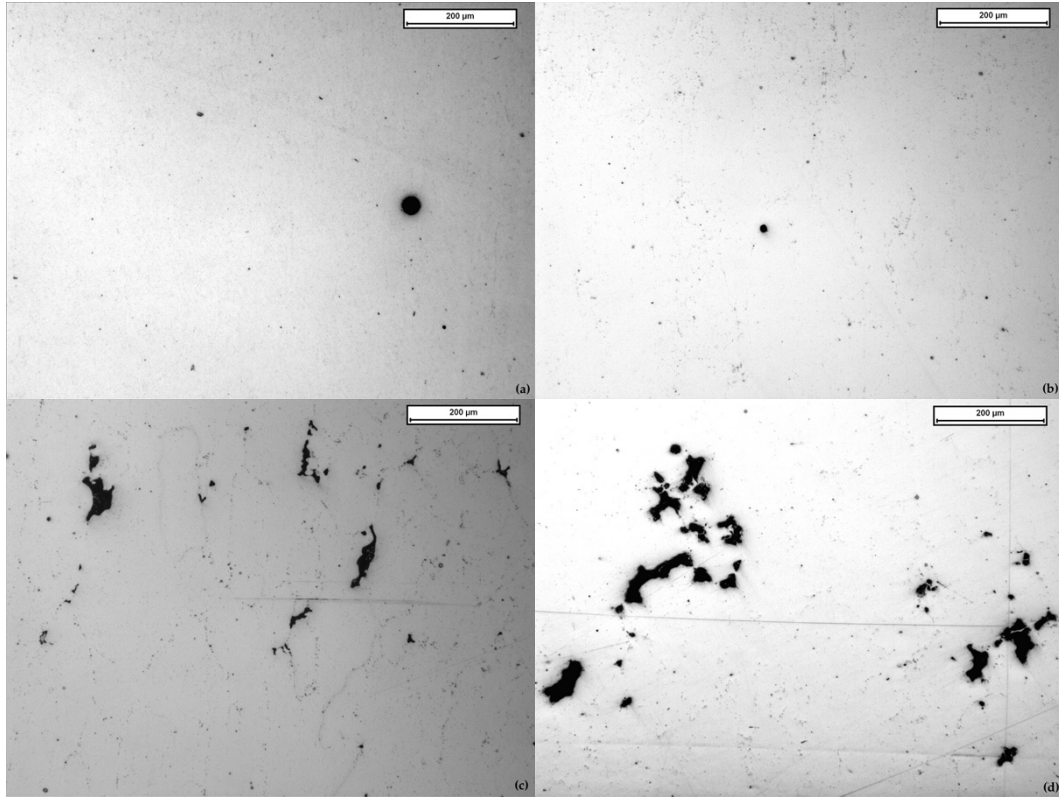
Figure 19:optical images of samples 1 (a), 2 (b), 3 (c), 4 (d) in xz plane.

The summaries defect analyses are reported in Table 6,Table 7,Table 8 and Table 9. From a first look can be seen that the average aspect ratios and defects radius, both used for flaws morphology characterization, largely differ from 1270 – 1280 °C temperatures to 1290 – 1300 °C. The same trend is visible for the average volumetric porosity of the samples, mainly in the xz plane.

Table 6: sample 1 defect analysis summary.

Sample 1	Av. aspect ratio	St. dev.	Av. vol. porosities [%]	St. dev.	Av. defects radius [μm]	St. dev
edge xy	1.520	0.600	0.057	0.058	10.556	5.174
core xy	1.550	0.675	0.061	0.051	11.287	4.221
edge xz	1.682	0.868	0.057	0.049	10.868	4.420
core xz	1.594	0.597	0.050	0.026	10.548	2.641

Table 7: sample 2 defect analysis summary.

Sample 2	Av. aspect ratio	St. dev.	Av. vol. porosities [%]	St. dev.	Av. defects radius [μm]	St. dev
edge xy	1.529	0.607	0.089	0.069	13.695	5.177
core xy	1.490	0.656	0.057	0.014	11.485	1.510
edge xz	1.556	0.643	0.048	0.013	10.507	1.543
core xz	1.523	0.609	0.021	0.009	6.887	1.525

Table 8: sample 3 defect analysis summary.

Sample 3	Av. aspect ratio	St. dev.	Av. vol. porosities [%]	St. dev.	Av. defects radius [μm]	St. dev
edge xy	1.815	0.831	0.065	0.021	12.293	1.975
core xy	1.678	0.720	0.042	0.017	9.738	2.005
edge xz	1.755	0.819	0.414	0.339	29.226	12.644
core xz	1.790	0.819	0.640	0.586	34.569	18.929

Table 9: sample 4 defect analysis summary.

Sample 4	Av. aspect ratio	St. dev.	Av. vol. porosities [%]	St. dev.	Av. defects radius [μm]	St. dev
edge xy	1.657	0.612	1.441	1.430	52.799	27.120
core xy	1.779	0.753	1.455	0.817	56.556	16.171
edge xz	1.800	0.889	1.739	0.842	62.423	16.036
core xz	1.918	3.147	1.018	0.594	46.996	14.655

An easier evaluation can be done seeing Figure 20 Figure 21 and Figure 22 that report a graphic comparison of all the samples mean aspect ratios, porosities radius and percentual porosity. In Figure 20 can be seen that with the increasing of temperatures from 1270 to 1280 °C there is a lowering of the mean aspect ratio of the flaws, such trend is inverted from 1290 to 1300 °C showing instead, a large increment. Same considerations are visible also for the average defect radii and percentual porosity (Figure 21,Figure 22). Thus, can be state that in ranges between 1290 °C and 1300 °C the presence of a plenty liquid phase produces larger porosities.
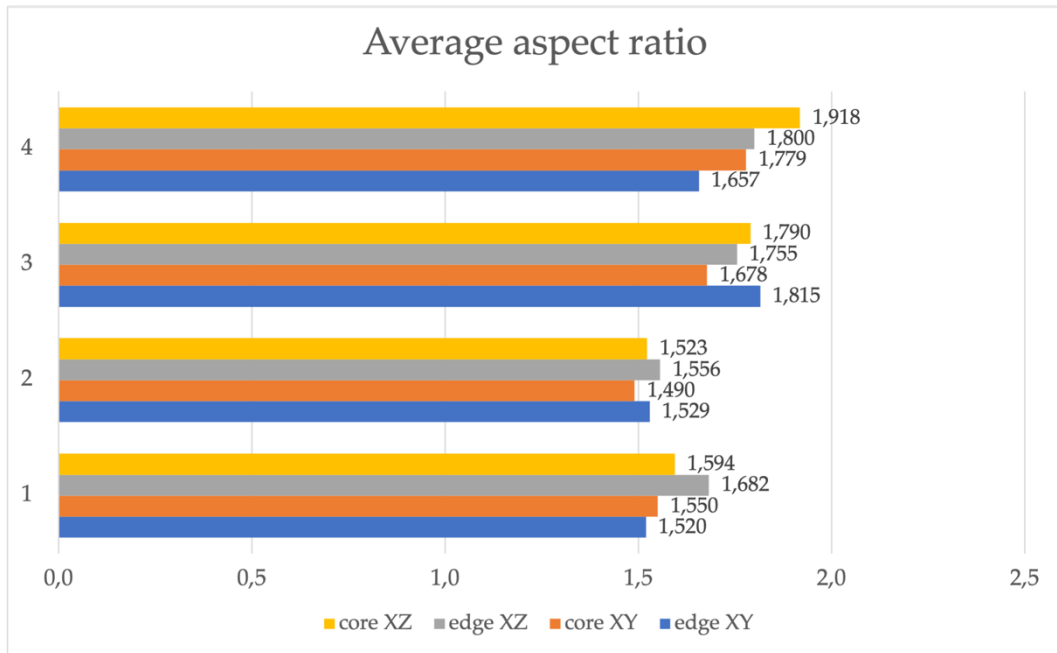
Figure 20: average aspect ratios comparison between non-standard heat-treated samples.
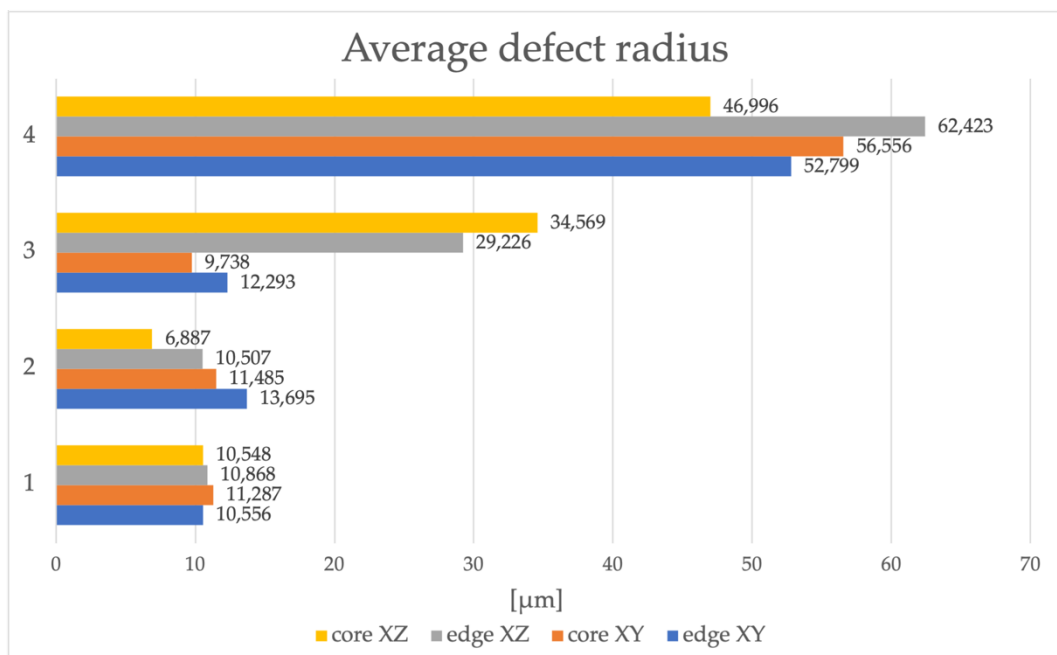
Figure 21: average porosity radii comparison between non-standard heat-treated samples.
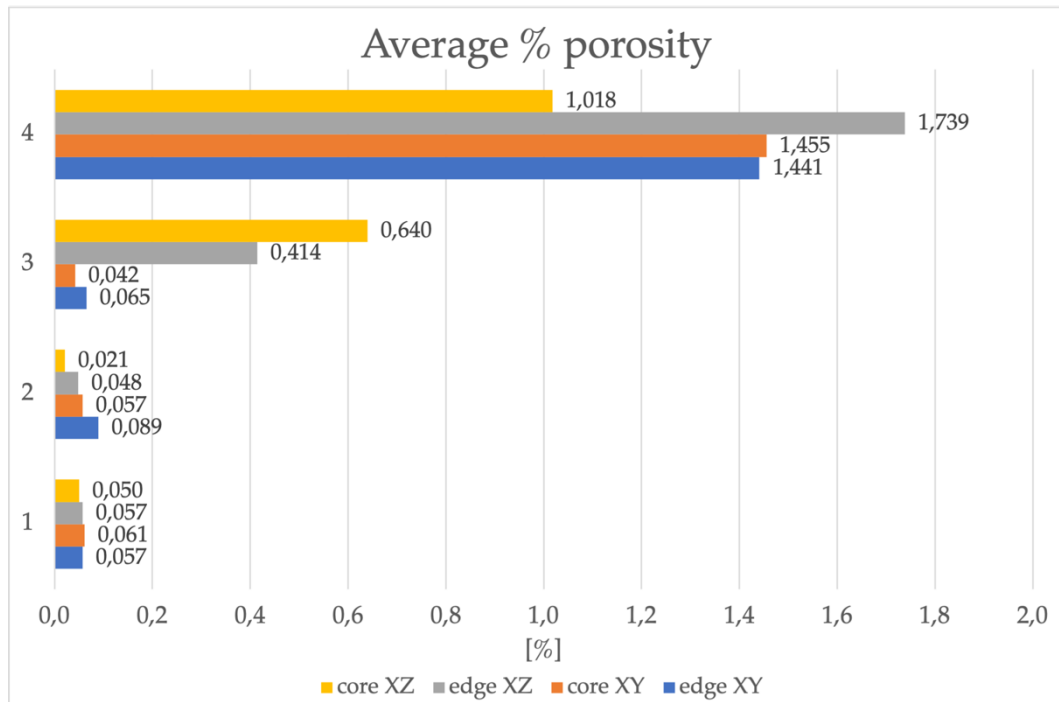
Figure 22: average volumetric percentual porosity comparison between non-standard heat-treated samples.

Grain structure evolution was evaluated through the procedure described in chapter 2. In

Figure 23 are reported for example images taken on xz plane of samples 1 (fig. 23 a), 2 (fig. 23 b), 3 (fig. 23 c) and 4 (fig. 23 d). Qualitatively can be assess that at 1270 °C (fig. 23 a) grains are very large but still show elongated shape due to building process; moreover, it can be noticed a bimodal size distribution of the grains i.e. simultaneously very large grains surrounded by small grains. With the increasing temperature grains become smaller until 1300 °C (fig. 23 d) at which grains definitely lose their oriented and elongated shape and also the bimodal distribution. A quantitative comparison is shown in Figure 24. Here can be seen that sample 1 has the higher average grain diameter value, especially in the xz plane. This result indicates that at 1270 °C IN738 is subjected to a substantial process of grain enlargement. With the increasing temperature there is a decreasing trend of the mean grain diameters, marked mainly in the xy oriented plane. It is also of interesting that larger mean grains diameters values are showed in the

xz plane, this could be justified by the preferential solidification of the grains along the building direction.
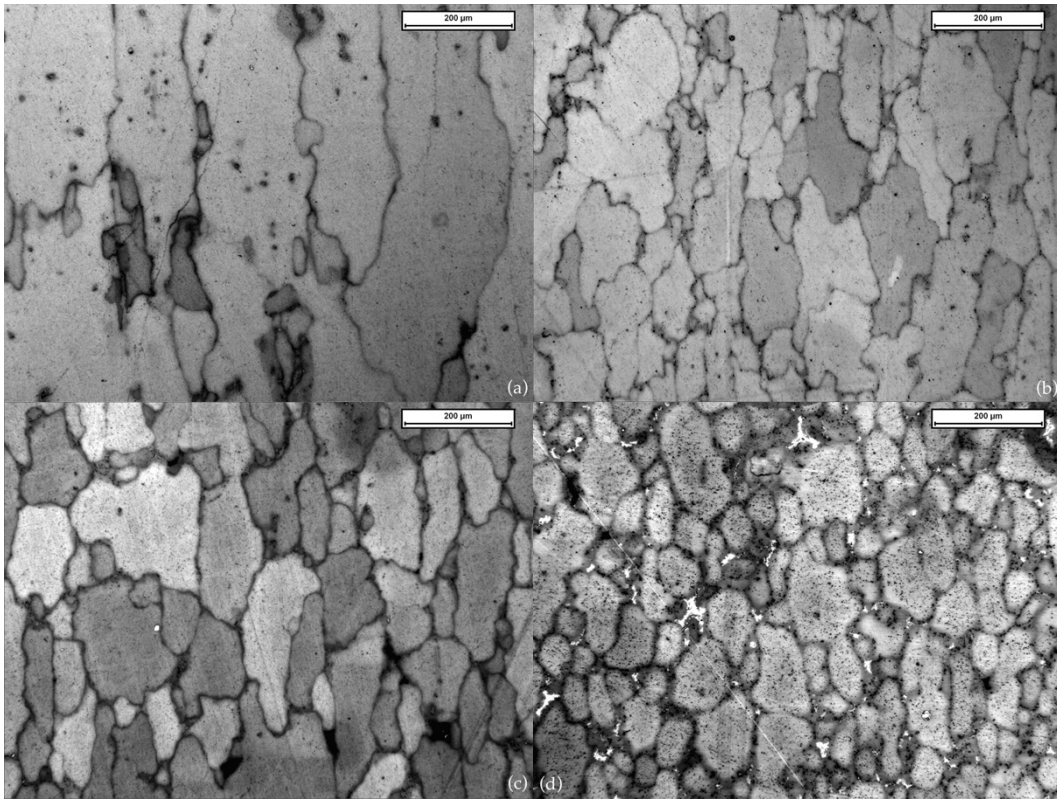
Figure 23: grain microstructure evolution of non-standard heat-treated samples 1 (a), 2 (b), 3 (c) and 4 (d).
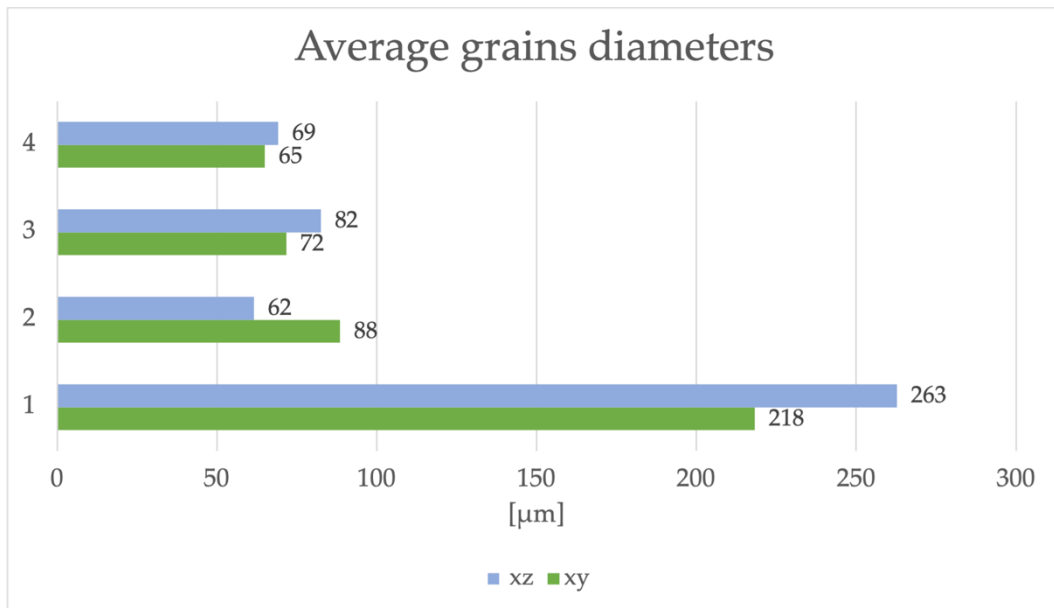
Figure 24: comparison of non-standard heat-treated average grain diameters.

3.4 HIP treatments

The main scope of this work of thesis, as previously described, is to evaluate the feasibility of hot isostatic pressing process above the solidus temperature of IN738 with 2 main objectives: obtain a defect-less or near-defect-less manufact with a coarser grain microstructure in respect to the as built state deriving from AM process. There are basically 3 fundamental parameters that can affect the material microstructure and also are possible to set in HIP processes: temperature, pressure and time. To do so, this experimental stage was implemented with a design of experiment (DOE) using the Taguchi method. In this manner it was possible to obtain consistent results with a lower number of trials. The realization of the DOE it's been done starting from the results of previous tests on the material, in fact, from the heat treatments and the DSC test were taken the best values of temperature and time parameters to perform super solidus HIP. At 1300 °C the material showed higher presence of liquid phase so, to prevent failure into the HIP furnace, this value of temperature was discarded. Instead, were used 1270, 1280 and 1290 as temperature values. As can be seen in the solutioning heat treatment, IN738 exhibits some recrystallization after 2 hours, beginning from this consideration 3 values for the time parameter are taken into account which are 80, 160 and 240 minutes. The last parameter to play with is pressure Standard pressure values for HIP processing from literature were applied as follows: 100, 125 and 150 MPa. Once chosen the values for the 3 main parameters the software calculates the optimal settings for each trial. A summary is reported in Table 10.

Sample	Temperature [°C]	Pressure [MPa]	Time [min.]
A	1290	150	240
B	1290	125	160
C	1290	100	80
D	1280	150	160
E	1280	125	80
F	1280	100	240
G	1270	150	80
H	1270	125	240
I	1270	100	160

Figure 25 shows heating and pressure ramps applied during the HIP process.
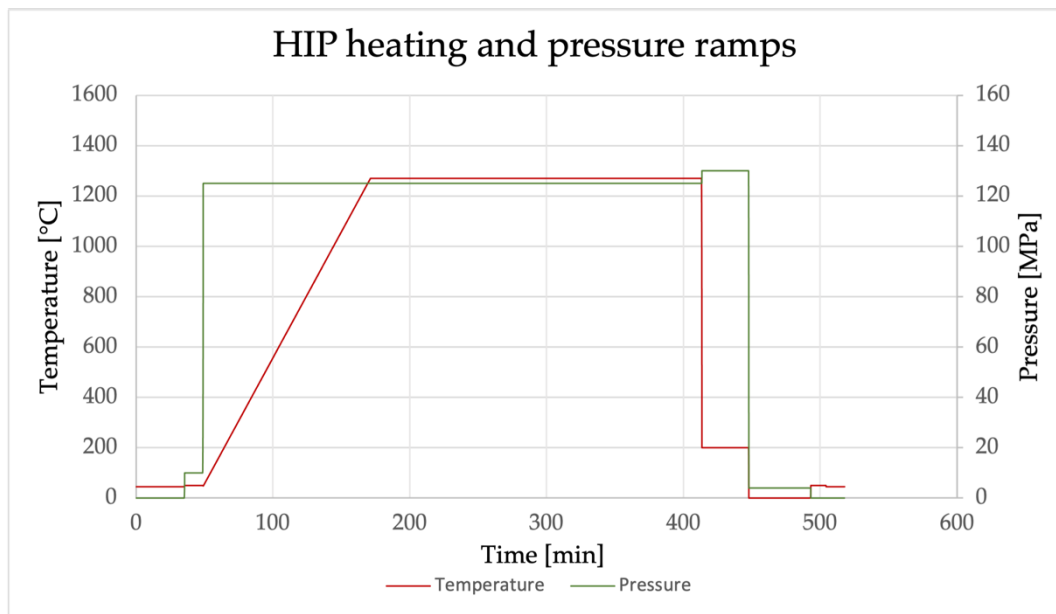
Figure 25: of heating and pressure ramps applied in HIP processes.

3.4.1 HIP analyses results

The results obtained from the HIP process, after the porosity and grains size analyses on samples, are shown in the following paragraphs.

Sample A)

Figure 26 shows illustrative images of the sample defectiveness in both near the surface of the sample (fig. 26 a) and core (fig. 26 b) location.
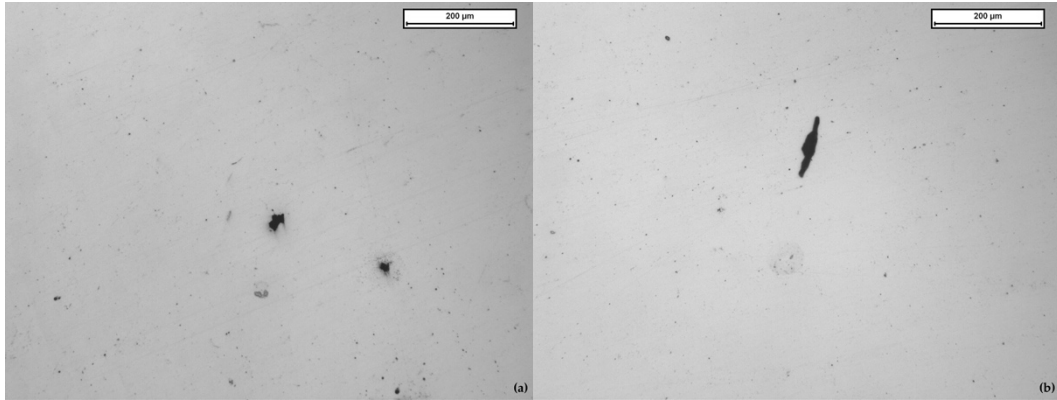
Figure 26: sample A density analysis at edge (a) and core (b) locations.

Table 11: sample A summary of defects analysis. reports the summarized data of the porosity analysis.
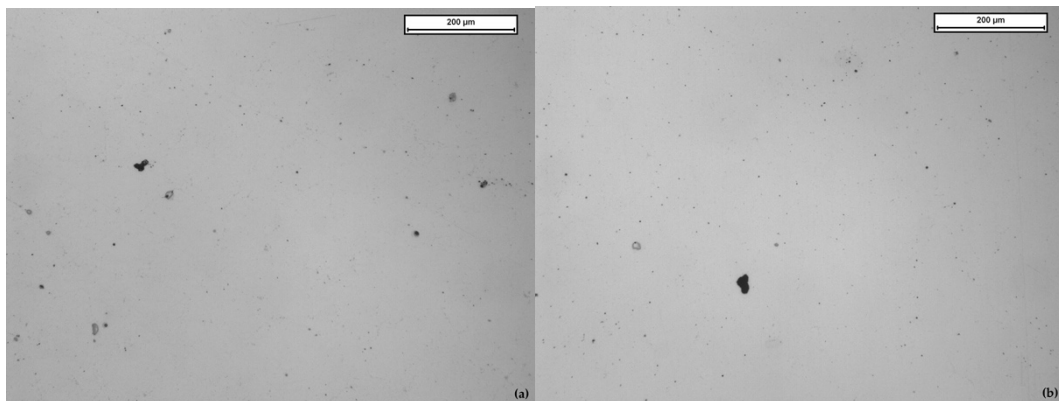
Table 11: sample A summary of defects analysis.

Sample A	Av. aspect ratio	St. dev.	Av. porosity [%]	St. dev.	Av. Feret diameter [μm]	St. dev.
edge	1.505	0.579	0.063	0.054	3.294	4.896
core	1.566	0.765	0.065	0.066	3.675	8.835

Results show that defects are mostly circular and uniformly distributed both at the surface and in the core. Feret equivalent diameter shows defects with an average size of ca. 3.4 mm. An example of the grain microstructure of sample A is report below. Figure 27 shows from a qualitative standpoint, a uniform grain size distribution.
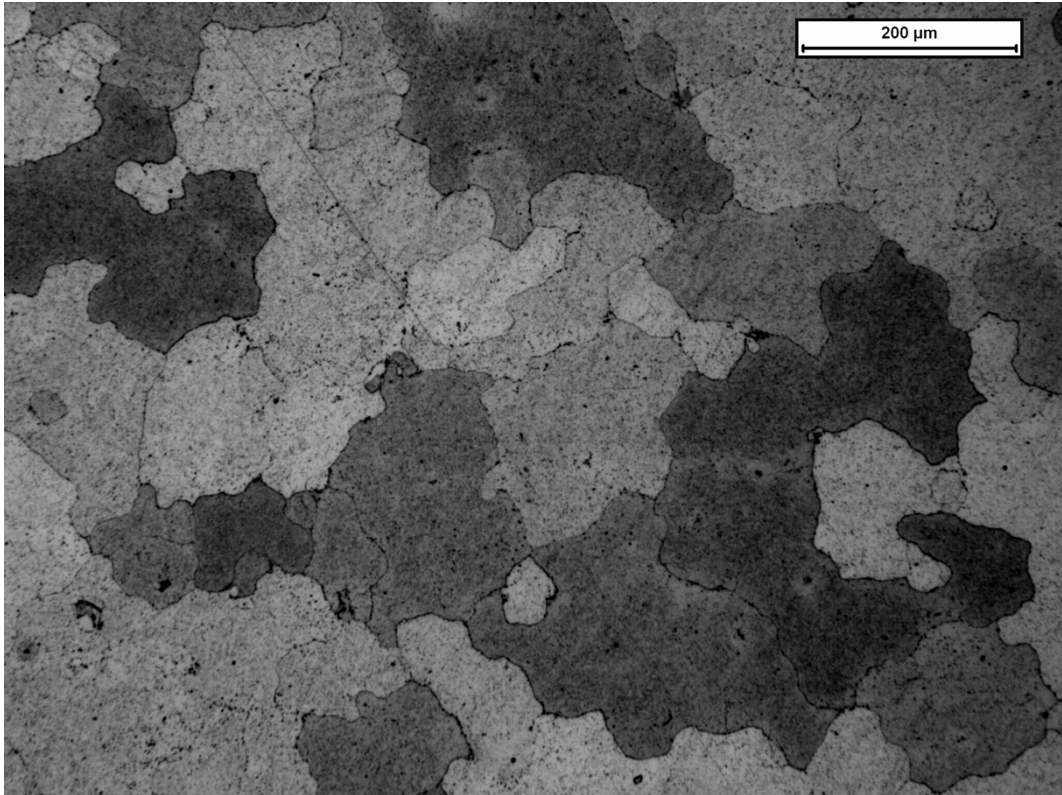
Figure 27: grain microstructure of sample A with LOM at 100x magnification.

From a quantitative point of view, it was calculated an average grains diameter of 132 μm. Figure 28 obtained by SEM analysis, shows intergranular carbides of the $M_{23}C_6$ type with squared geometry; it also possible to notice several intragranular precipitate secondary phases, probably MC type carbides.
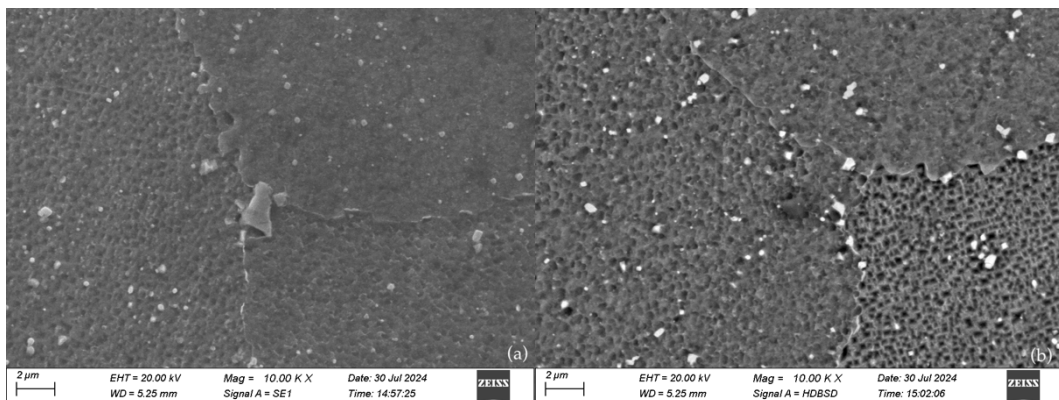
Figure 28: SE1 signal (a) and BSD signal (b) of secondary phases and MC carbides in sample A.

Figure 29 shows a non-melted particle (fig. 29 a) that can be a preferential site for segregation phenomena. Can also be seen in (fig. 29 b) an incipient melting region because the elongation of all the precipitates in one direction coincides with the formation of liquid and subsequent re-solidification. A $M_{23}C_6$ carbide, that can be distinguished by its elongated shape, is displayed inside the incipient melting region. Finally, can be stated that: despite its small size, traces of liquid that has re-hardened were spotted, which create a discontinuity in the material, even though it may have negligible effects.
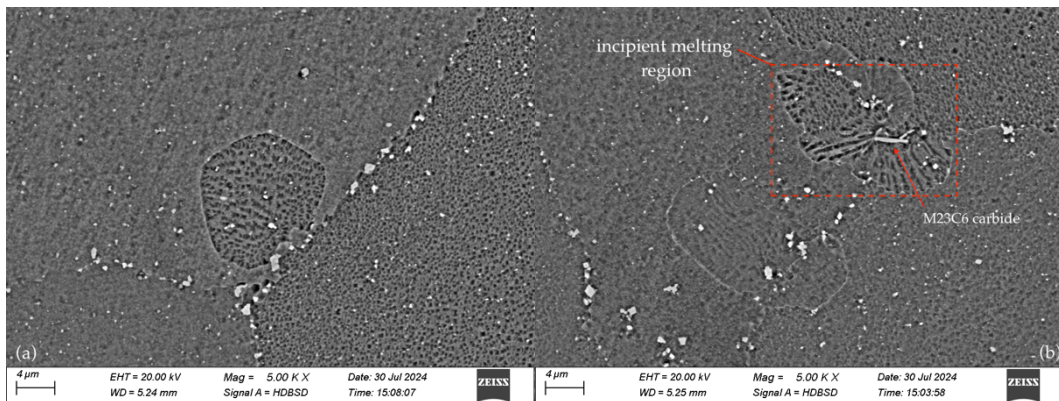
Figure 29: BSD signal of non-melted particle (a) and of incipient melting region (b) in sample A.

Sample B)

Figure 30 shows exemplificative defects images for both near-edge sample surface (fig. 30 a) and core (fig. 30 b). In Table 12 were also summarized the data from flaws analysis.

Figure 30: sample B density analysis at edge (a) and core (b) locations.

Sample B	Av. aspect ratio	St. dev.	Av. porosity [%]	St. dev.	Av. Feret diameter [μm]	St. dev.
edge	1.542	0.546	0.052	0.034	3.671	5.280
core	1.511	0.533	0.072	0.055	3.659	7.597

In general similar results of sample A are obtained for sample B concerning defects morphology. Only a particular mention on the average percentual porosity must be done since in this case pores are located especially in the sample core. Figure 31 of sample B shows a grain microstructure similar to that seen for sample A, so this leads to same qualitative considerations. It was calculated an average grains diameter of 110 μm, thus, for sample B the grains result finer compared to the grains in sample A.
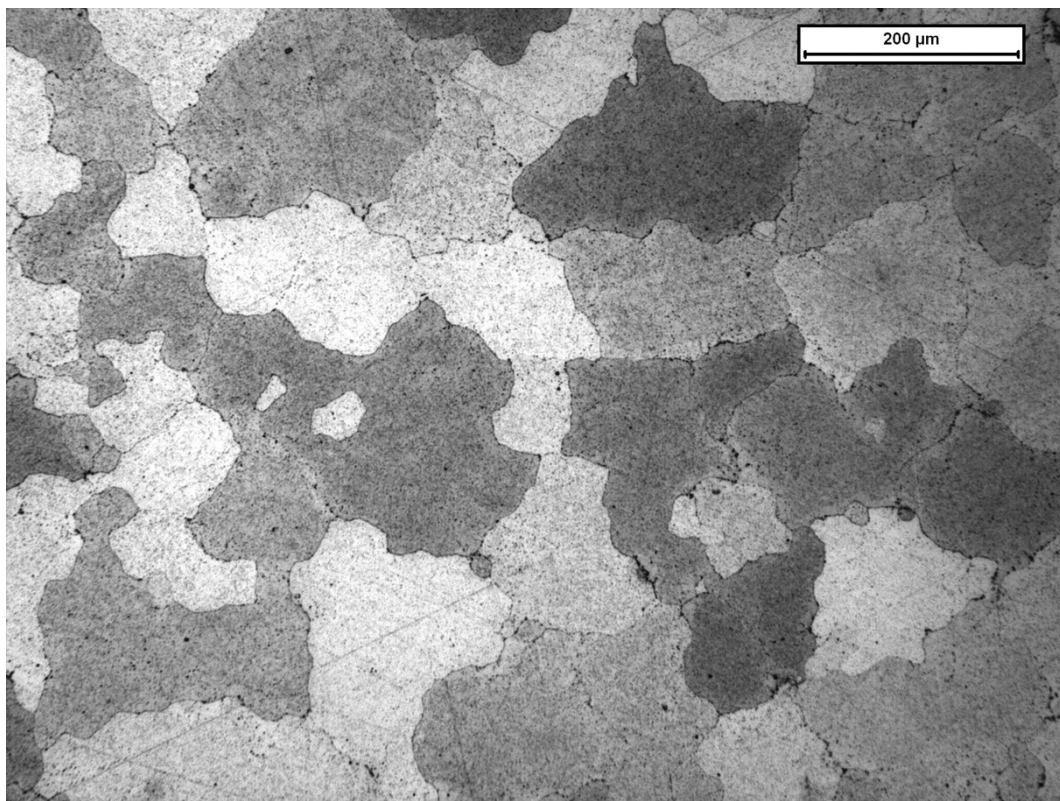
Figure 31: grain microstructure of sample B with LOM at 100x magnification.

SEM analysis in this case exhibit some interesting differences. Figure 32 (a) shows a pore surrounded by hard particles that could be identified as carbides. These particles, present at the pore edges, display as intense bright region when detected with backscattered electrons signal (fig. 32 b), that can

be reconducted to heavier elements than those forming the γ matrix phase. Thus, such tough phases present at the pore edges could be carbides formed during the HIP process which did not allow the pore to close.
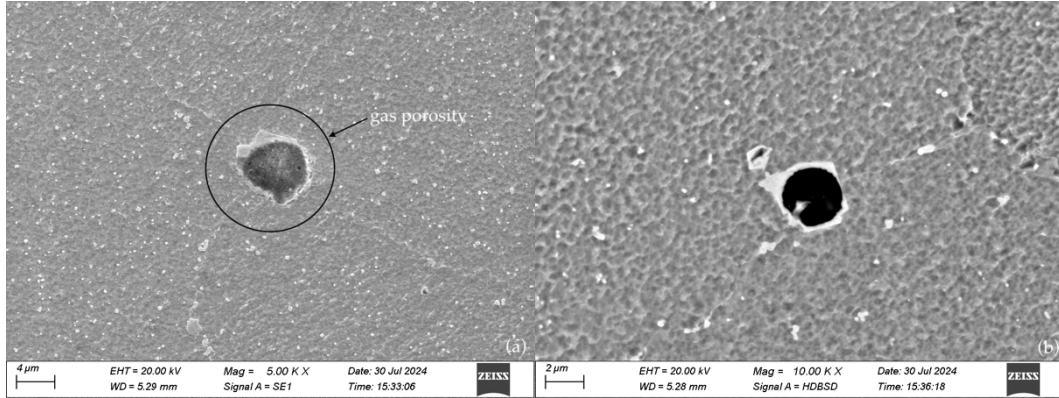
Figure 32: SE1 signal (a) and BSD signal (b) of gas porosity in sample B.

Figure 33 shows other gas unclosed porosities (fig. 33 a) and MC squared carbides (fig 33 b) present in sample B.
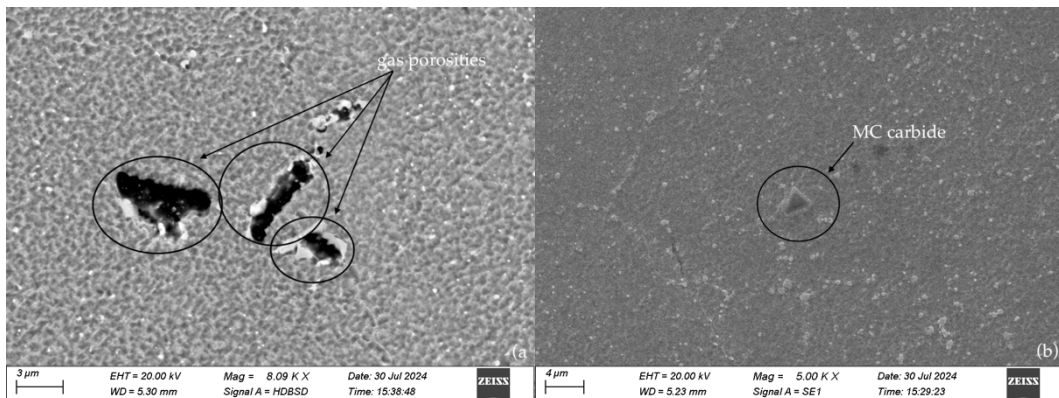

Figure 33: BSD signal of porosities (left) SE1 signal of MC carbides (right) in sample B.

Sample C)

Figure 34 shows illustrative images of the sample surfaces near the edge (fig. 34 a) and core (fig 34 b) location.
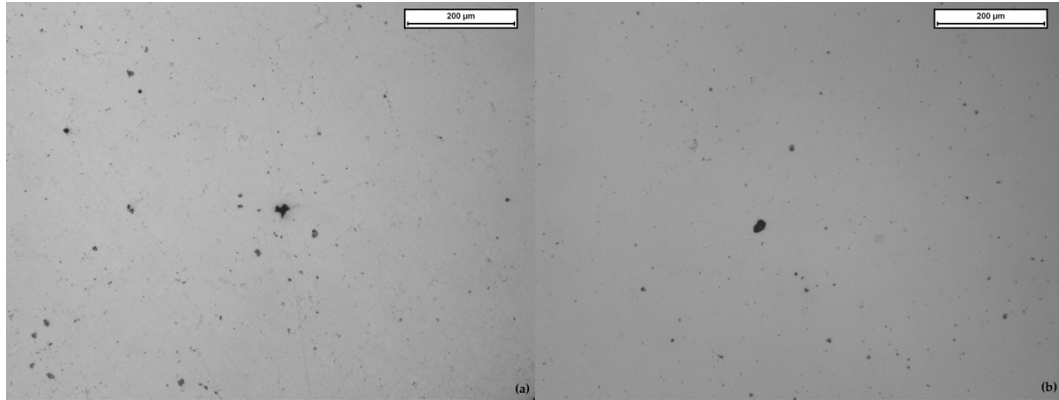
Figure 34: sample C density analysis near the edge (a) and core (b) locations.

In Table 13 were summarized the data of density analysis for sample C. As can be seen, mean aspect ratio and Feret diameter values remains very similar to the previously HIP treated samples. The mean value of porosity in this case remains similar in both edge and core zones as in sample A, moreover, this sample has the lowest defects fraction among the hipped ones at 1290 °C.

Table 13: sample C summary of defects analysis.

Sample C	Av. aspect ratio	St. dev.	Av. porosity [%]	St. dev.	Av. Feret diameter [μm]	St. dev.
edge	1.538	0.513	0.045	0.025	3.183	4.089
core	1.558	0.590	0.049	0.021	3.205	4.976

Figure 35 shows the microstructure of sample C, focusing on grain structure and size. Can be noticed that some grains are smaller respect to others resulting in a bimodal grain size distribution. From calculation are obtained an average grains diameter of 104 μm. It can be concluded that sample C has the smallest grain size of all 3 tests at this temperature.
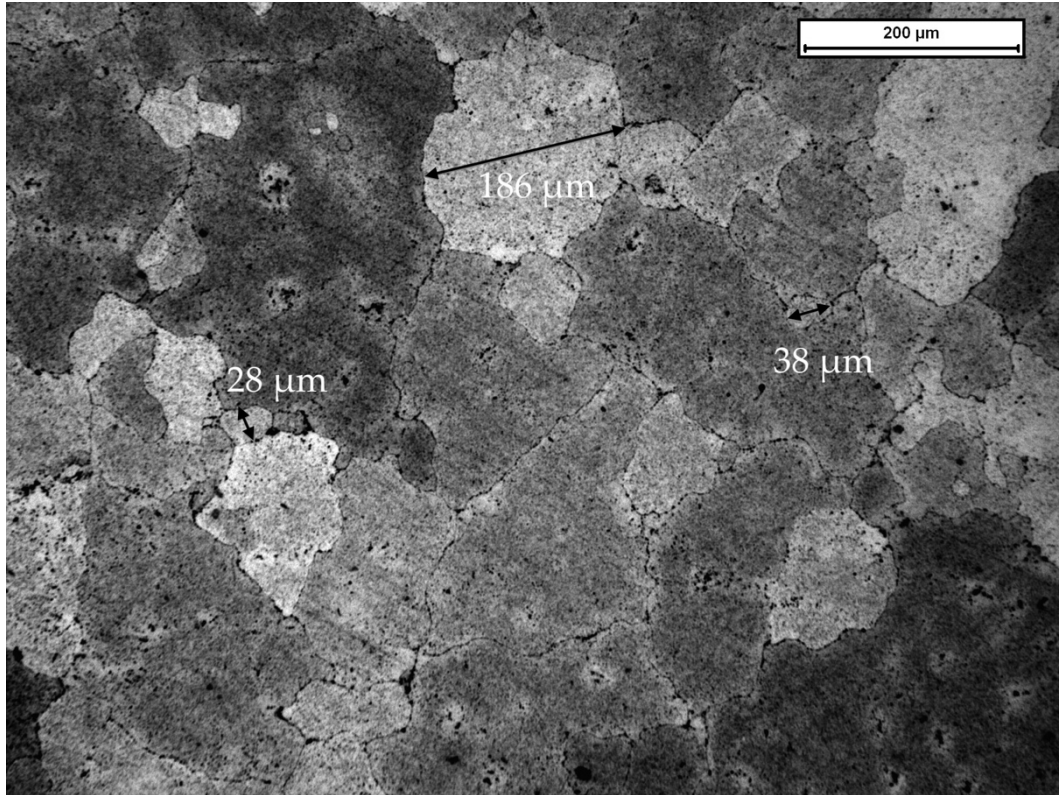
Figure 35: grain microstructure of sample C with LOM at 100x magnification.

Figure 36 from SEM analysis on C sample shows a large amount of secondary precipitate phases, almost within the grains. Secondary phases are mainly MC and M_6C carbides.
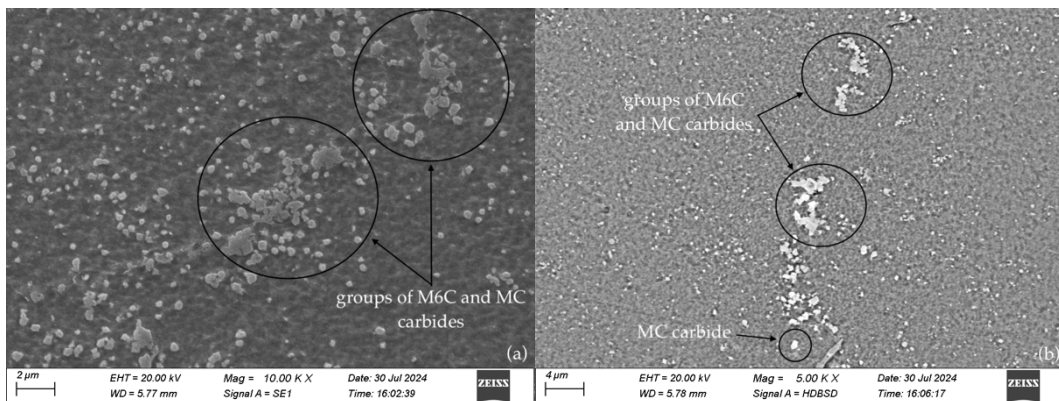

Figure 36: SEM images in SE1 signal (a) and BSD (b) signal of secondary precipitated phases in sample C.

In Figure 37 a mixed precipitate phase is observed: a carbo-nitride with a darker center, indicating the presence of lighter elements such as nitrogen, and a brighter edge, where heavier elements like carbon are concentrated.
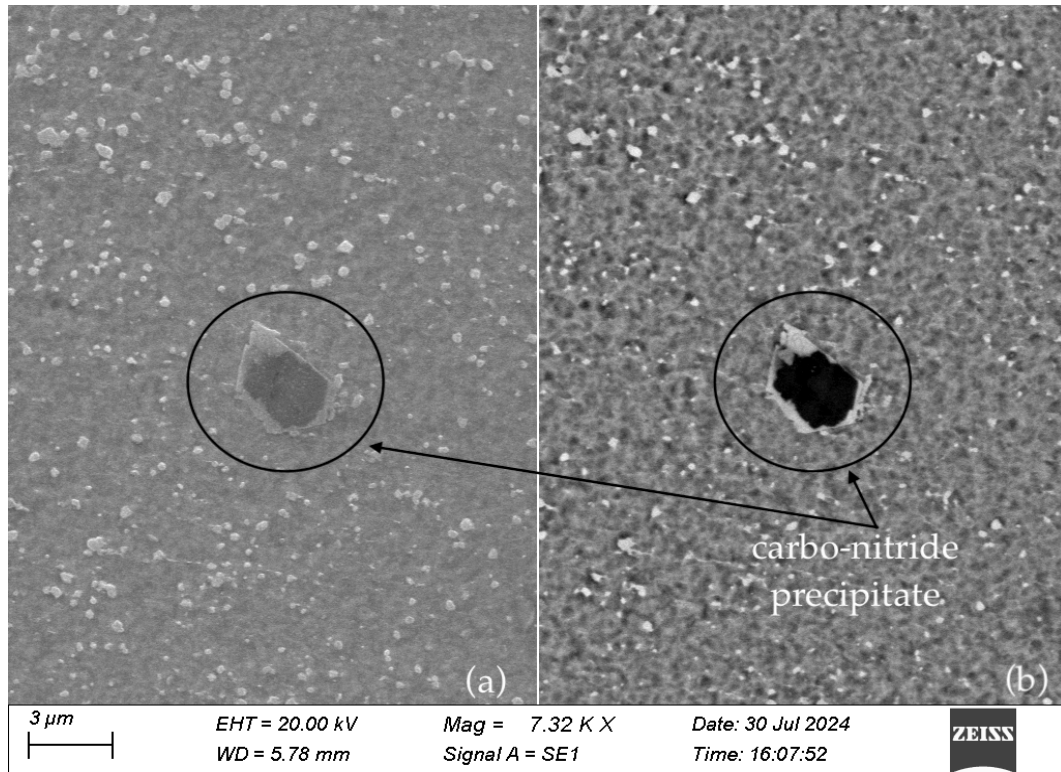
Figure 37: SE1 signal (left) and BSD signal (right) of carbonitride in sample C.

The next set of trials performed at 1280 °C will be reported in the following.

Sample D)

Figure 38 shows examples how sample D looks like on the surface in both near the edge (fig. 38 a) and core (fig. 38 b) zone.
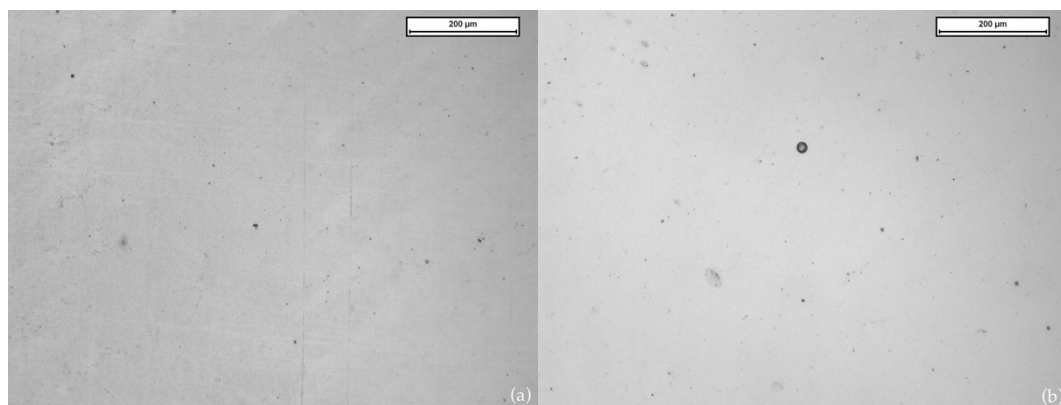

Figure 38: sample D density analysis at near-edge (a) and core (b) locations.

From the summary of defects analysis reported in Table 14 can be stated that defect morphology doesn't show any particular differences from the previous trials set conducted at 1290 °C: comparing average aspect ratios

results, all under 1.5, can be affirmed that mostly defects are gas porosities. A relevant lowering of the average percentual porosity can be seen both at edge and core zones.

Table 14: sample D summary of defects analysis.

Sample D	Av. aspect ratio	St. dev.	Av. porosity [%]	St. dev.	Av. Feret diameter [μm]	St. dev.
edge	1.455	0.460	0.025	0.011	3.102	2.741
core	1.492	0.605	0.031	0.011	3.190	3.284

Figure 39 shows that this thermal treatment had consistent effect on the grain size microstructure. Qualitatively grains appear large and well distributed, no bimodal grain size distribution can be seen, so results in a more homogeneous microstructure. Based on the calculations, the average grain diameter is 229 μm, which is 100 μm higher than the results obtained in the first three sets of trials.
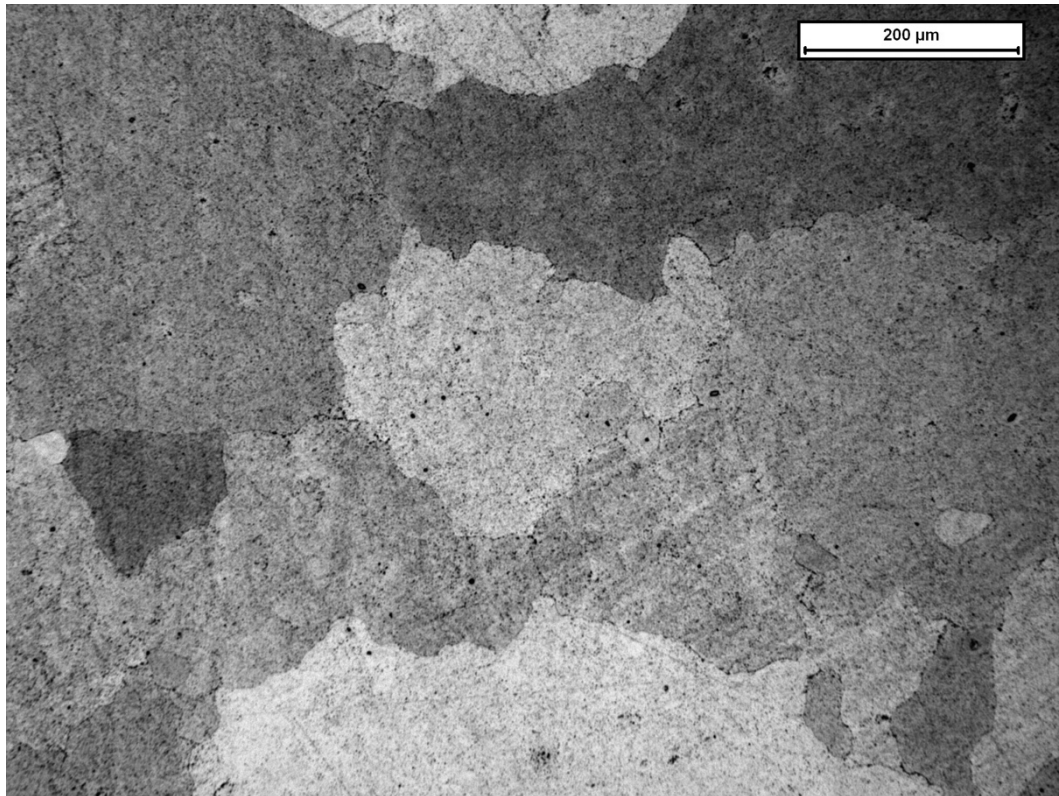

Figure 39: grain microstructure of sample D with LOM at 100x magnification.

Figure 40 presents SEM image analyses: (fig. 40 a) an example of a carbonitride precipitate at a grain boundary, which is larger than the one

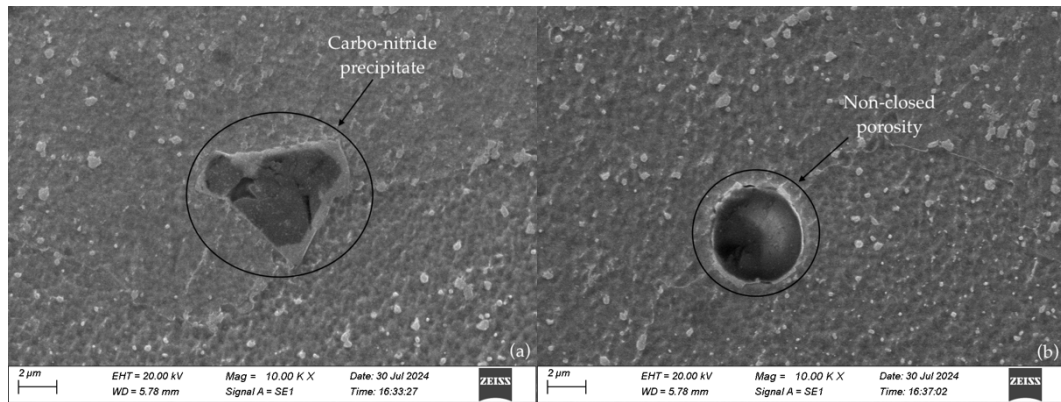observed in sample C, and (fig. 40 b) a non-closed pore caused by secondary precipitate phases at the edge.

Figure 40: SE1 signal of MC carbonitride (a) and pore (right) in sample D.

In Figure 41are shown several carbides of MC and $M_{23}C_6$ type decorating the grain boundary marked with red dotted line.
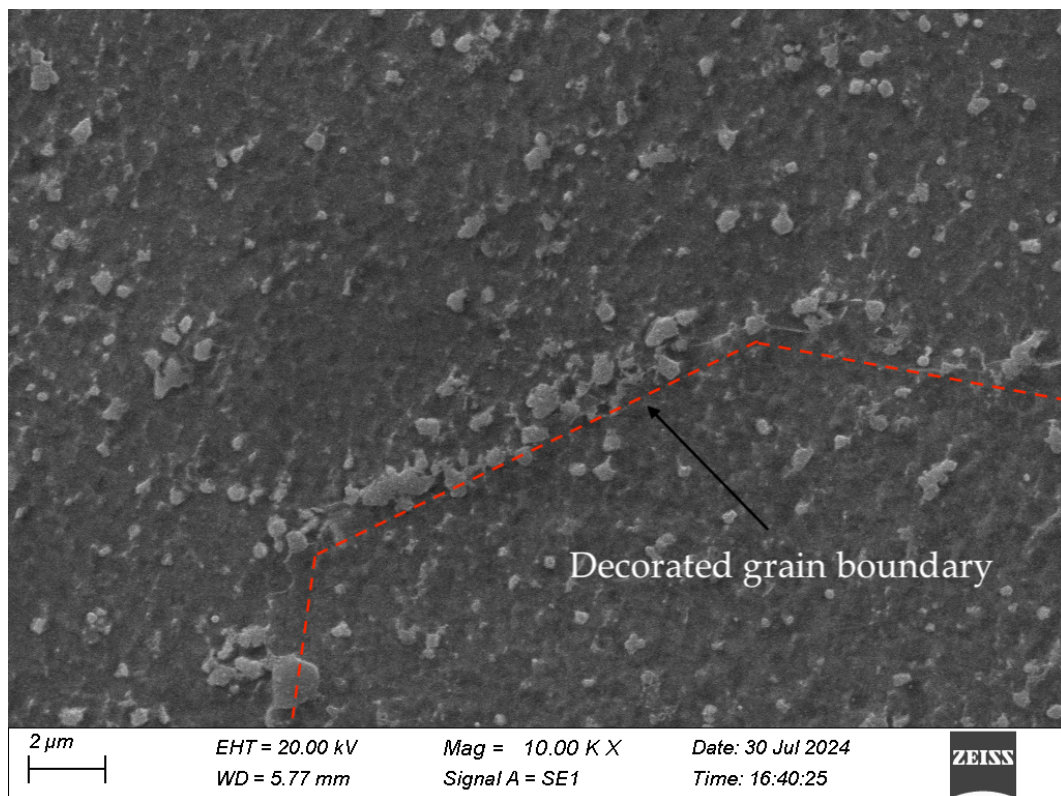

Figure 41: SE1 signal carbides decorating the grain boundary in sample D.

Figure 42 shows the one that could be an initial melting region: one possible hypothesis is that micro pores in the darker areas probably have acted as

nucleator points for the incipient melting mechanism; another hypothesis is that there was a γ - γ' eutectic phase that began to melt but not completely, and then subsequently solidified again.
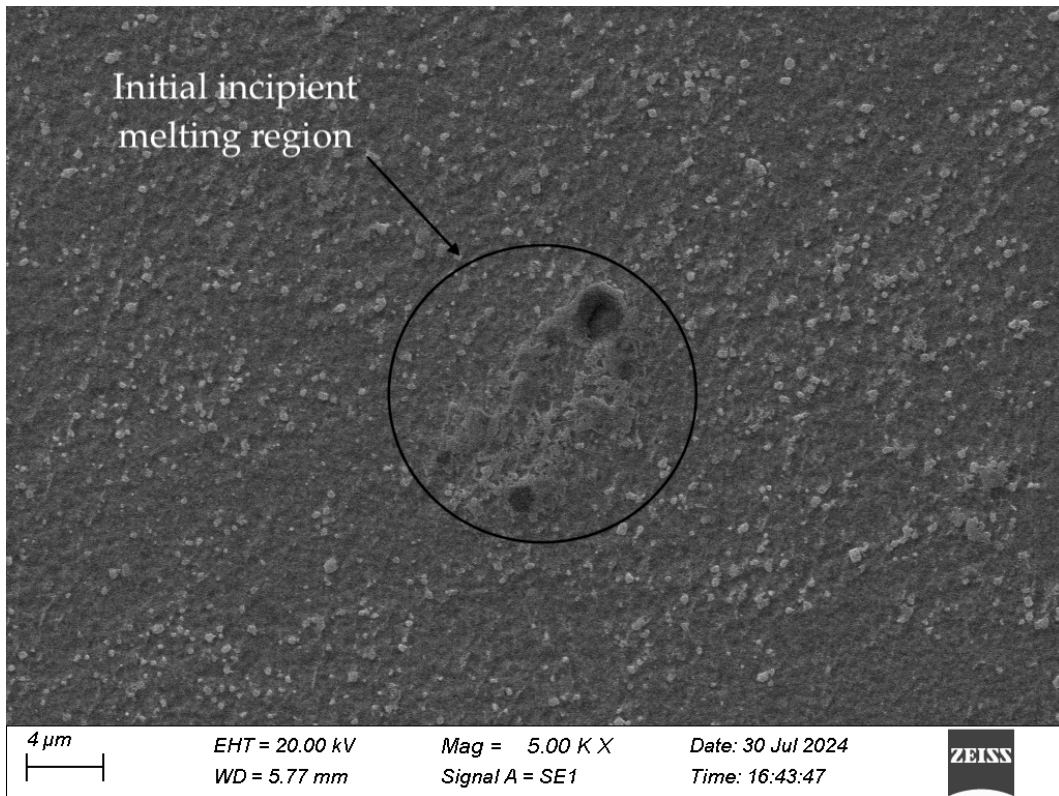

Figure 42: initial incipient melting region in sample D.

Sample E)

Figure 43 shows surface images of sample E near edge (fig. 43 a) and core (fig. 43 b) zone.
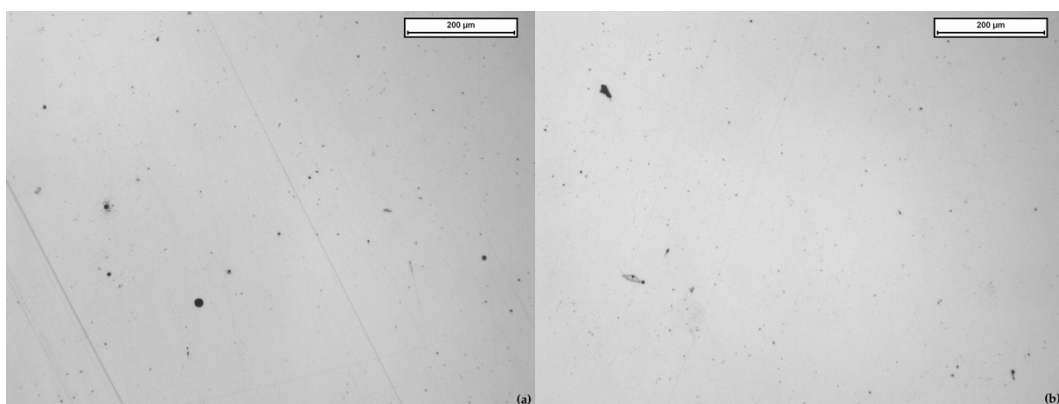

Figure 43: sample E density analysis at near-edge (a) and core (b) locations.

Table 15 shows the summary of defects analyses of sample E. By noticing values related to defects morphology: average aspect ratio and Feret diameter, can be stated that defects shape of sample E remain similar to the previous samples. The average volume fraction porosity is 43% higher than what resulted in sample D.

Table 15: sample E summary of defects analysis.

Sample E	Av. aspect ratio	St. dev.	Av. porosity [%]	St. dev.	Av. Feret diameter [μm]	St. dev.
edge	1.460	0.554	0.039	0.017	3.493	2.736
core	1.443	0.499	0.041	0.019	3.453	3.119

Figure 44 shows the grain microstructure of sample E. It can be stated that, even here, there is the presence of big grains concurrently of small grain resulting in a bimodal grain size distribution. Calculation of the average grains diameter result in a diameter of 157 μm, a much lower value respect than obtained for sample D. This last result can be related to carbides or/and γ′ pinning mechanisms which lead to grains growth blocking effect [66]. This hypothesis should be verified through SEM analyses results.
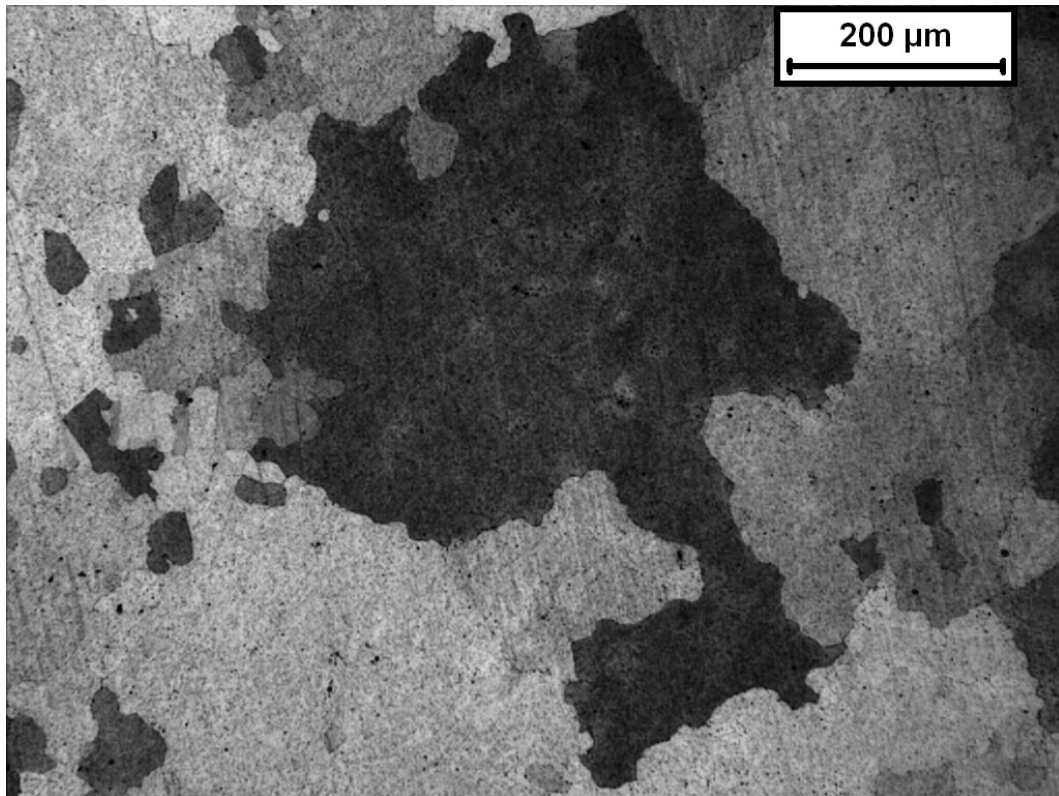

Figure 44: grain microstructure of sample E with LOM at 100x magnification.

Figure 45 shows SEM analyses images of sample E. Even in this case is notable the presence of MC and M_6C type carbides and carbonitride (fig. 45 a) and non-closed pore (fig. 45 b).
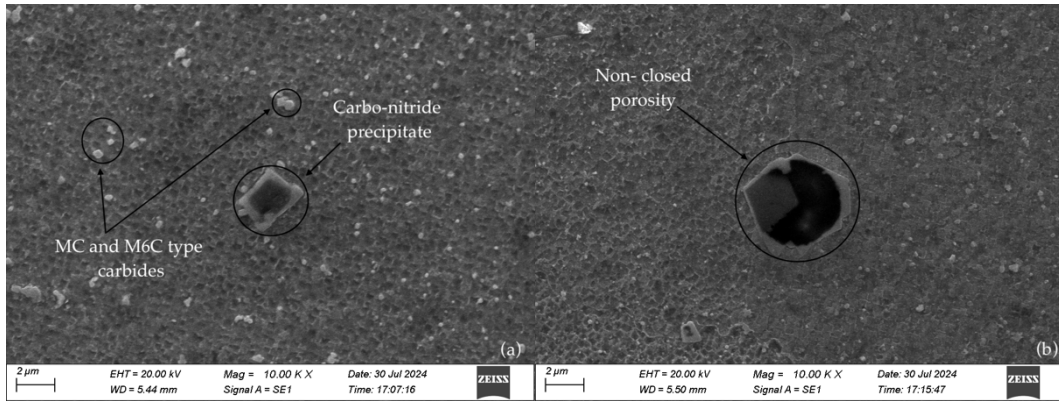

Figure 45: SE1 signal of MC and M_6C carbides and carbonitride (a) and non-closed pore (b) in sample E.

Figure 46 shows primary γ′ phase in cubic shape which was highlighted by the chemical etching and well visible in the darker area. The fact that γ′ phase is clearly detected through SEM analyses could justified the poor grains enlargement abovementioned.

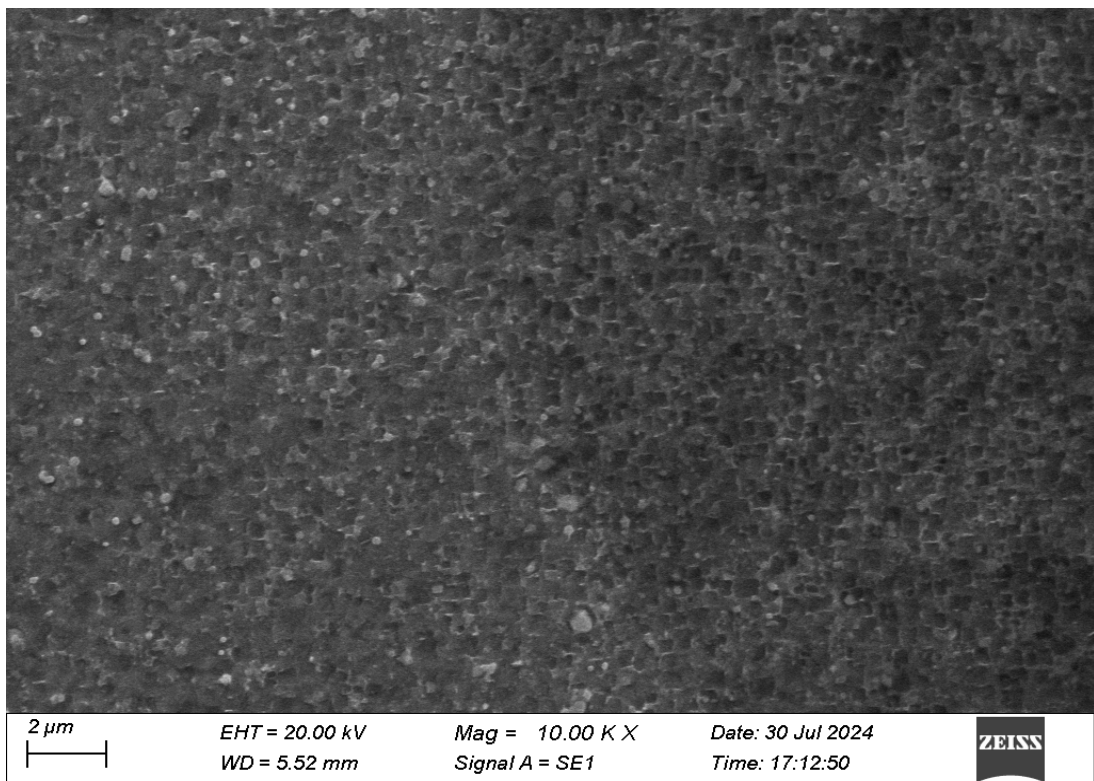*Figure 46:SE1 signal of primary γ′ in sample E.*

Sample F)

Figure 47 shows defects surface analyses of sample F both on the near-edge surface (fig. 47 a) and the core (fig. 47 b) location.
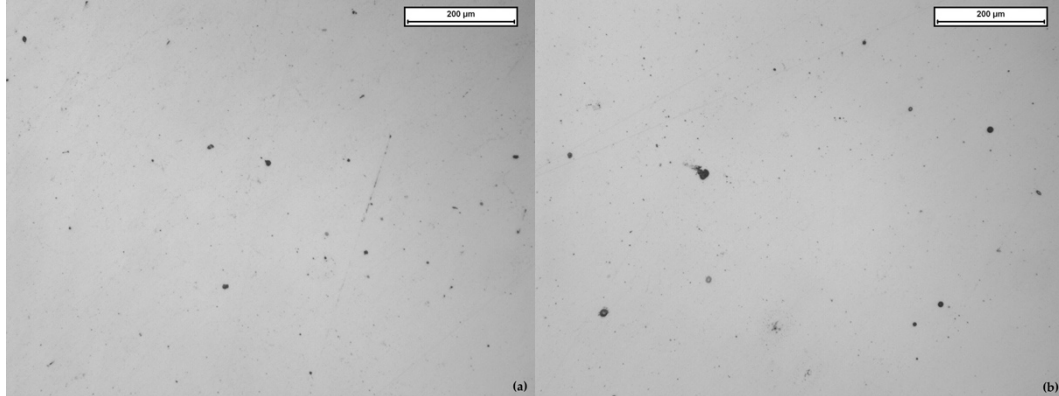

Figure 47: sample F density analysis at near-edge (a) and core (b) locations.

Table 16 reports the summary of the defect analysis of sample F. The same morphology consideration stated before for other samples are valid. Sample F presents the highest average volume fraction porosity among samples of this set of trials treated at 1280 °C. Moreover, it can be noticed that mostly of defects are concentrated near the surface edge of the specimen.

Table 16: sample F summary of defects analysis.

Sample F	Av. aspect ratio	St. dev.	Av. porosity [%]	St. dev.	Av. Feret diameter [μm]	St. dev.
edge	1.423	0.548	0.122	0.177	3.999	3.958
core	1.434	0.423	0.058	0.031	3.129	3.528

Figure 48 shows grain microstructure of sample F. It exhibits large grains as in sample D with qualitatively no bimodal grain size distribution. Based on the calculations, the average grain diameter is estimated to be 174 μm, which falls between the average grain diameters of the previous trials: smaller than sample D but larger than sample E.
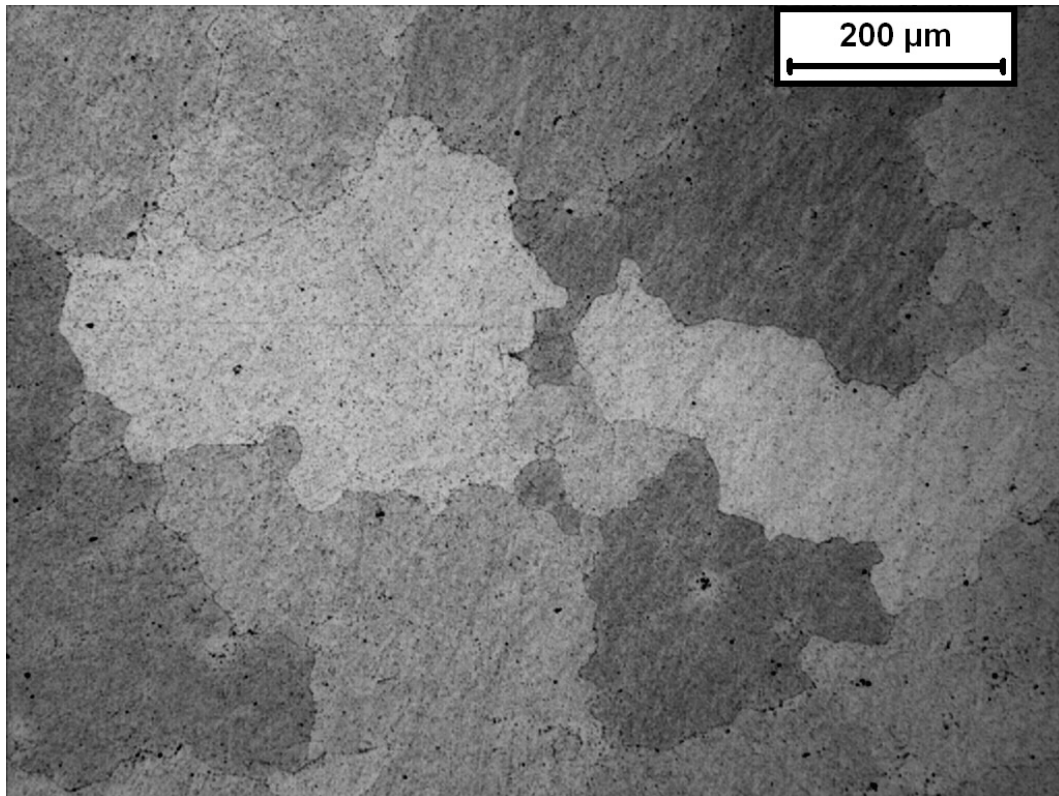
Figure 48:grain microstructure of sample F with LOM at 100x magnification.

Figure 49 shows SEM images detected via secondary electrons of sample F. Primary precipitates phases are visible in fig. 49 (a) including MC, $M_{23}C_6$ and M_6C type carbides. In fig. 49 (b) can be noticed a large $M_{23}C_6$ intragranular carbide which could negatively affect the mechanical properties of the alloy.
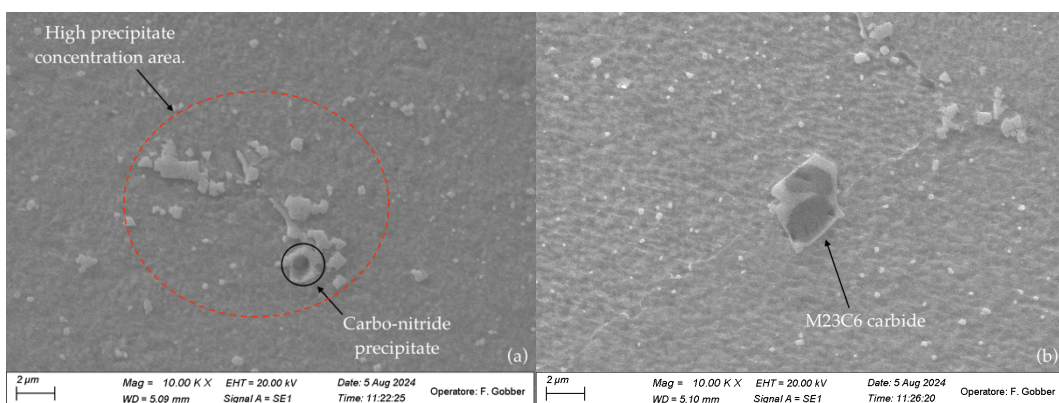

Figure 49: SE1 detected signal of high precipitation zone (a) and $M_{23}C_6$ carbide (b) in sample F.

Figure 50 shows a triple point of junction between grains, also are visible decorated grain boundaries with $M_{23}C_6$. Grains decorated in this manner

can improve the creep resistance, preventing the hot viscous sliding at high temperature behave like anchorages between the grains.
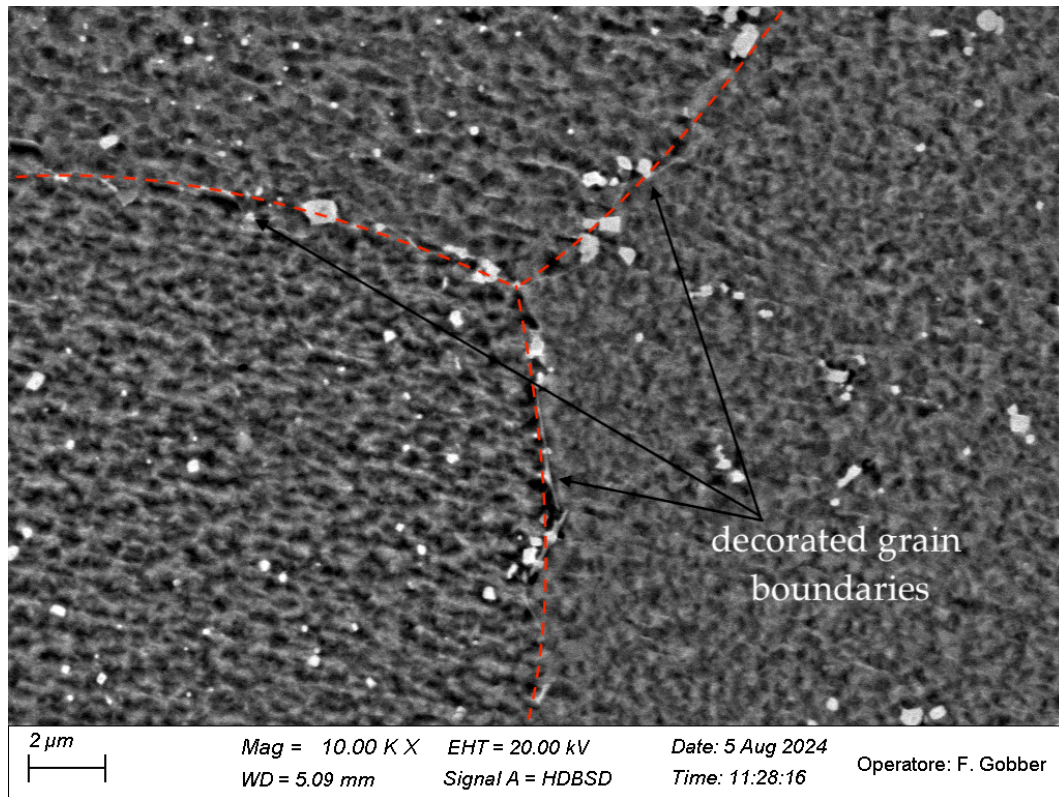

Figure 50: BDS detected signal of decorated grain boundaries on sample F surface.

Figure 51 shows a large non-closed porosity, especially with backscattered electron signal it is possible to see in the brighter areas along the pore edge the precipitate phases that not allow the pore to close. Pores non closed with this acicular morphology are detrimental for mechanical properties as the behave as preferential nucleation point for cracks in the material. The fact that a hard phase is present on the pore edge could lead to 2 hypothetic cases: the first is a slightly increase of the yielding stress need to allow the cracks nucleation leading to an improvement of the mechanical properties. The latter is an early cracks nucleation because of the intrinsic fragile nature of this precipitates. Stress rupture testing is mandatory in order to better understand and verifying in which measure these pore edge precipitate phases could affect the mechanical behavior of IN738.
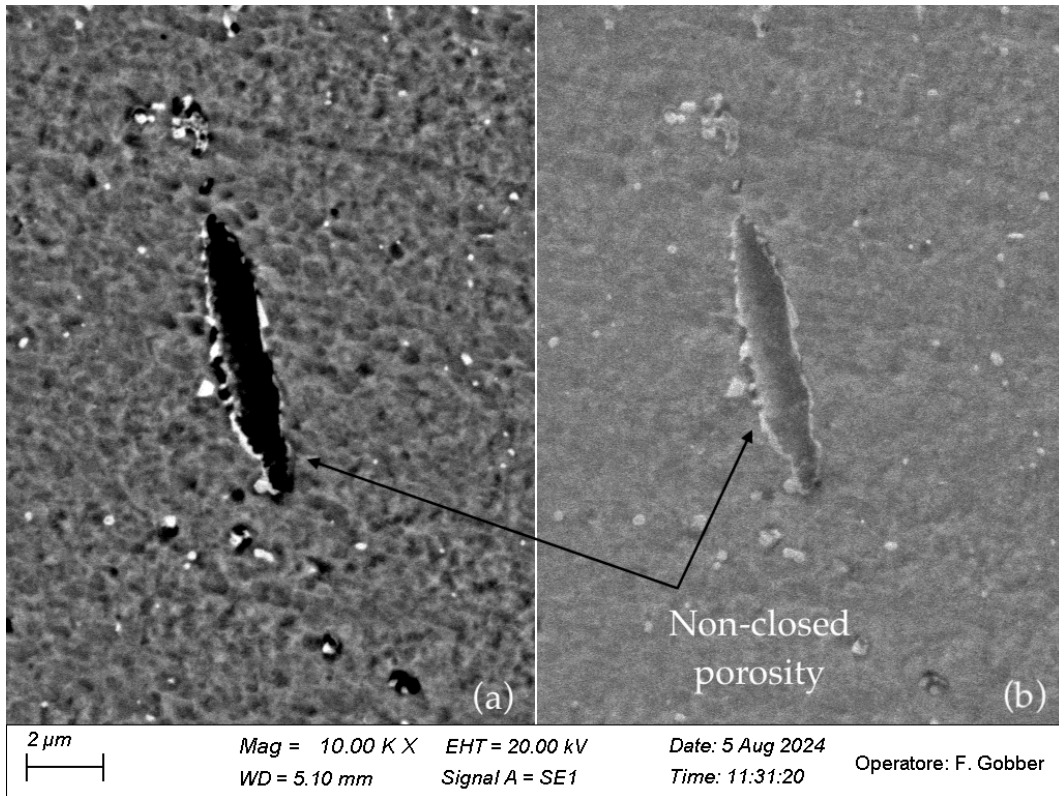
Figure 51: BSD (a) and SE1 (b) signal of non-closed porosity in sample F.

The results of the last set of trials at a temperature of 1270 °C are reported below.

Sample G)

Figure 52 shows images of sample G surface in both near-edge (fig. 52 a) and core (fig. 52 b). From a qualitative standpoint, can be already stated that sample G presents more flaws.
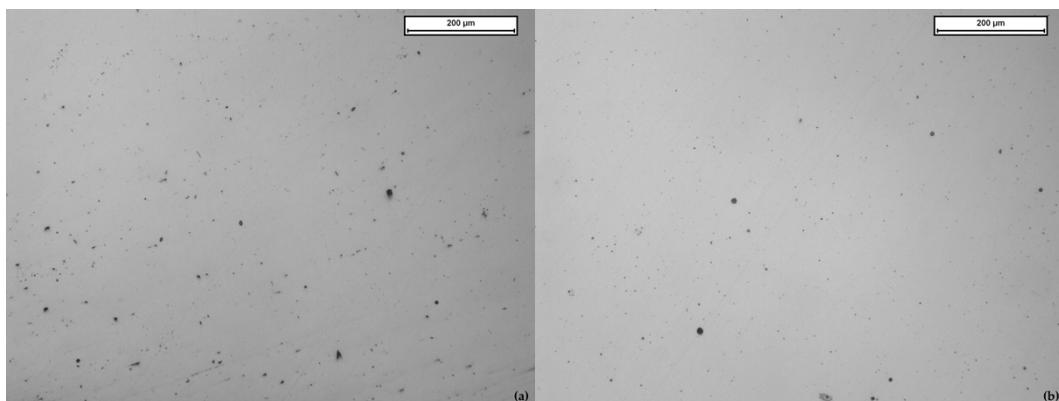

Figure 52: sample G density analysis at near-edge (a) and core (b) locations.

Table 17 shows a summary of defects analysis of sample G. The calculations reported in the summary confirm the higher defectivity of sample G. Defect morphology is similar to that observed in previous samples, mostly rounded and evenly distributed.

Table 17: sample G summary of defects analysis.

Sample G	Av. aspect ratio	St. dev.	Av. porosity [%]	St. dev.	Av. Feret diameter [μm]	St. dev.
edge	1.505	0.572	0.161	0.156	3.124	5.721
core	1.503	0.492	0.051	0.021	2.398	2.511

Figure 53 shows the grain microstructure of sample G. Qualitatively it can be noticed that grains size is finer in respect of the other set trials conducted at 1290 and 1280 °C. It can be also noticed that, in this treatment, grains maintain remain similar to that resulting from the AM process. Additional images must be taken at 200x magnification for evaluation of the average grains diameter resulting in 21 μm. This last result can be justified by the previous information collected in chapter 1: grains do not recrystallize because of the insufficient temperature applied in the HIP process. Furthermore, as seen in the non-standard heat treatments, at 1270 °C liquid formation due to incipient melting is minimal, thus, diffusive mechanism processes could only occur via solid state. Moreover, pinning mechanism could also have affected the grains growth.
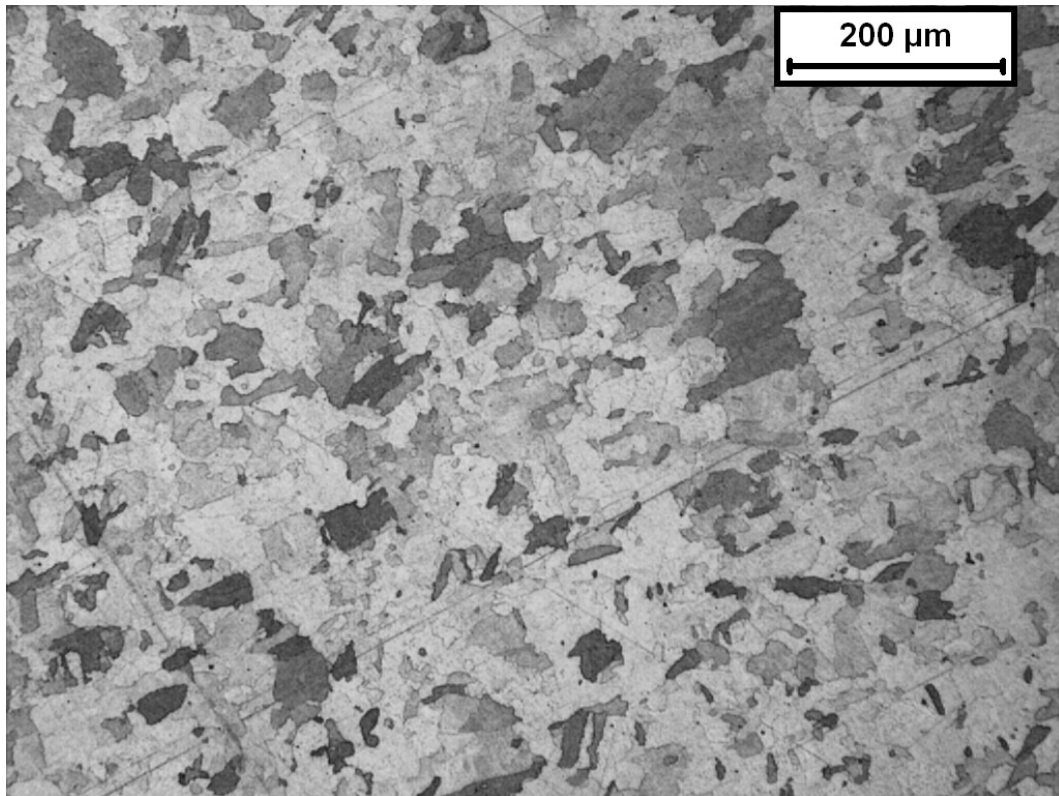
Figure 53: grain microstructure of sample G with LOM at 100x magnification.

Figure 54 shows SEM analyses images of sample G. In fig. 54 (a) and (b) can be noticed a carbo-nitride precipitate, like in the previous samples. Of interest is the overall microstructure that can be seen in fig. 54 (c), indeed, can be stated that a plenty of MC and $M_{23}C_6$ type carbides of small dimensions precipitate in sample F. Exceptions are $M_{23}C_6$ type carbides showed in fig. 54 (c), these larger and intergranular carbides could lead to detrimental effect on the mechanical properties of the superalloy.
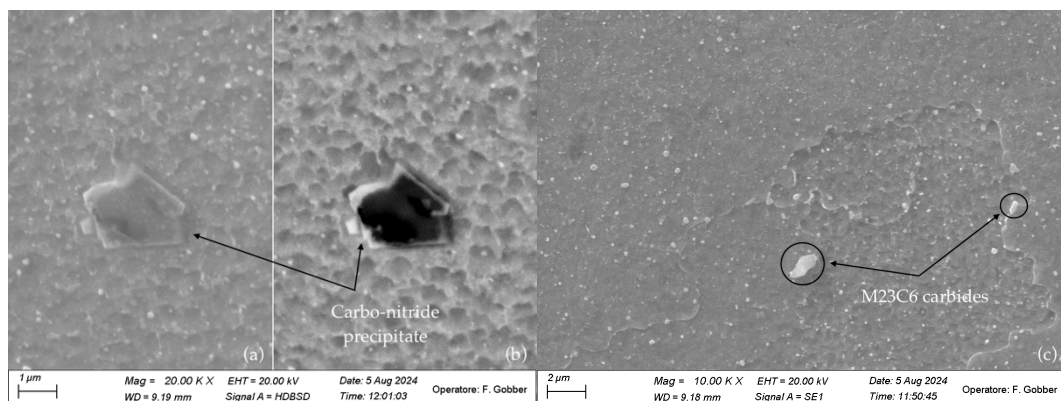

Figure 54:SE1 (a) and BSD (b) signal of carbo-nitride; $M_{23}C_6$ intergranular carbides (c) in sample G.

Figure 55 better shows the microstructure and the decorated grain boundaries in sample G. Uniformly precipitated phases of mainly $M_{23}C_6$ type small carbides can explain the previously seen grain microstructure.

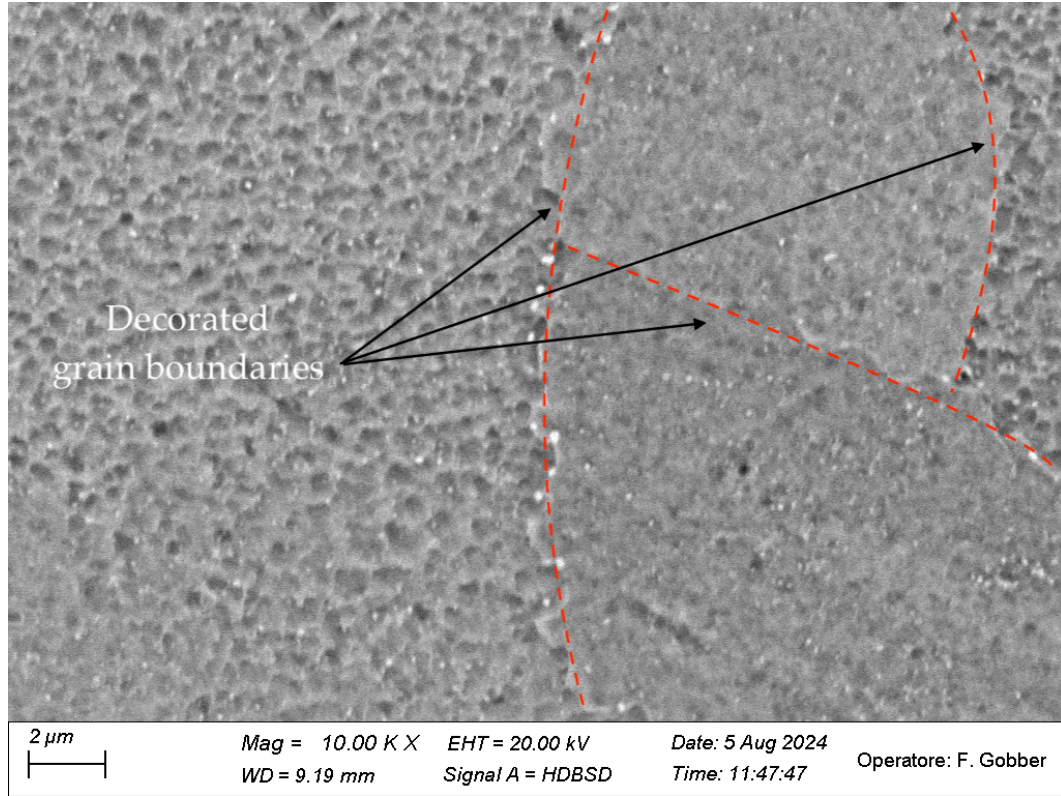*Figure 55: decorated grain boundaries in sample G.*

Figure 56 shows the γ′ cuboidal phase in sample G. the presence of abundant γ′ phase could also explain the grain microstructure of sample G. The combinate pinning effect of γ′ and precipitate intergranular carbides could prevent the grain growth during the HIP process. Furthermore, this mechanism may have been affected by the low temperature.
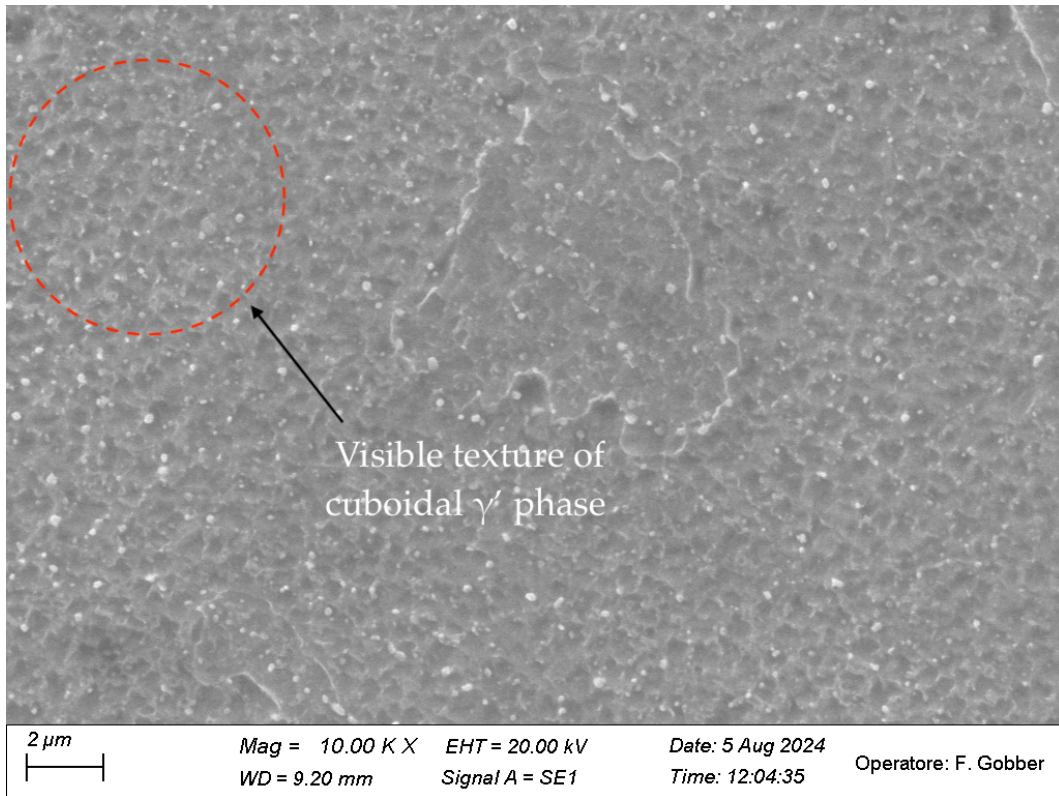
Figure 56: particular of the cuboidal γ′ phase in sample G.

Sample H)

Figure 57 shows sample H surfaces in the near-edge (fig. 57 a) and the core (fig. 57 b) location.
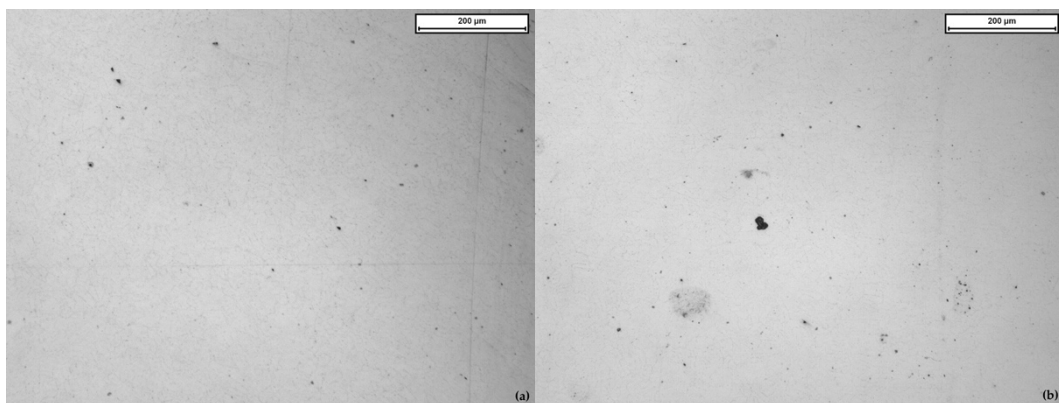
Figure 57: sample H density analysis at edge (a) and core (b) locations.

The summary of flaws analysis of sample H is reported below in Table 18. Compared to sample G, sample H shows a lower average porosity volume fraction. The defect morphology is similar to that observed in previous samples, although, the average aspect ratio has increased both at the core

and the edge of the sample, resulting in defects with a morphology that differs more from the typical gas-related porosity.

| Sample H	Av. aspect ratio	St. dev.	Av. porosity [%]	St. dev.	Av. Feret diameter [μm]	St. dev.
edge	1.675	0.956	0.029	0.018	3.222	2.990
core	1.519	0.601	0.037	0.028	3.050	2.750

Figure 58 shows the grain microstructure of sample H. Qualitatively grains size results fine and evenly distributed. The average grains diameter calculated results to be of 17 μm, likely for the same reasons observed in sample G, which will be discussed in relation to the SEM analysis results of sample H.
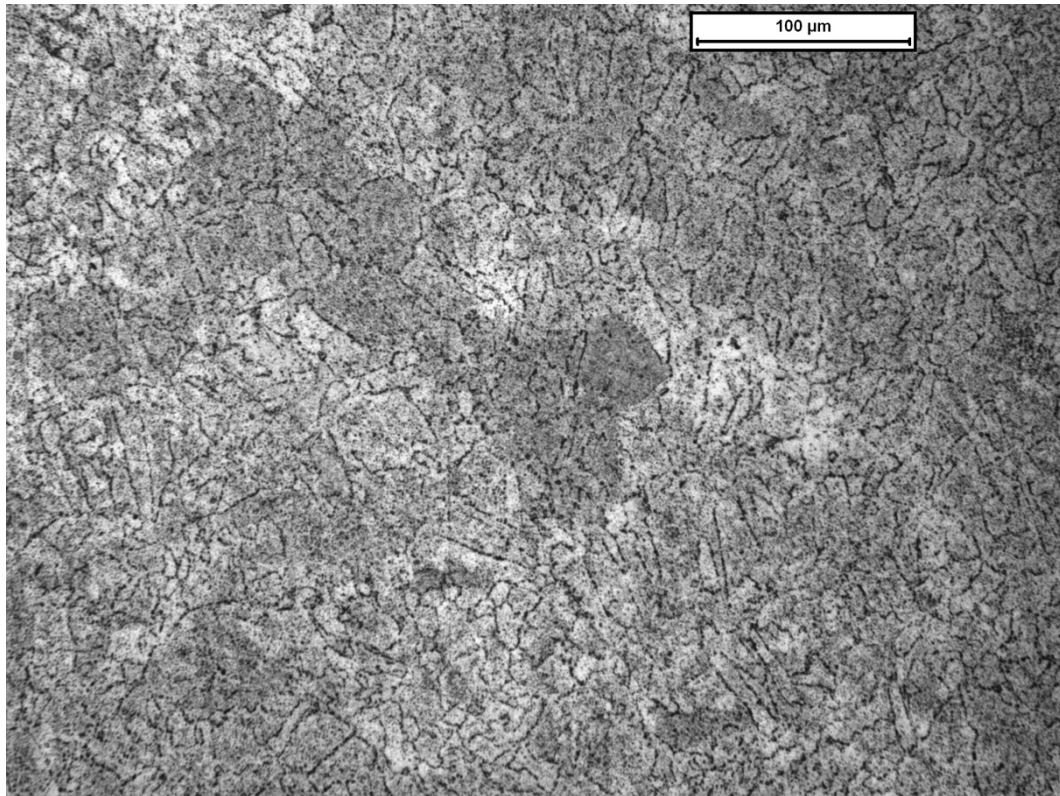
Figure 58: grain microstructure of sample H with LOM at 200x magnification.

Figure 59 shows SEM analyses of images detected with secondary electrons reported can be noticed a large precipitation both in grains and grain boundaries of MC, M_6C and $M_{23}C_6$ type carbides.
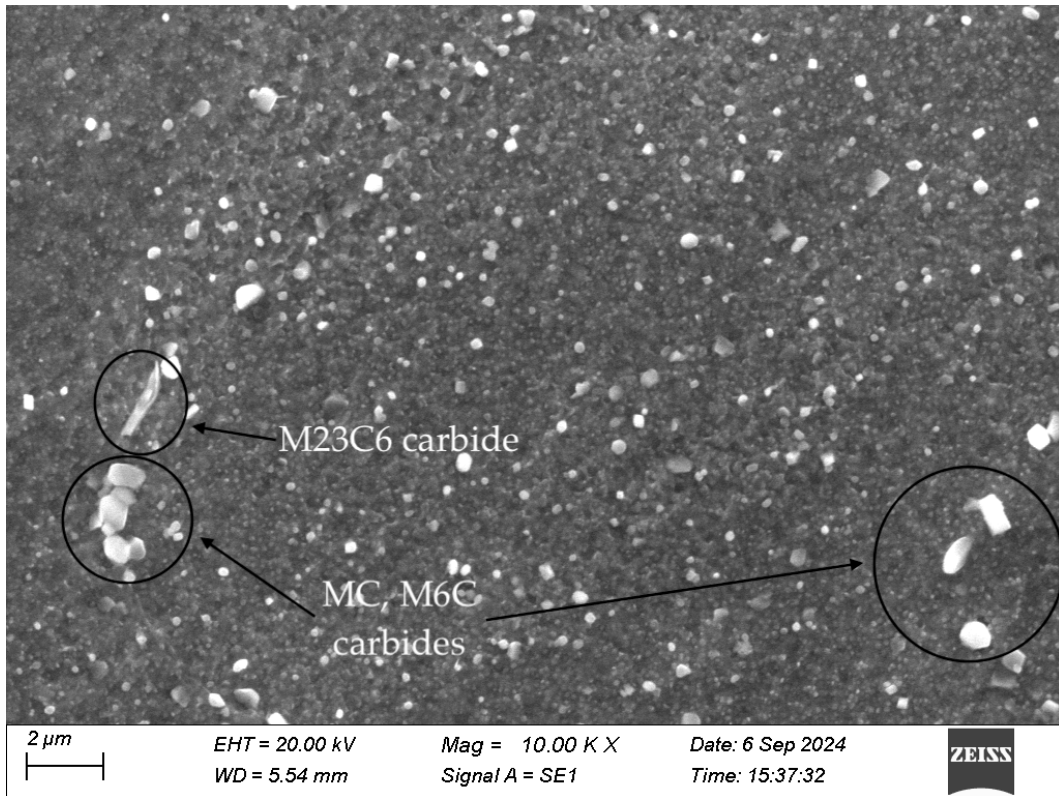
Figure 59: SE1 signal of MC and $M_{23}C_6$ type carbides in sample H.

Figure 60 shows M_6C and $M_{23}C_6$ type carbides decorating the grain boundaries which for an easier view were marked with red dotted lines. Reported precipitated secondary phases in sample H are more abundant and finer than those in samples of the previous set trials at 1280 and 1290 °C. This also justified the grain microstructure.
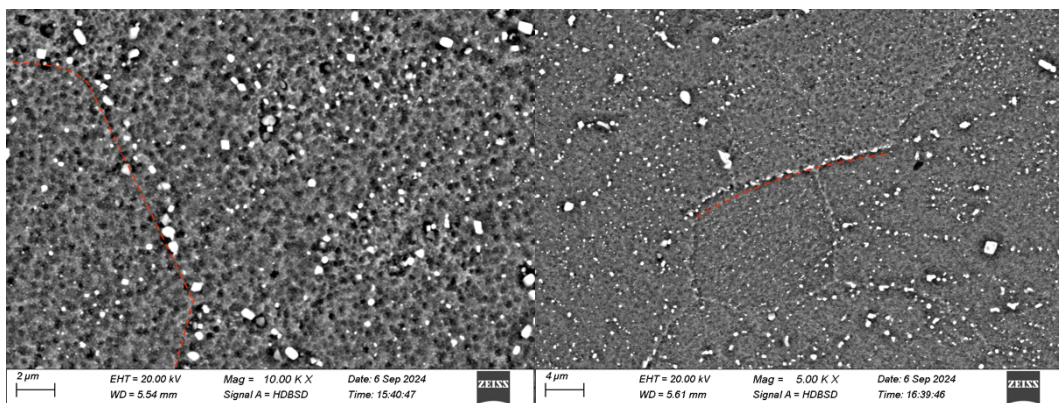
Figure 60: BSD signal of carbides decorating grain boundaries in sample H.

Sample I)

Figure 61 shows defect analysis images from the sample surface both at near-edge (fig. 61 a) and core (fig. 61 b).
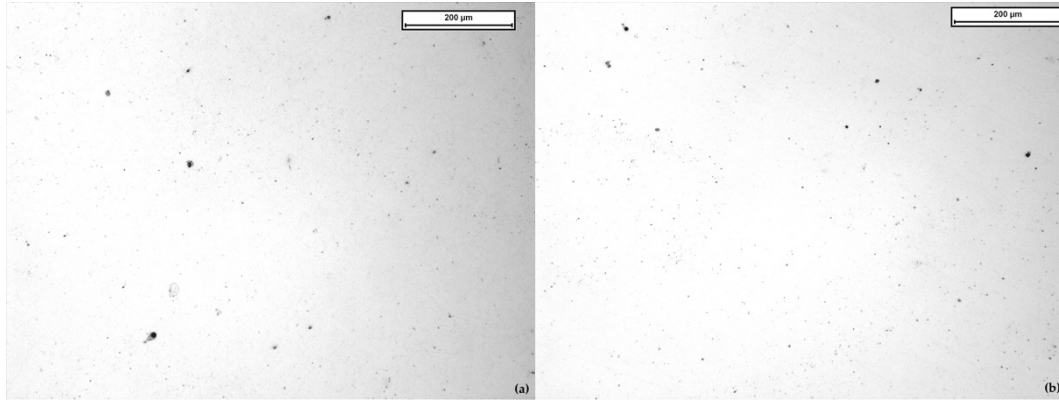
Figure 61: sample I density analysis at near-edge (a) and core (b) locations.

The summary data resulting from the defects analysis is reported in table 18. in this case the average porosity volume fraction results in between the values found for samples G and H, in particular specimen I results more defective if compared to H on the contrary if compared to G.

Table 19: sample I summary of defects analysis.

Sample I	Av. aspect ratio	St. dev.	Av. porosity [%]	St. dev.	Av. Feret diameter [μm]	St. dev.
edge	1.470	0.459	0.077	0.038	2.075	1.679
core	1.495	0.660	0.077	0.053	2.233	2.618

Figure 62 shows the grain microstructure of specimen I. Even in this case, pictures were taken at 200x magnification. As can be seen grains size is fine; qualitatively can be seen grains larger than other resulting in a bimodal grains size distribution. From calculation is obtained an average grains diameter of 16 μm resulting in the finest grains size among all the set trials conducted.
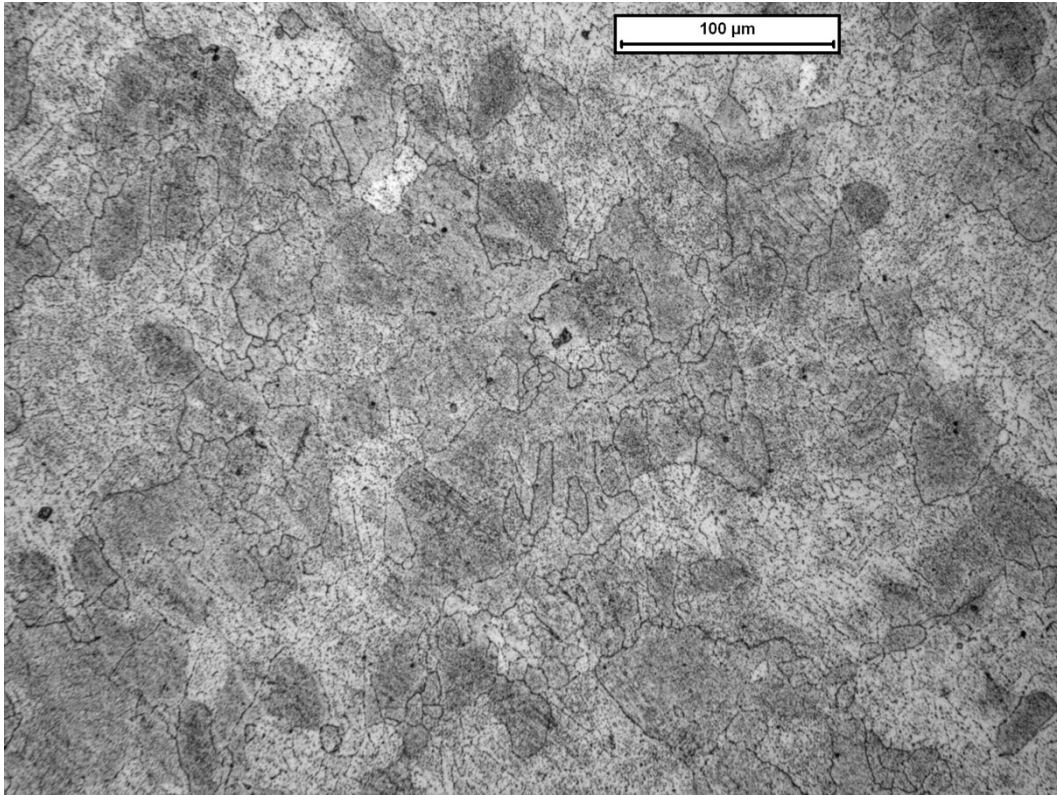
*Figure 62: grain microstructure of sample I with LOM at 200x magnification.*

Figure 63 shows SEM analysis images of sample I. It's displayed fine $M_{23}C_6$ and M_6C type carbides decorating grain boundaries (fig. 63 a). In fig 63 (b) are reported a MC type carbide within the grain and a large $M_{23}C_6$ intergranular carbide. Even in this case the abundant precipitated secondary phases has affected the grain growth process leading to a fine grain microstructure as seen in sample G and H.
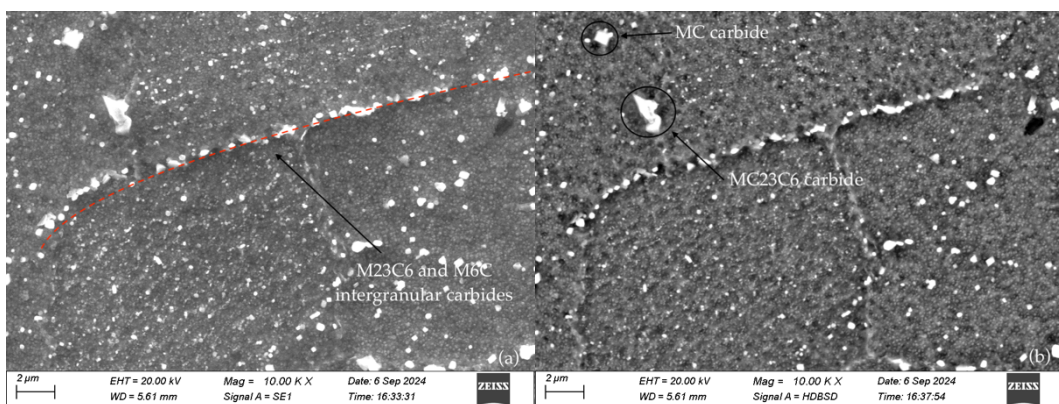
Figure 63: SE1 (a) signal of $M_{23}C_6$ and M_6C type carbides decorating grain boundaries and BSD (b) signal of MC type carbide within grains in sample I.

3.7 Design of experiment analyses

In order to evaluate which of the 3 HIP parameter respectively: temperature, pressure and time, has influenced the most density and grains microstructure of the material data are implemented in 2 steps.

3.7.1 DOE results for material density

Firstly, was investigated the effect of the parameters on the density of the material. As example is reported in Table 20 the calculation of the mean value of the average volume fraction porosity resulting from defect analyses of HIP samples. This mean value was calculated for each of the 9 HIP samples (A-I) to conduct the material density data analysis.

Table 20: mean percentual volume fraction calculation for sample A.

sample A	average porosity [%]
edge	0.063
core	0.065
Mean porosity [%]	*0.064*

Mean values were implemented in Minitab. The software then evaluates which parameter is the most impactful by analyzing the mean values of the signal-to-noise ratios from each of the 9 trials, ranking them from highest to lowest. Since the main objective in this case is to lower the mean percentage porosity, the software analysis was set to the 'smaller is better' option. Results are reported in Figure 64. Delta value corresponds to the difference between the higher and the lower mean values, by doing this calculation for the signal to noise ratios Minitab ranks which parameter was the most impactful among all the trials. Can be noticed that the highest value of delta corresponds to pressure make it the parameter that has the most impact. So, to reduce porosity in the material through super solidus HIP process pressure parameter is fundamental, followed by temperature and time.

Response Table for Signal to Noise Ratios

Smaller is better

Level	temperature	pressure	time
1	23,80	23,25	24,67
2	26,64	27,25	25,83
3	24,86	24,81	24,81
Delta	2,85	4,00	1,16
Rank	2	1	3

Figure 64: results of DOE smaller is better analysis.

In Figure 65 the average percentual porosity for each parameter were reported, the best values correspond to these parameters setting: 1280 °C, 125 MPa and 160 minutes. It is clearly visualized the high impact of pressure on density material control.
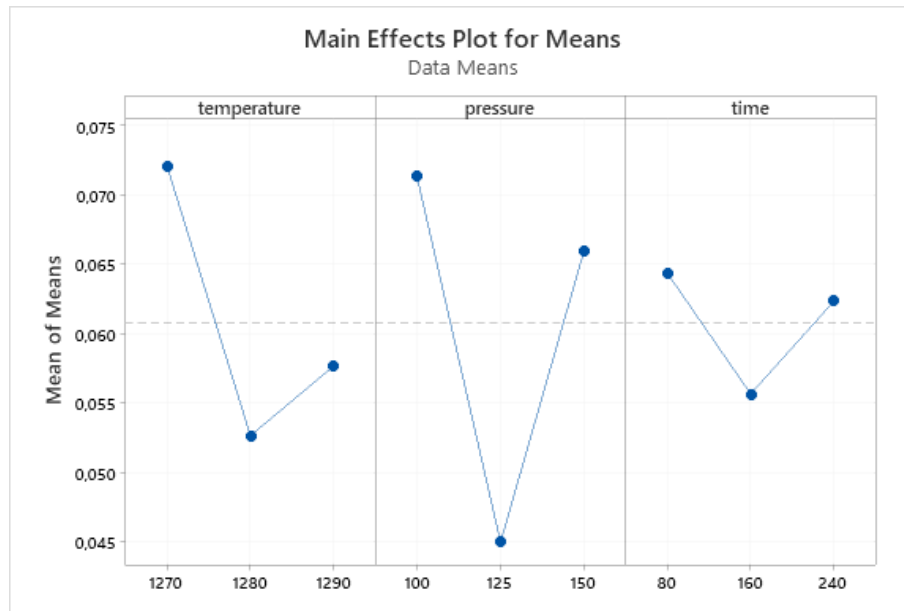

Figure 65: results of DOE smaller is better analysis, best percentual porosity for each parameter.

Figure 66 shows a specular graph compared to that showed before, this result is perfectly in line with what was stated above concerning the delta values.
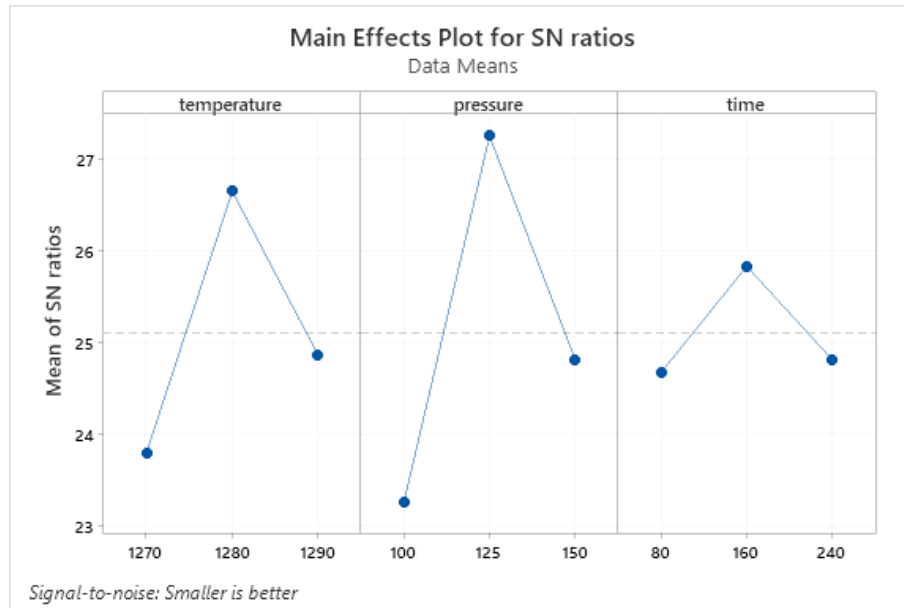
Figure 66: results of DOE smaller is better analysis, maximum values of S/N ratios for each parameter.

This final result could seem counterintuitive based on previously information gathered in chapter 1. For IN738 a possible justification can be that pressure and liquid formation due to incipient melting have acted synergistically on defects closure, enhancing the final material density. Temperatures values of 1270 and 1290 °C do not have a very good effect on the material microstructure. At 1270 °C the amount of liquid is small and the lower temperature reduces the diffusivity of the elements leading to a less effective pore closure. On the other hand, at 1290 °C the amount of liquid is higher and possibly, this temperature could stabilize hard phases (MC carbides or Nitro-Carbides) resulting again in a less effective closure of the pores. According to the above description, time plays a marginal role during this process because it's the least impactful parameter. Probably 160 minutes is the best time value that allows for the best diffusive condition, assisted by the presence of small amount of molten alloy. Too long or short timing will lead to a worsening of the final density.

3.7.2 DOE results for grain size control

The second investigation was conducted to maximize the grains size as a consequence of the HIP treatment conducted in a super-solvus and super-solidus regime. In this case, the average grain diameters resulting from each

of 9 trials was implemented in the Minitab software. Since in this case the main objective is to obtain a coarser grains size in respect to the as built state, the software analysis has been set as "larger is better". Figure 67 shows results from Minitab DOE.

Response Table for Signal to Noise Ratios

Larger is better

Level	temperature	pressure	time
1	24,93	36,35	36,91
2	45,31	36,42	37,32
3	41,21	38,68	37,23
Delta	20,37	2,33	0,41
Rank	1	2	3

Figure 67: results of DOE larger is better analysis.

Based on a comparison of the delta values, it can be stated that temperature is the most influential parameter, surpassing pressure and time, with delta values differing by two orders of magnitude. Figure 68 shows the graph with the higher mean values obtained for each parameter settings. It is clearly visible the predominant impact of temperature on grain growth.
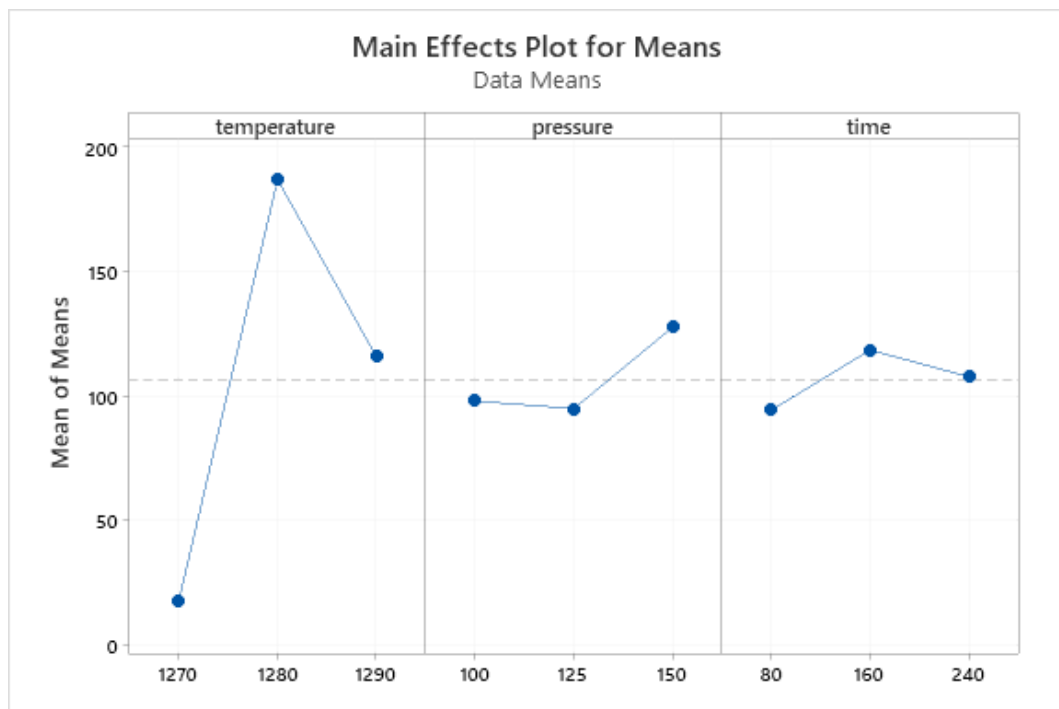

Figure 68: results of DOE larger is better analysis, best average grains diameter for each parameter.

Figure 69 shows the maximum values of signal to noise ratios correspond to 1280 °C, 150 MPa and 160 minutes. This result is in line with what has already been stated previously in Chapter 1.
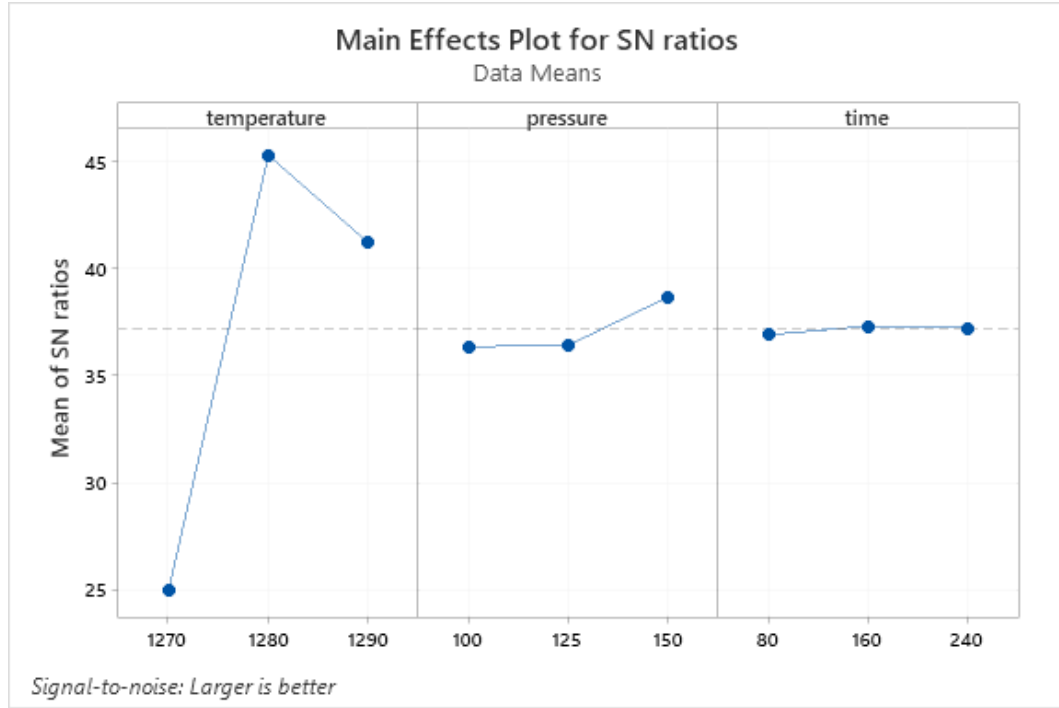
Figure 69: results of DOE larger is better analysis, maximum S/N ratios for each parameter.

Finally, considering the DOE results, it can be stated that temperature has the strongest effect on grain growth control. In particular treating the material at 1280 °C was considered the best option to obtain the highest amount of grain recrystallization. Time seems to play only a limited or null effect to the grain growth process. According to the DOE results, pressure has a smaller effect, and generally speaking higher values seems to bring better results for grain coarsening. This result is counterintuitive, but it can be explained considering that higher pressures could hinder or delay the precipitation of carbides and γ′ particles at the grain boundaries. The grains can grow more freely as the time goes by thanks to a lower pinning effect. This hypothesis, though, requires more experimental work for its validation. Final synoptic table is reported in Figure 70 and to provide an overall view of the microstructure evolution, particularly the grain microstructure after the HIP treatment performed in the super-solidus temperature range of the material.

Figure 70: HIP samples grain microstructure synoptic table.

Chapter 4

Conclusions

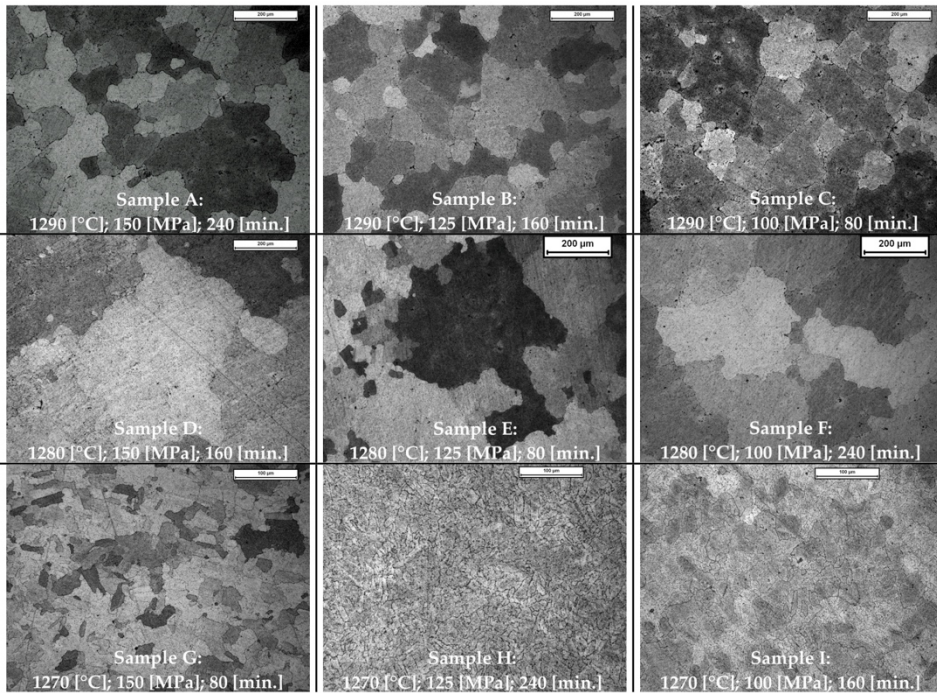The final scope of this thesis was to develop an alternative heat treatment within a hot isostatic pressing furnace for an LPBF IN738. Due to the nature of the additive manufacturing process, which relies on the selective melting of very thin layer of powders, the resulting microstructure of the material is considerably different to that of a cast material. Several defects and a much finer grain structure are common features in these materials. The use of such structures in components designed to resist creep should be discouraged, unless a dedicated heat treatment modifies this starting microstructure with a more proper one, consisting of a fully dense and coarse-grained material. IN738 is known for its microstructural stability and recrystallization is notoriously close to zero when treated at 1120 °C, i.e. its standard solutioning temperature. Thus, an obvious workaround for grain coarsening could be adopting very high temperatures during the solutioning heat treatment. By the way, it was noticed that significative grain coarsening was achievable only at temperatures at which the material started to form traces of liquid. Normally, this condition would be unacceptable because it would lead to the formation of detrimental defects, brought by liquid expansion. This scenario can be avoided if during the heating a strong pressure is applied from outside as normally happens during HIP process. This thesis explains how the use of high pressures and temperatures (above the solidus point) could be used to satisfy the microstructural requirements previously mentioned.

The experimental work began with the evaluation of the as built state. Defect volume fraction was calculated with standard metallographic procedures. Several heat treatments were employed to assess how temperature would affect the material microstructure, with special concern to the final grain size. LPBF IN738 has shown higher γ′ solvus temperature (> 1180 °C) than cast IN738 and incipient melting occurs at temperature of

1260 °C. The results of this thesis proved that. After this initial set-up procedure, which was performed in a traditional furnace, the experimental work was moved to the HIP. In order to explore the optimal range of time, pressure and temperature for the HIP treatment for achieving the above-mentioned targets, a 3X3 design of experiment (DOE) was arranged, aiming at minimizing the residual porosity and maximizing the grain size of the material.

The main results obtained are summarized as follows:

- **HIP treatment at 1290 °C (samples A, B, C)**: samples show an overall 21% reduction of the defect volume fraction as compared to the as built state. Grains present a sort of bimodal distribution, with an average size of 116 ± 14.79 μm. The typical elongated texture of the grains parallel to the building direction is no longer evident.

- **HIP treatment at 1280 °C (samples D, E, F):** samples show an overall 28% reduction of the defects volume fraction if compared to the as built state. The grains are more uniform compared to the previous condition, showing grains with an average size of 187 ± 37.54 μm. Similarly to the previous case, texture along the building direction is no longer visible.

- **HIP treatment at 1270 °C (G, H, I):** samples show an overall 1% reduction of the defects volume fraction if compared to the as built state. Grains structure is finer with an average size of 18 ± 2.78 μm. Moreover, grains have a bimodal distribution. Nevertheless, the texture along the building direction is no longer visible.

Considering the results obtained with the DOE using the Taguchi method the optimal parameter set for super solidus HIP treatment should be 1280 °C, 125 MPa at 160 minutes to achieve the best material density value and 1280 °C, 150 MPa at 160 minutes to obtain the coarser grain microstructure. Indeed, sample D treated at 1280 °C, 150 MPa and 160 minutes display both

the least defects volume fraction (2.8 %) and the largest average grains diameter (229 μm). Based on these final results, it can be said that super solidus hot isostatic pressing is a feasible tool for reducing the amount of defects and obtaining a larger grain size in LPBF materials. Obviously, other heat treatments, such as first and second aging are still required to achieve the best mix of reinforcing phases such as γ′ and carbides. Future works may focus on the optimization of the latter stages of the heat treatment and set the bases for a validation study involving mechanical test such as creep, stress rupture and fatigue tests.

Acknowledgements

At the end of this intense journey, I feel a deep sense of gratitude toward all the people who have stood by my side. First and foremost, my family, who never made me feel like I lacked anything. They have always supported me in every way over these years, and I hope that today, in some way, I have repaid them. I love you all.

To Ross, to you who support me and put up with me, thank you so much for all the time we've spent together. Thank you for always helping me with love and kindness because, in the end, you too are a little engineer! Every day, I am more and more grateful to have you by my side. I love you.

To my dear friends, I dedicate a huge thank you, especially to you, for everything we have been through together, for the beautiful and sometimes tough moments, for all the adventures, laughter, advice, trips, vacations, goodbyes, and meals. Thank you for always helping and supporting me (especially during the less clear-headed moments...) and, of course, for putting up with me. To all of you, thank you for always being honest with me and for being my second family. I know I am very lucky to have you all by my side.

A special mention goes to Jacopo and Gabriele, because they have been putting up with me for far too long; I love you like brothers. To Paolo, who has been with me since the early days in Turin, and whom I grew fond of right away. To Carla and Asja, who have always made me feel carefree, even in difficult moments; I love you dearly. To Gaetano and Abel, who were fantastic roommates as well as friends, thank you so much, really.

I thank my teachers, my professors, and this institution for providing me with the knowledge and resilience to face whatever comes in the future. I would like to express a special thanks to Professors Emilio and Daniele for standing by my side during these months, for being available, and for sparking my passion for studying.

Finally, I would like to thank everyone once again. Because I know that without you, I probably wouldn't be here, and I wouldn't be who I am today. I care about you all very much.

Bibliography

[1] J. R. Davis Davis & Associates, Nickel, Cobalt, and Their Alloys, first, 2000.

[2] Nasa, Casi, General Disclaimer, n.d.

[3] C. Ma, S.N. Parbat, M.L. Redigolo, M.K. Chyu, B. Kang, Ni-based ODS alloy prepared by direct energy deposition process: powder fabrication, microstructure, mechanical property, and oxidation resistance, Progress in Additive Manufacturing (2024). https://doi.org/10.1007/s40964-024-00710-0.

[4] C. Varvenne, G.P.M. Leyson, M. Ghazisaeidi, W.A. Curtin, Solute strengthening in random alloys, Acta Mater 124 (2017) 660–683. https://doi.org/10.1016/j.actamat.2016.09.046.

[5] M.X. Wang, H. Zhu, G.J. Yang, K. Liu, J.F. Li, L.T. Kong, Solid-solution strengthening effects in binary Ni-based alloys evaluated by high-throughput calculations, Mater Des 198 (2021). https://doi.org/10.1016/j.matdes.2020.109359.

[6] W. Zhang, Y. Zheng, F. Liu, D. Wang, F. Liu, C. Huang, Q. Li, X. Lin, W. Huang, Effect of solution temperature on the microstructure and mechanical properties of Hastelloy X superalloy fabricated by laser directed energy deposition, Materials Science and Engineering: A 820 (2021). https://doi.org/10.1016/j.msea.2021.141537.

[7] R. Ghiaasiaan, A. Poudel, N. Ahmad, P.R. Gradl, S. Shao, N. Shamsaei, High Temperature Tensile and Fatigue Behaviors of Additively Manufactured IN625 and IN718, in: Procedia Structural Integrity, Elsevier B.V., 2021: pp. 581–587. https://doi.org/10.1016/j.prostr.2022.03.059.

[8] X.X. Wu, C.Y. Wang, Influence of alloying elements upon the theoretical tensile strength of Ni-based model superalloy: γ-Ni/γ'-Ni3Al multilayer, Comput Mater Sci 119 (2016) 120–129. https://doi.org/10.1016/j.commatsci.2016.04.001.

[9] A. Jena, S.E. Atabay, A. Gontcharov, P. Lowden, M. Brochu, Laser powder bed fusion of a new high gamma prime Ni-based superalloy

with improved weldability, Mater Des 208 (2021). https://doi.org/10.1016/j.matdes.2021.109895.

[10] F.C. Campbell, Superalloys, in: Manufacturing Technology for Aerospace Structural Materials, Elsevier, 2006: pp. 211–272. https://doi.org/10.1016/B978-185617495-4/50006-8.

[11] Y.C. Lin, M. He, M.S. Chen, D.X. Wen, J. Chen, Effects of initial δ phase (Ni3Nb) on hot tensile deformation behaviors and material constants of Ni-based superalloy, Transactions of Nonferrous Metals Society of China (English Edition) 26 (2016) 107–117. https://doi.org/10.1016/S1003-6326(15)64043-2.

[12] L.S.B. Ling, Z. Yin, Z. Hu, J. Wang, B. De Sun, Effects of the γ-Ni3Nb phase on fatigue behavior of nickel-based 718 superalloys with different heat treatments, Materials 12 (2019). https://doi.org/10.3390/ma12233979.

[13] I. Lopez-Galilea, J. Koßmann, A. Kostka, R. Drautz, L. Mujica Roncery, T. Hammerschmidt, S. Huth, W. Theisen, The thermal stability of topologically close-packed phases in the single-crystal Ni-base superalloy ERBO/1, J Mater Sci 51 (2016) 2653–2664. https://doi.org/10.1007/s10853-015-9579-7.

[14] X. Song, Y. Wang, X. Zhao, J. Zhang, Y. Li, Y. Wang, Z. Chen, Analysis of carbide transformation in MC-M23C6 and its effect on mechanical properties of Ni-based superalloy, J Alloys Compd 911 (2022). https://doi.org/10.1016/j.jallcom.2022.164959.

[15] O.M.D.M. Messé, R. Muñoz-Moreno, T. Illston, S. Baker, H.J. Stone, Metastable carbides and their impact on recrystallisation in IN738LC processed by selective laser melting, Addit Manuf 22 (2018) 394–404. https://doi.org/10.1016/j.addma.2018.05.030.

[16] F. Theska, W.F. Tse, B. Schulz, R. Buerstmayr, S.R. Street, M. Lison-Pick, S. Primig, Review of Microstructure–Mechanical Property Relationships in Cast and Wrought Ni-Based Superalloys with Boron, Carbon, and Zirconium Microalloying Additions, Adv Eng Mater 25 (2023). https://doi.org/10.1002/adem.202201514.

[17] X. Dong, X. Zhang, K. Du, Y. Zhou, T. Jin, H. Ye, Microstructure of Carbides at Grain Boundaries in Nickel Based Superalloys, 2012.

[18] SUPERALLOYS, SUPERCOMPOSITES AND SUPERCERAMICS, n.d.

[19] S. Sravan Sashank, S. Rajakumar, R. Karthikeyan, D.S. Nagaraju, Weldability, Mechanical Properties and Microstructure of Nickel Based Super Alloys: A review, in: E3S Web of Conferences, EDP Sciences, 2020. https://doi.org/10.1051/e3sconf/202018401040.

[20] T. Altan F. W. Boulger J. R. Becker N. Akgerman H. J. Henning, Forging Equipment, Materials, and Practices, 1973.

[21] M.J. Donachie, S.J. Donachie, SELECTION OF SUPERALLOYS FOR DESIGN, n.d.

[22] N. Perevoshchikova, J. Rigaud, Y. Sha, M. Heilmaier, B. Finnin, E. Labelle, X. Wu, al Optimi, Optimisation of selective laser melting parameters for the Ni-based superalloy IN-738 LC using Doehlert's design, Rapid Prototyp J 23 (2017). https://doi.org/10.1108/RPJ-04-2016-0063ï.

[23] W.J. Sames, F.A. List, S. Pannala, R.R. Dehoff, S.S. Babu, The metallurgy and processing science of metal additive manufacturing, International Materials Reviews 61 (2016) 315–360. https://doi.org/10.1080/09506608.2015.1116649.

[24] Additive manufacturing-General principles-Terminology COPYRIGHT PROTECTED DOCUMENT, n.d. www.iso.orgwww.astm.orgiTehSTANDARDPREVIEWISO/ASTM52900:2015https://standards.iteh.ai/catalog/standards/sist/d9adc3ce-ca51-4c21-b508-00fbbe01687d/iso-astm-52900-2015.

[25] A. Mostafaei, C. Zhao, Y. He, S. Reza Ghiaasiaan, B. Shi, S. Shao, N. Shamsaei, Z. Wu, N. Kouraytem, T. Sun, J. Pauza, J. V. Gordon, B. Webler, N.D. Parab, M. Asherloo, Q. Guo, L. Chen, A.D. Rollett, Defects and anomalies in powder bed fusion metal additive manufacturing, Curr Opin Solid State Mater Sci 26 (2022). https://doi.org/10.1016/j.cossms.2021.100974.

[26] C. Yan, L. Hao, A. Hussein, D. Raymont, Evaluations of cellular lattice structures manufactured using selective laser melting, Int J Mach Tools Manuf 62 (2012) 32–38. https://doi.org/10.1016/J.IJMACHTOOLS.2012.06.002.

[27] Manufacturing Milestone: 30,000 Additive Fuel Nozzles | GE Aerospace News, (n.d.). https://www.geaerospace.com/news/articles/manufacturing/manufacturing-milestone-30000-additive-fuel-nozzles (accessed August 30, 2024).

[28] GM Uses Advanced Software, 3D Printing to Make Kinda Creepy-Looking Lightweight Parts - The News Wheel, (n.d.). https://thenewswheel.com/gm-uses-advanced-software-3d-printing-to-make-kinda-creepy-looking-lightweight-parts/ (accessed August 30, 2024).

[29] H.L. Wei, T. Mukherjee, W. Zhang, J.S. Zuback, G.L. Knapp, A. De, T. DebRoy, Mechanistic models for additive manufacturing of metallic components, Prog Mater Sci 116 (2021). https://doi.org/10.1016/j.pmatsci.2020.100703.

[30] C. Zhao, N.D. Parab, X. Li, K. Fezzaa, W. Tan, A.D. Rollett, T. Sun, Critical instability at moving keyhole tip generates porosity in laser melting, n.d. https://www.science.org.

[31] Z.A. Young, Q. Guo, N.D. Parab, C. Zhao, M. Qu, L.I. Escano, K. Fezzaa, W. Everhart, T. Sun, L. Chen, Types of spatter and their features and formation mechanisms in laser powder bed fusion additive manufacturing process, Addit Manuf 36 (2020). https://doi.org/10.1016/j.addma.2020.101438.

[32] C. Zhao, K. Fezzaa, R.W. Cunningham, H. Wen, F. De Carlo, L. Chen, A.D. Rollett, T. Sun, Real-time monitoring of laser powder bed fusion process using high-speed X-ray imaging and diffraction, Sci Rep 7 (2017). https://doi.org/10.1038/s41598-017-03761-2.

[33] R. Cunningham, C. Zhao, N. Parab, C. Kantzos, J. Pauza, K. Fezzaa, T. Sun, A.D. Rollett, Keyhole threshold and morphology in laser melting revealed by ultrahigh-speed x-ray imaging, Science 363 (2019) 849–852. https://doi.org/10.1126/SCIENCE.AAV4687.

[34] U. Gratzke, P.D. Kapadia, J. Dowden, J. Kroos, G. Simon, Theoretical Approach to The Humping Phenomenon in Welding Processes, J Phys D Appl Phys 25 (1992) 1640–1647. https://doi.org/10.1088/0022-3727/25/11/012.

[35]   X. Meng, G. Qin, A theoretical study of molten pool behavior and humping formation in full penetration high-speed gas tungsten arc welding, Int J Heat Mass Transf 132 (2019) 143–153. https://doi.org/10.1016/J.IJHEATMASSTRANSFER.2018.12.004.

[36]   H. Ali, H. Ghadbeigi, K. Mumtaz, Effect of scanning strategies on residual stress and mechanical properties of Selective Laser Melted Ti6Al4V, Materials Science and Engineering: A 712 (2018) 175–187. https://doi.org/10.1016/j.msea.2017.11.103.

[37]   S. Catchpole-Smith, N. Aboulkhair, L. Parry, C. Tuck, I.A. Ashcroft, A. Clare, Fractal scan strategies for selective laser melting of 'unweldable' nickel superalloys, Addit Manuf 15 (2017) 113–122. https://doi.org/10.1016/j.addma.2017.02.002.

[38]   M.S. Chen, Z.H. Zou, Y.C. Lin, H. Bin Li, W.Q. Yuan, Effects of annealing parameters on microstructural evolution of a typical nickel-based superalloy during annealing treatment, Mater Charact 141 (2018) 212–222. https://doi.org/10.1016/j.matchar.2018.04.056.

[39]   Y. Zhang, J. Li, Y. Wu, Q. Feng, J. Liu, T. Liu, Microstructure Evolution of a Nickel-Based Powder Metallurgy Superalloy Under Different Solution Treatment Temperatures, Adv Eng Mater 24 (2022). https://doi.org/10.1002/adem.202200004.

[40]   I. Guzman, A. Garza, F. Garcia, J. Acevedo, R. Méndez, Effect of heat treatment solution on the size and distribution of gamma prime (γ′) of super-alloy INCONEL 738, in: Materials Research Society Symposium Proceedings, 2012: pp. 81–88. https://doi.org/10.1557/opl.2012.110.

[41]   A. Martucci, G. Marchese, E. Bassini, M. Lombardi, Effects of Stress-Relieving Temperature on Residual Stresses, Microstructure and Mechanical Behaviour of Inconel 625 Processed by PBF-LB/M, Metals (Basel) 13 (2023). https://doi.org/10.3390/met13040796.

[42]   INTERNATIONAL ® The Materials Information Company, n.d.

[43]   J.L. Dossett, Practical Heat Treating, ASM International, 2020. https://doi.org/10.31399/asm.tb.phtbp.9781627083263.

[44]   S. Linn, A. Scholz, M. Oechsner, C. Berger, O. Luesebrink, Evaluation of property scatter of Ni-base alloy in 738 LC, Materials Science and

Engineering: A 528 (2011) 4676–4682. https://doi.org/10.1016/j.msea.2011.02.052.

[45] M.-A. Charpagne, J.-M. Franchet, N. Bozzolo, Overgrown grains appearing during sub-solvus heat treatment in a polycrystalline γ-γ′ Nickel-based superalloy, Mater Des 144 (2018) 353–360. https://doi.org/10.1016/j.matdes.2018.02.048ï.

[46] O.A. Ojo, N.L. Richards, M.C. Chaturvedi, On incipient melting during high temperature heat treatment of cast Inconel 738 superalloy, n.d.

[47] Y.X. Liu, Z.J. Ke, R.H. Li, J.Q. Song, J.J. Ruan, Study of grain growth in a Ni-based super alloy by experiments and cellular automaton model, Materials 14 (2021). https://doi.org/10.3390/ma14226922.

[48] Y. Li, X. Liang, G. Peng, F. Lin, Effect of heat treatments on the microstructure and mechanical properties of IN738LC prepared by electron beam powder bed fusion, J Alloys Compd 918 (2022). https://doi.org/10.1016/j.jallcom.2022.165807.

[49] E.C. Caldwell, F.J. Fela, G.E. Fuchs, SEGREGATION OF ELEMENTS IN HIGH REFRACTORY CONTENT SINGLE CRYSTAL NICKEL BASED SUPERALLOYS, 2004.

[50] B. Schulz, T. Leitner, S. Primig, In-situ observation of the incipient melting of borides and its effect on the hot-workability of Ni-based superalloys, J Alloys Compd 956 (2023). https://doi.org/10.1016/j.jallcom.2023.170324.

[51] J.Q. Peng, H.T. Zhang, Y.F. Li, Review of Blade Materials for IGT, in: Procedia Eng, Elsevier Ltd, 2015: pp. 668–675. https://doi.org/10.1016/j.proeng.2015.12.295.

[52] ALLOY IN-738 TECHNICAL DATA A PRACTICAL GUIDE TO THE USE OF NICKEL-CONTAINING ALLOYS N O 497, n.d. www.nickelinstitute.org.

[53] W. Zhou, Y. Tian, D. Wei, Q. Tan, D. Kong, H. Luo, W. Huang, G. Zhu, D. Shu, J. Mi, B. Sun, Effects of heat treatments on the microstructure and tensile properties of IN738 superalloy with high carbon content fabricated via laser powder bed fusion, J Alloys Compd 953 (2023). https://doi.org/10.1016/j.jallcom.2023.170110.

[54] Y. Hu, H. Jia, X. Zhang, X. Yang, D. Zhang, Delayed recrystallization behavior and deformation mechanism of IN738LC alloy prepared by laser powder bed fusion, Materials Science and Engineering: A 903 (2024). https://doi.org/10.1016/j.msea.2024.146697.

[55] O.M.D.M. Messé, R. Muñoz-Moreno, T. Illston, S. Baker, H.J. Stone, Metastable carbides and their impact on recrystallisation in IN738LC processed by selective laser melting, Addit Manuf 22 (2018) 394–404. https://doi.org/10.1016/j.addma.2018.05.030.

[56] J. Risse, Jeroen Risse Additive Manufacturing of Nickel-Base Superalloy IN738LC by Laser Powder Bed Fusion, n.d.

[57] Z. Sun, Y. Ma, D. Ponge, S. Zaefferer, E.A. Jägle, B. Gault, A.D. Rollett, D. Raabe, Thermodynamics-guided alloy and process design for additive manufacturing, Nat Commun 13 (2022). https://doi.org/10.1038/s41467-022-31969-y.

[58] L. Zhang, Y. Li, Q. Zhang, S. Zhang, Microstructure evolution, phase transformation and mechanical properties of IN738 superalloy fabricated by selective laser melting under different heat treatments, Materials Science and Engineering: A 844 (2022). https://doi.org/10.1016/j.msea.2022.142947.

[59] I. Lopez-Galilea, L. Hecker, A. Epishin, D. Bürger, B. Ruttert, P. Thome, S. Weber, W. Theisen, Super-Solidus Hot Isostatic Pressing Heat Treatments for Advanced Single Crystal Ni-Base Superalloys, Metall Mater Trans A Phys Metall Mater Sci 54 (2023) 1509–1525. https://doi.org/10.1007/s11661-022-06884-y.

[60] Material Datasheet, 2020. www.siemens-energy.com/am.

[61] G.F. Vander Voort, E.P. Manilova, Metallographic techniques for superalloys, in: Microscopy and Microanalysis, 2004: pp. 690–691. https://doi.org/10.1017/S1431927604883442.

[62] Designation: E112 – 13 Standard Test Methods for Determining Average Grain Size 1, (n.d.). https://doi.org/10.1520/E0112-13R21.

[63] S. Ghalme, A. Mankar, Y.J. Bhalerao, Optimization of wear loss in silicon nitride (Si3N4)–hexagonal boron nitride (hBN) composite using DoE–Taguchi method, Springerplus 5 (2016). https://doi.org/10.1186/s40064-016-3379-7.

[64] N. Li, C. Shi, Z. Zhang, H. Wang, Y. Liu, A review on mixture design methods for geopolymer concrete, Compos B Eng 178 (2019). https://doi.org/10.1016/j.compositesb.2019.107490.

[65] What is MiniTab? Data Analysis Tool | Simplilearn, (n.d.). https://www.simplilearn.com/what-is-minitab-data-analysis-tool-article (accessed September 29, 2024).

[66] K. Song, M. Aindow, Grain growth and particle pinning in a model Ni-based superalloy, Materials Science and Engineering: A 479 (2008) 365–372. https://doi.org/10.1016/j.msea.2007.09.055.